unesp ❖ UNIVERSIDADE ESTADUAL PAULISTA
"JÚLIO DE MESQUITA FILHO"
CAMPUS DE GUARATINGUETÁ

SAMIR BOSET ROJAS CHAVEZ

Schlieren and PLIF imaging for hydrogen-air detonations

Guaratinguetá - SP
2019

Samir Boset Rojas Chávez

Schlieren and PLIF imaging for hydrogen-air detonations

Dissertação apresentada à Faculdade de Engenharia do Campus de Guaratinguetá, Universidade Estadual Paulista, para obtenção do título de Mestre em Engenharia Mecânica na área de transmissão e conversão de energia.

Orientador: Prof. Dr. João Andrade de Carvalho Jr
Coorientador:Prof. Dr. Andrés Mendiburu Zevallos

Guaratinguetá - SP
2019

unesp ❖

UNIVERSIDADE ESTADUAL PAULISTA
CAMPUS DE GUARATINGUETÁ

SAMIR BOSET ROJAS CHÁVEZ

ESTA DISSERTAÇÃO FOI JULGADA ADEQUADA PARA A OBTENÇÃO DO TÍTULO DE
"MESTRE EM ENGENHARIA MECÂNICA"

PROGRAMA: ENGENHARIA MECÂNICA
ÁREA: ENERGIA

APROVADA EM SUA FORMA FINAL PELO PROGRAMA DE PÓS-GRADUAÇÃO

Profª. Drª. Ivonete Ávila
Coordenadora

BANCA   EXAMINADORA:

Prof. Dr. JOÃO ANDRADE DE CARVALHO JUNIOR
Orientador / UNESP/FEG

Prof. Dr. JOSÉ ANTONIO PERRELLA BALESTIERI
UNESP/FEG

Prof. Dr. CHRISTIAN JEREMI CORONADO
UNIFEI

dezembro de 2019

DADOS CURRICULARES

SAMIR BOSET ROJAS CHAVEZ

NASCIMENTO   24.02.1994 – Chimbote / Perú

FILIAÇÃO   Hernan Octavio Rojas Garcia
                    Yolanda Chávez Ortega

2012/2017   Curso de graduação –Engenharia em Energia
                    Universidad Nacional del Santa

2018/2019   Curso de Pós-graduação em Engenharia Mecânica, nível de mestrado
                    na Faculdade de Engenharia do Campus de Guaratinguetá da Universidade
                    Estadual Paulista.

To my mother, father, and sister who always support me in my academic life.

ACKNOWLEDGEMENTS

"My help cometh from the LORD, which made heaven and earth."

Psalm 121:2

ABSTRACT

Application technologies based on the detonation cycle has proven a significant impact on the overall efficiency. However, detonation engines are not currently available on the markets due to the lack of physical and chemical knowledge of the detonation phenomenon. The present study aims to provide new insights by studying the pressure and velocity, the density gradient of the detonation wave, and the OH distribution on the reaction zone of hydrogen-air detonation. Three strategies were proposed to obtain repeatable detonation events. The strategies vary on the geometry of the obstacle and the amount of spark plug to ignite the mixture. Pressure and velocity were recorded to determine if the transition from deflagration to detonation is successful. To image the density gradient of the shock wave, the optical technique called Schlieren was adapted to the detonation test bench. The OH radical distribution was studied by the optical diagnostic technique called planar laser-induced fluorescence. The pressure trace results showed high peaks in the regimen of Chapman-Jouguet state for detonation, unlike fast flames. The velocity results showed a considerable influence of the obstacle geometry to enhance the velocity of the wave, although the repeatable detonation events and the steadiness of the velocity were not boosted. The third strategy proved that adding more energy to a transient detonation wave, enhanced the stability and the consistent production of detonation events. The Schlieren images revealed the coupling between the reaction and shock wave for detonation, unlike fast flames. Fast flames close to 83% of the Chapman-Jouguet velocity underwent weak decoupling compared to the fast flame with velocities in the range of 40% of the Chapman-Jouguet velocity. The detonation density gradient images, obtained by using a bandpass filter, revealed an irregular cellular structure for different conditions when detonation occurs. The single image obtained by the technique planar laser-induced fluorescence at 0.5 bar, 293 K, and stoichiometric mixture showed the influence of the cellular structure of the shock wave into the reaction zone since an irregular cellular structure was captured at the beginning of the reaction zone. The fluorescence intensity profile registered the maximum values at the beginning of the reaction zone, followed by a fast decrease of the intensity.

KEYWORDS: Detonation. Hydrogen-air. PLIF. Schlieren. Fast flames.

RESUMO

Aplicações tecnológicas baseadas no ciclo de detonação provou um enorme impacto na eficiência geral. No entanto, atualmente, os motores de detonação não estão disponíveis nos mercados devido à falta de conhecimento físico e químico do fenômeno de detonação. O presente estudo tem como objetivo fornecer novas idéias, estudando a pressão e a velocidade, o gradiente de densidade da onda de detonação e a distribuição do radical OH na zona de reação das detonações de hidrogênio e ar. Três estratégias foram propostas para obter eventos de detonação repetíveis. As estratégias variam na geometria do obstáculo e a quantidade de vela de ignição para inflamar a mistura. Pressão e velocidade foram registradas para determinar se a transição da deflagração para a detonação é bem-sucedida. Para visualizar o gradiente de densidade da onda de choque, a técnica óptica chamada Schlieren foi adaptada ao banco de testes de detonação. A distribuição do radical OH foi estudada pela técnica de diagnóstico óptico chamada fluorescência induzida por laser planar. Os resultados do traço de pressão revelaram altos picos no regime do estado de Chapman-Jouguet para detonação, diferentemente das chamas rápidas. Os resultados da velocidade permitiram revelar uma influência considerável da geometria do obstáculo para aumentar a velocidade da onda, embora os eventos repetitivos de detonação e a firmeza da velocidade não tenham sido aumentados. A terceira estratégia provou que adicionar mais energia a uma onda de detonação transitória melhorava a estabilidade e a produção consistente de eventos de detonação. As imagens da Schlieren revelaram o acoplamento entre a reação e a onda de choque para detonação, ao contrário das chamas velozes. As chamas rápidas perto de 83% da velocidade de Chapman-Jouguet sofreram desacoplamento fraco em comparação com a chama rápida com velocidades na faixa de 40% da velocidade de Chapman-Jouguet. As imagens de gradiente de densidade de detonação, obtidas com o uso de filtro passa-banda, revelaram uma estrutura celular irregular para diferentes condições quando ocorre a detonação. A única imagem obtida pela técnica fluorescência induzida por laser planar em condições 0,5 bar, 293 K e mistura estequiométrica mostrou a influência da estrutura celular da onda de choque na zona de reação, uma vez que uma estrutura celular irregular foi capturada no início da zona de reação. O perfil de intensidade de fluorescência registrou os valores máximos no início da zona de reação, seguidos por uma rápida diminuição da intensidade.

PALAVRAS-CHAVE: Detonação. Hidrogênio-ar. PLIF. Schlieren. Chamas rápidas.

LIST OF FIGURES

LIST OF ABBREVIATIONS AND ACRONYMS

PDC	Pulse detonation combustion
DCC	Detonation combustion cycles
DDT	Deflagration to detonation transition
PDE	Pulse detonation engine
RDE	Rotating detonation engine
PLIF	Planar laser-induced fluorescence
CARS	Coherent anti-Stokes Raman spectroscopy
CJ	Chapman Jouguet
ER	Equivalence ratio
ZND	Zeldovich-Von Neumann-Doering
VN	Von Neumann
BR	Blockage ratio
CCD	Charge-Coupled Device
ICCD	Intensified Charged Coupled Device
MFC	Mass flow controller
TTL	Transistor-Transistor Logic
ICP	Injection control pressure
BNC	Bayonet Neill–Concelman connector
FS	Full scale
SP	Spark plug
LED	Light-emitting diode
CMOS	Complementary metal-oxide–semiconductor
UV	Ultraviolet
FA	Flame acceleration

LIST OF SYMBOLS

P	Pressure, Pressure sensor
T	Temperature
ρ	Density
V,v	Velocity
h	Enthalpy
υ	Specific volume
t	Time
λ	Cell size
R	Perfect gas constant, Ratio of the shifted light to the unblocked light
τ	Induction time
E	Energy, Activation energy
θ	Effective activation energy, the refraction angle
n	Refractive index
k	Gladstone-Dale coefficient
a	Height of allowed light
f	Focal length
L	Optical deep
X,Y	Axis
G	The ratio of the deflected angle
Ω	Detection angle
f_B	Boltzmann fraction of OH in the ground state
Γ	Dimensionless overlap integral
I_v	Normalized spectral laser irradiance
I_b	Dimensionless factor accounting for the light sheet absorption
N_{OH}	OH radical density
B	Einstein coefficient
Q	Quenching rate
A	Einstein coefficients
I	Ionic probes

CONTENTS

1   INTRODUCTION

Since the nineteenth century, humanity has made use of oil as a fuel. However, the resource is becoming scarce on our planet. The sustainability vision requires that any process needs to be in harmony with the environment, society, and the economy; to do that, we need new alternatives that meet these three goals. Nowadays, the combustion community is focused on alternative fuels since it offers an exciting alternative to hydrocarbons in terms of harmful emissions, wear, cost, and availability. To generate fewer pollutants in the environment, research on hydrogen as a fuel is a growing trend in the scientific environment, see Figure 1. Hydrogen is considered as the ideal fuel to be burned, in terms of pollution, since it generates fewer pollutants compared to diesel, natural gas, and other fuels that have carbon in their chemical bonds.

Figure 1 -Publications made per year related to Hydrogen-air.
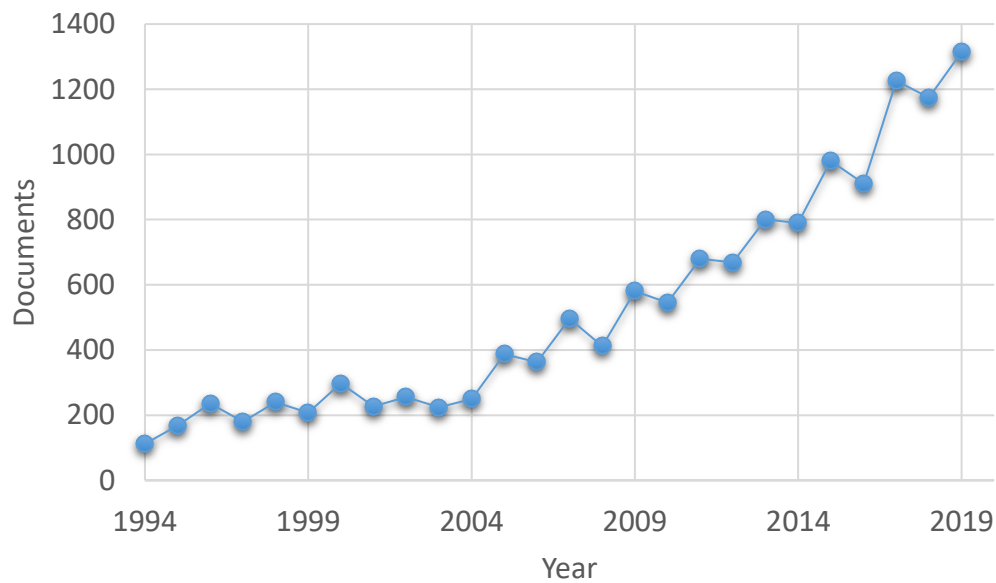
Scopus (2019)

In addition to reducing greenhouse gas emissions, scientists are currently focused on improving the thermodynamic cycles that are used for electricity production. The need for more efficient combustion-based cycles has brought much attention to pressure gain combustion cycles in recent years (GRAY; LACOSTE, 2019; RANKIN et al., 2018). The pressure generated by the

use of detonations substantially improves the performance of gas turbines and propulsion systems. Zeldovich and Jacobs determined that a thermodynamic cycle based on pulse detonation combustion (PDC) had the potential to be more efficient than the isobaric Joule (Brayton) cycle predominantly used in gas turbines (GRAY et al., 2017). Thermodynamic calculations have shown that the efficiency of the "Zeldovich cycle" (detonation combustion cycle) can theoretically be up to 20 and 30% higher than the efficiency of the constant pressure combustion cycle (FROLOV; AKSENOV; IVANOV, 2015). As shown in Figure 2, the well-known Brayton cycle ideally works through four processes: isentropic compression, isobaric heat addition, isentropic expansion, and isobaric heat rejection. The crucial change for the detonation cycle is the addition of heat at isochoric conditions instead of isobaric. By doing that, the engine is able to generate more work by using less amount of energy released by the fuel and then increase the thermal efficiency (LISANTI; ROBERTS, 2017).

Figure 2 -Thermodynamic benefit of pressure gain gas turbine
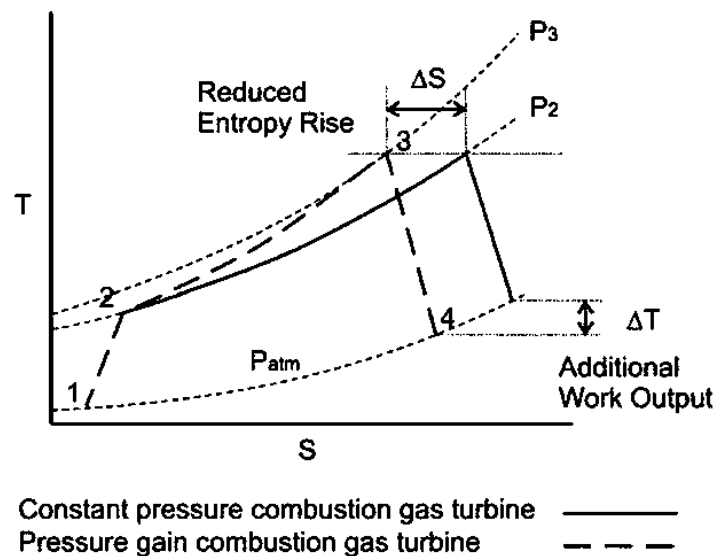
Lisanti; Roberts (2017)

The detonation cycle is not only related to energy generation, but it also can impact the propulsion. Pulse detonation engines (PDE) and Rotating detonation engines (RDE) are the most promising application for detonation. The purpose of these devices is to replace the combustion chamber of a gas turbine to supply more work, as was shown in Figure 2. The first PDE was

designed by Nicholls, Wilkinson, and Mor (1957) at the University of Michigan; the current designs remain similar to the one built by Nicholls's team, Figure 3 shows their design. An important fact to be mention is the absence of commercial detonation engines; this is due to the complexity in state of the art and the lack of physical and chemical knowledge.

Figure 3 -Pulse detonation engine
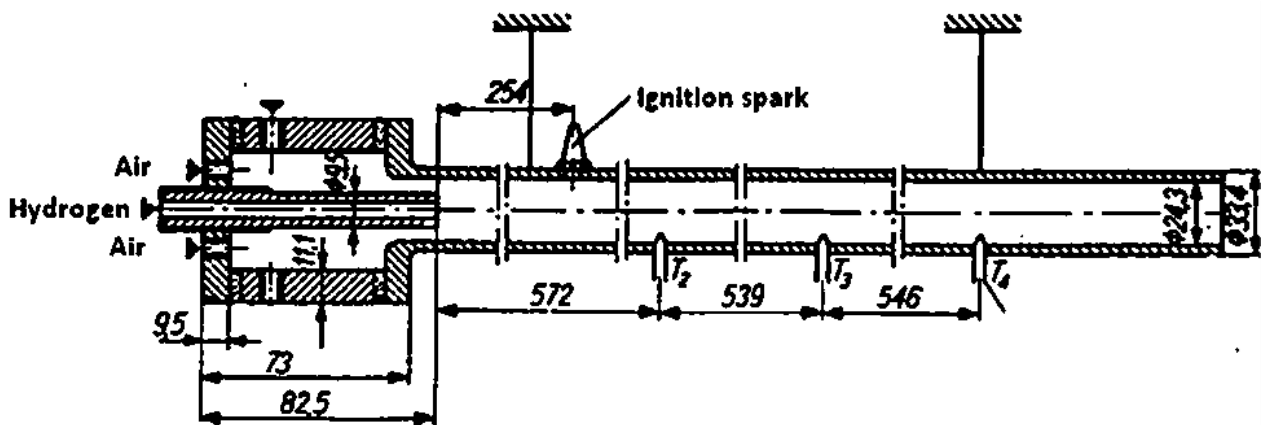
Nicholls; Wilkinson; Mor (1957)

In order to improve the energy efficiency of the thermal devices that generate energy and with the desire to generate fewer pollutants, fundamental studies are needed to understand the detonation phenomenon. Research related to this phenomenon dates from the nineteenth century when, after the discovery of the phenomenon, Chapman (1889) and Jouguet (1904, 1905) developed a quantitative theory that predicts the rate of detonation of an explosive mixture. In the following years, due to the great need for military applications, Zeldovich (1940), von Neumann (1942) and Doring (1943) described the detonation structure model as comprising a leading shock front followed by a chemical reaction zone (LEE, 2008). The theoretical principles provided by the scientists mentioned above has allowed investigations to be carried out today to understand the phenomenon of detonation as well as to apply the principles within new thermodynamic cycles.

Since combustion takes part in many engineering applications and is a complex phenomenon to study, it is necessary to differentiate the type of combustion under study in this investigation. Most of the thermal devices that make use of this process work via deflagration; this is one of the

two modes of propagation, where the molecular transport of heat and mass is essential. The slow mode of combustion is called deflagration; it is called so because the speed of propagation is subsonic. At roughly constant pressure, the chemical reactions occur. For gaseous fuel-air mixtures at equivalence ratio one and atmospheric conditions, the laminar burning velocity is typically less than 1 m/s. Transport properties are enhanced for turbulent flames, and as a result, the burning velocity can be significantly higher than the laminar value (CICCARELLI; DOROFEEV, 2008). The other mode of propagation is detonation; this type of combustion will be studied in this investigation. Detonation is a supersonic combustion wave characterized by an exothermic chemical reaction that takes place behind a strong leading shock front. Due to the increased pressure and temperature behind the shock wave, the reactive material ignites after a short time, the induction time. The volume expansion caused by the substantial increase in temperature during the exothermic reaction drives the shock. This leads to a coupling between the shock and reaction fronts. The chemical reaction is shock-induced as opposed to being controlled by heat conduction or diffusion, as observed in ordinary flames (PINTGEN, 2005). The range of pressure ratio across the detonation wave is in the range of 15–20, for stoichiometric fuel-air mixtures (CICCARELLI; DOROFEEV, 2008). It is essential to mention that only under certain conditions might happen a transition from deflagration to detonation, and this phenomenon is called DDT.

Some of the most relevant studies in detonation show the next progress: Kessle, Gamezo and Oran (2010) simulated using a single-step reaction mechanism for flame acceleration and deflagration-detonation (DDT) transitions in large clogged channels filled with a stoichiometric methane-air mixture. Davidenko et al. (2014) implemented a laser-induced fluorescence model and used to post-process detonation wave numerical simulation results to allow direct comparison with previous experimental visualizations of detonations in hydrogen-oxygen-diluent mixtures. Shepherd (2009) reviewed recent progress in gas detonation experimentation, modeling, and simulation. They focused on the propagating detonation wave as a fundamental combustion process. The evolution of a temperature gradient on detonation was investigated by Liberman, Kiverin and Ivanov (2011) for the combustion mixture whose chemistry is governed by detailed chemical kinetics. He has shown that the minimum length of the temperature gradient to which a detonation can be ignited is much larger than predicted from a one-step chemical model. Austin, Pintgen and Sheoherd (2005) carried out an experimental study, taking images of detonation fronts for several fuel-oxidizer mixtures, including hydrocarbon–air systems showing the effect that the

higher reduced activation energy has a markedly different structure than those with low activation energy.

In order to provide new insights into this phenomenon, it is necessary to perform theoretical, experimental, and numerical studies. It was noticed in the previous paragraph that for investigations related to detonation exist two tendencies, experimental and simulations studies. Both of them are highly linked to each other, especially experimental studies that characterize the shock wave and reaction zone using optical diagnostics like Schlieren, shadowgraph, planar laser-induced fluorescence (PLIF), Coherent anti-Stokes Raman spectroscopy (CARS). Results obtained from images coming from these techniques are valuable for validation purposes, so the main goal for this study is to provide new experimental data that will help numerical models to be validated and improved. An example of a validation process is the study performed by Chatelain (2019) who crosschecked its model by using experimental data taken for two different configurations of laser sheet orientation, see Figure 4. The experimental data used for this study was at 45.3 kPa and 20 kPa, both at 295 K of the initial condition. This model was only validated at those conditions because of the lack of paper available on the web, which justifies the purpose of this study to provide new information.

Figure 4 -Comparison between the experimental and numerical OH-PLIF images. (a) Experiment; (b) Simulation. Conditions: $2H_2$-O_2-10Ar at P = 45.3 kPa and T = 295 K.

a) Experimental OH-PLIF   b) Numerical OH-PLIF

Chatelain et al., (2019)
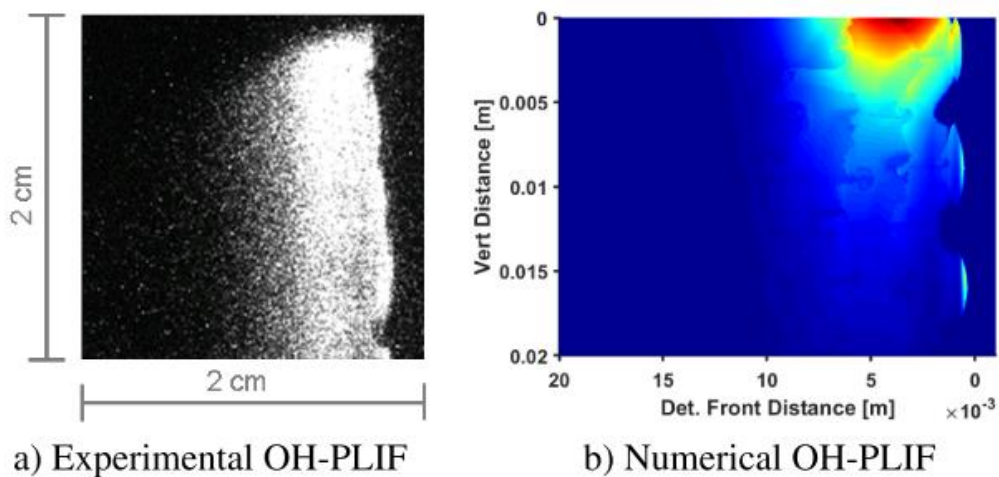
For this reason, taking advantage of the lack of studies that provide reliable images to compare experimental results and numerical simulations, this research aims to characterize detonations of hydrogen-air using well-known techniques in the combustion community, Schlieren, and PLIF at different initial conditions. It is worth to mention that the previous studies realized measurements at unrealistic conditions compared to engineering applications like turbines, the present study aims to work slightly closer to real conditions, and so to deal with its inherent challenges.

The main objective of this study is to characterize the detonation phenomena of hydrogen-air by applying optical diagnostic techniques. To achieve the main objective, three specific objectives were proposed. The first one is to perform experimental measurements in a detonation setup, so before to get Schlieren and PLIF images, it is necessary to obtain reproducible detonations. The detonations measurements performed are related to the pressure and velocity of the shock wave to recognize if the strategy helps to achieve the Chapman-Jouguet (CJ) condition. The second objective is to use the optical technique called Schlieren, to visualize the gradient of density. Since finding a planar wave is crucial for validation of numerical simulation, Schlieren will be the technique to be used at the beginning because the images will enable us to see if the detonation front is 2-D planar or not. Thanks to high spatial and temporal resolution, Schlieren photography will provide information about the density gradient in shock waves using the refraction of the light in inhomogeneous media. The last objective is to perform OH density measurements in the detonation front by adapting the technique planar laser-induced fluorescence (PLIF) that will be used to detect the reaction zone.

The dissertation begins with a theoretical background of the detonation phenomenon, explaining the first theory created by Chapman-Jouguet, then the modern theory called ZND developed by Zel'dovich, John von Neumann and Werner Döring, hence the name, where the relevant features regarding the detonation structure will be pointed out. The third chapter will be discussed the optical techniques that will be used to reveal the physics of the phenomenon under study. The first technique is Schlieren following by planar laser-induced fluorescence, where will be elucidated the scientific principles to interpret the results and how to apply the technique correctly. The third chapter will show the experimental set-up for the detonation, Schlieren, and PLIF system. Furthermore, this chapter will explain the different strategies carried out in the lab to achieve a detonation. Finally, chapters four and five will present the results and conclusion.

2   THEORETICAL BACKGROUND

To understand the physics behind detonations is necessary to explain previous concepts related to combustion. There are three crucial elements to perform combustion; they are fuel, oxidant, and amount of energy necessary to ignite the mixture of fuel-oxidant. The interaction among these elements will create an energetic gaseous reactive medium, called flame; this reaction zone is subject to a specific volume where numerous chemical reaction takes place. Adding to that, radiation and diffusion of species and heat are happening at the same time. Flames can be categorized into two types: diffusion flames and premixed flames. Premixed flames are constituted by a homogeneous mixture of fuel and oxidant in which the flame propagates in direction to the unburnt mixture at a certain speed given by the composition of the mixture and its equivalence ratio. For diffusion flames, the fuel and oxidant are separated, so the flame is in between the fuel-product and the oxidant-products to where they diffuse (MÉVEL, 2018). Figure 5 illustrates the propagation mechanism of the premixed flame (blue) and diffusion flame (yellow). An important fact to be mention for future consideration is that detonation can only occur in a premixed mixture.

Furthermore, flames can propagate into two modes: deflagration and detonation. Heat and mass transfer mechanism governs deflagration. Shock waves might influence on deflagration, but they do not induce it. For deflagration, the unburnt gas is heated until it reaches the temperature when the chemical reactions start; the reaction zone transfer energy to the unreacted mixture through radiation, diffusion, heat, and mass transfer, see Figure 6. Deflagration is also considered as the slow mode of propagation or subsonic combustion.

Figure 5 -The basic structure of a premixed and diffusion flame

Own authorship
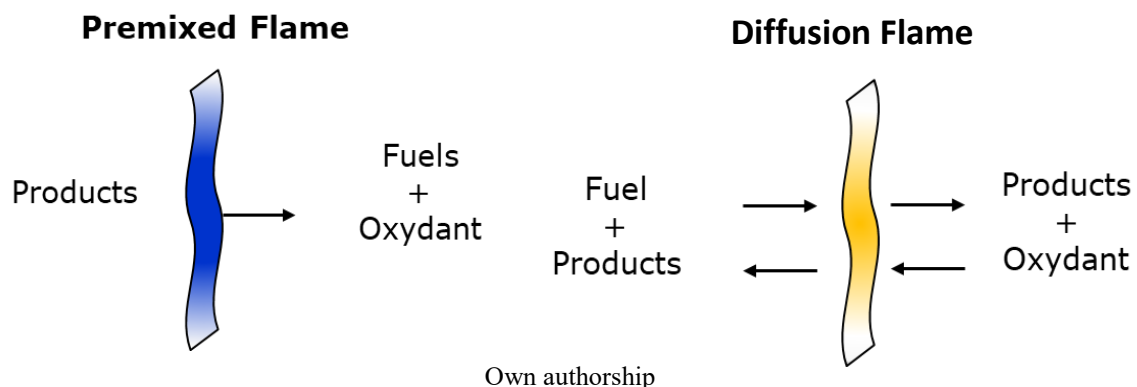
On the other hand, detonation can only propagate in the presence of a shock wave. The shock wave compresses the unburned gas, creating the thermodynamic conditions necessary for the gas to react. In such a way that the shock and reaction fronts are coupled with each other. This type of propagation is also called supersonic combustion, with speeds around 2000 m/s. (PINTGEN, 2000).

Figure 6 -Structure of a laminar flame

Forman (1985)
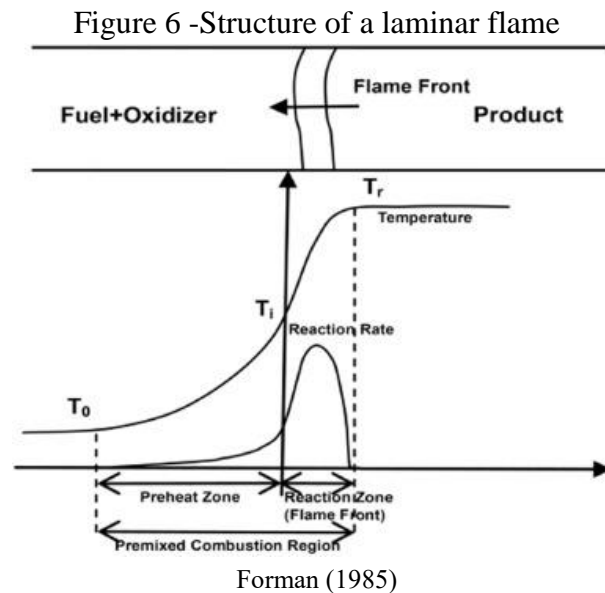
2.1. CHAPMAN-JOUGUET THEORY

This theory was developed independently by two scientists, Chapman and Jouguet (CHAPMAN, 1899; JOUGUET, 1905). The Chapman-Jouguet theory was proposed based on the following assumption: constant propagation speed of the detonations wave, perfect gases, negligible losses in the wall, and a flat and one-dimensional detonation wave. According to this first theory, the detonation wave was considered as a simple hydrodynamic discontinuity of negligible thickness. This assumption infers the spontaneous change from reactants to products, reaching the thermodynamic equilibrium after the shock wave.

The one-dimensional model will be developed in this chapter, considering a flame, whether a deflagration or detonation, as discontinuity, which separates reactants and products. Figure 7 depicts the schematic for the one-dimensional model, considering a flame propagating through a duct, where subscript one means unburnt gas and subscript two burnt gases. For the first position,

the mixture is subjected to the initial condition of temperature and pressure; for the second, the gases are converted into products where are considered to be in thermodynamic equilibrium.

Figure 7 – Schematic of the one-dimensional reaction-front model
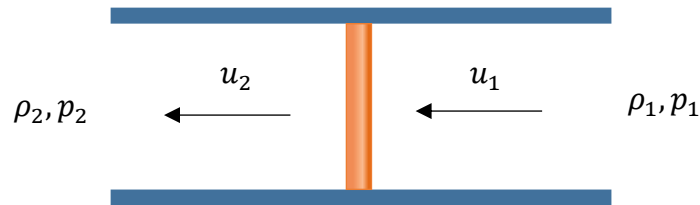
Own authorship

The continuity, conservation of energy, and conservation of momentum equations are numbered (1),(2) and (3), respectively:

$$\rho_1 u_1 = \rho_2 u_2 \tag{1}$$

$$\frac{u^2{}_1}{2} + h_1 = \frac{u^2{}_2}{2} + h_2 \tag{2}$$

$$P + \rho_1 u^2{}_1 = P_2 + \rho_2 u^2{}_2 \tag{3}$$

In which ρ is the density kg/m³, u is the velocity m/s, p is the pressure N/m², and h is the enthalpy J/kg.

Rewriting the continuity equation:

$$u_2{}^2 = \left(\frac{\rho_1 u_1}{\rho_2}\right)^2 \tag{4}$$

Substituting equation (4) into equation (3), taking into account that $\rho_i = {}^1\!/v_i$:

$$P_2 - P_1 = \frac{u_1{}^2}{v_1{}^2}(v_1 - v_2) \tag{5}$$

Equation (5) represents the path of thermodynamics states across the combustion wave. This equation is known as the Rayleigh line.

Multiplying equation of conservation of momentum (3) by $\left(1/\rho_1 + 1/\rho_2\right)$, the following expression is obtained :

$$(P_2 - P_1)\left(\frac{1}{\rho_1} + \frac{1}{\rho_2}\right) = u_1{}^2 - u_2{}^2 + u_1{}^2\frac{\rho_1}{\rho_2} - u_2{}^2\frac{\rho_2}{\rho_1} \tag{6}$$

Substituting equation (4) into equation (6), the following equation is obtained:

$$u_1{}^2 - u_2{}^2 = (P_2 - P_1)\left(\frac{1}{\rho_1} + \frac{1}{\rho_2}\right) \tag{7}$$

Substituting equation (7) into equation (2), it is obtained equation (8):

$$h_2 - h_1 = \frac{1}{2}(P_2 - P_1)\left(\frac{1}{\rho_1} + \frac{1}{\rho_2}\right) \; or \; h_2 - h_1 = \frac{1}{2}(P_2 - P_1)(v_1 + v_2) \tag{8}$$

Equation (8) is well known as the Rankine-Hugoniot curve, which describes the possible solutions between the density and pressure for an adiabatic shock wave and equilibrium state. The Rankine-Hugoniot curve and Rayleigh line are plotted in Figure 8.

Figure 8 -Diagram specific volume-pressure for Rayleigh line and Rankine-Hugoniot
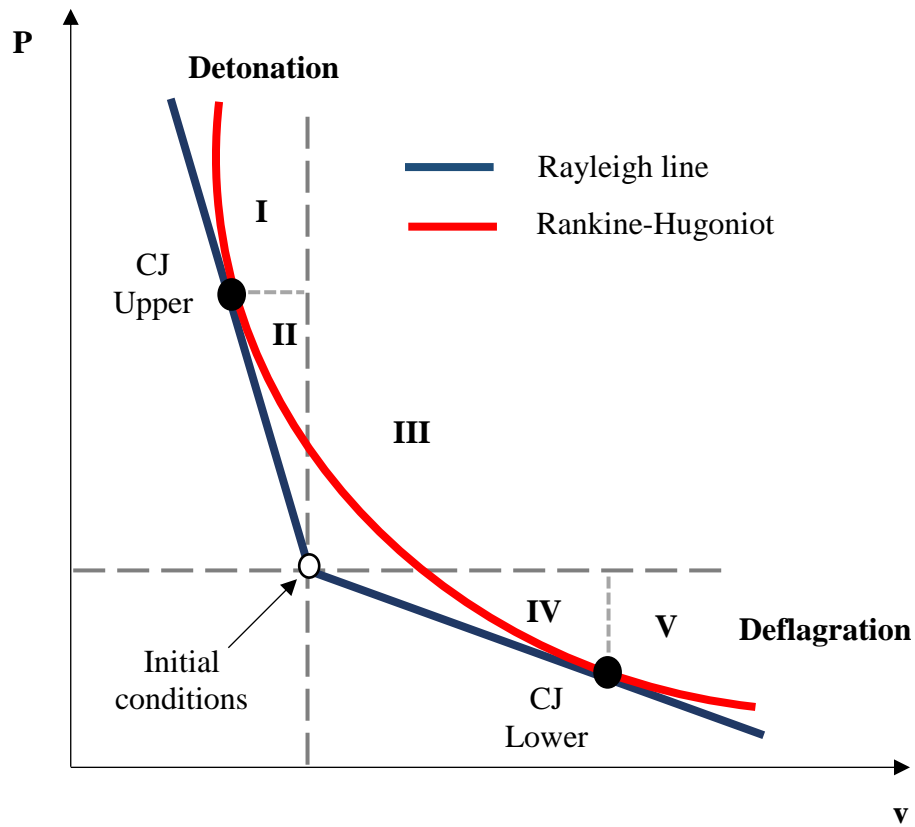
Own authorship

Considering tangent the Hugoniot curve and Rayleigh line, it creates two-point called Chapman-Jouguet upper point and Chapman-Jouguet point condition. The intersection in the upper point creates the solutions for detonation while the lower point the solutions for deflagration. At the same time, these points split two-section called strong and weak solutions. In the area, I and II are registered the supersonic regimen of combustion. For detonation located above the CJ upper point, the solutions contain over-driven detonations, whereas for the detonations below this point are considered weak, both solutions are unsteady conditions that are commonly obtained experimentally. Area III depicts imaginary solutions. The areas IV and V are the solutions for deflagration or subsonic combustion. As detonation, the intersection point, in this case Chapman-Jouguet lower point, creates two are of solutions. Area IV is the strong deflagration and area V weak deflagration. As can be seen in Figure 8, across the detonation wave, the gases are compressed since the specific volume is decreasing so that it can be called a compression process, whereas, for

deflagration, the gases are expanding since the specific volume increase. Nowadays, this one-dimensional model is still used to estimate the Chapman-Jouguet velocity accurately. Equation (9) expresses the Chapman-Jouguet Velocity, considering the intersection between the Rankine-Hugoniot curve and Rayleigh line, which means a self-sustained propagating detonation.

$$u_1 = u_{CJ} = v_1 * \sqrt{\frac{P_2 - P_1}{v_1 - v_2}} \tag{9}$$

2.2. ZELDOVICH-VON NEUMANN-DOERING THEORY

The ZND theory, also called the modern theory of detonation, was proposed by Zeldovich, von Neumann, and Doering, hence the name (DOERING, 1943; VON NEUMANN, 1942; ZELDOVICH Y.B, 1940). This one-dimensional theory was proposed during World war II but developed independently. The ZND theory is based on the CJ theory; however, new assumptions were proposed. One of the differences between both theories is the consideration made in the modern theory regarding the structure of the detonation; this theory proposed the double discontinuity consisting of a shock wave and a reaction zone behind the shock.

A schematic of the new features proposed by the ZND theory is shown in Figure 9. As mentioned in the previous paragraph, the detonation is composed of a leading shock wave following by a reaction zone. Between these two discontinuities exist the induction zone, the length of this zone depends on the initial conditions like compositions of reactants, temperature, pressure, equivalence ratio, amount of dilutant, and position respect to the cellular structure. Overall, the detonation structure is divided into five elements: fresh gases, shock wave, induction zone, reaction zone, and burnt gases.

Figure 9 -Schematic of the main features given by the ZND theory

Own authorship
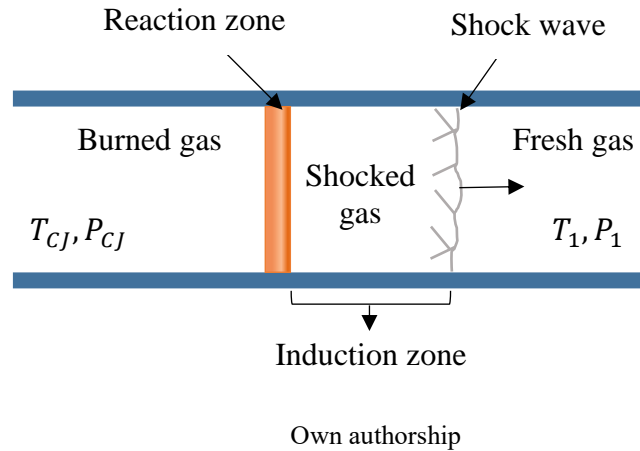
Figure 10 represents the development of the pressure and temperature across the detonation. The propagation of the detonations goes from the left to right, but the evolution of the state variables is reading from right to left. Considering the pressure and temperature of the reactants at given initial condition P_0 and T_0, respectively. The mixture goes through the shock wave where it is heated and compressed until reaching the von Neumann peak conditions; this process happens spontaneously without any chemical reaction. When the peak has been reached, the pressure and temperature stay almost constant at the ZND state while it is located in the induction zone. Due to the elevated pressure and temperature, chemical reactions happen during this stage; the formation of radical through chain branching processes occur. Once the gaseous mixture leaves the induction zone, energy is released exothermically by trimolecular recombination reactions, and this stage is called the reaction zone, where the pressure decrease, whereas the temperature increase. Finally, the products leave the reaction zone at Chapman-Jouguet conditions (MÉVEL, 2018; PINTGEN, 2000). Figure 12 depicts the path of the reactants through the shock wave, considering it as an adiabatic process, where the VN peak is achieved in the intersection with the Rayleigh line. The solid black line represents the changes in the pressure and specific volume generated by the interaction with the shock wave. Once the reactants reach the necessary conditions to trigger the chain branching process of radical and subsequently release its energy in the reaction zone, they intersect the Chapman-Jouguet state.

Figure 10 -Pressure and Temperature diagram of detonation, according to the ZND theory.

Adapted from Pintgen (2000)
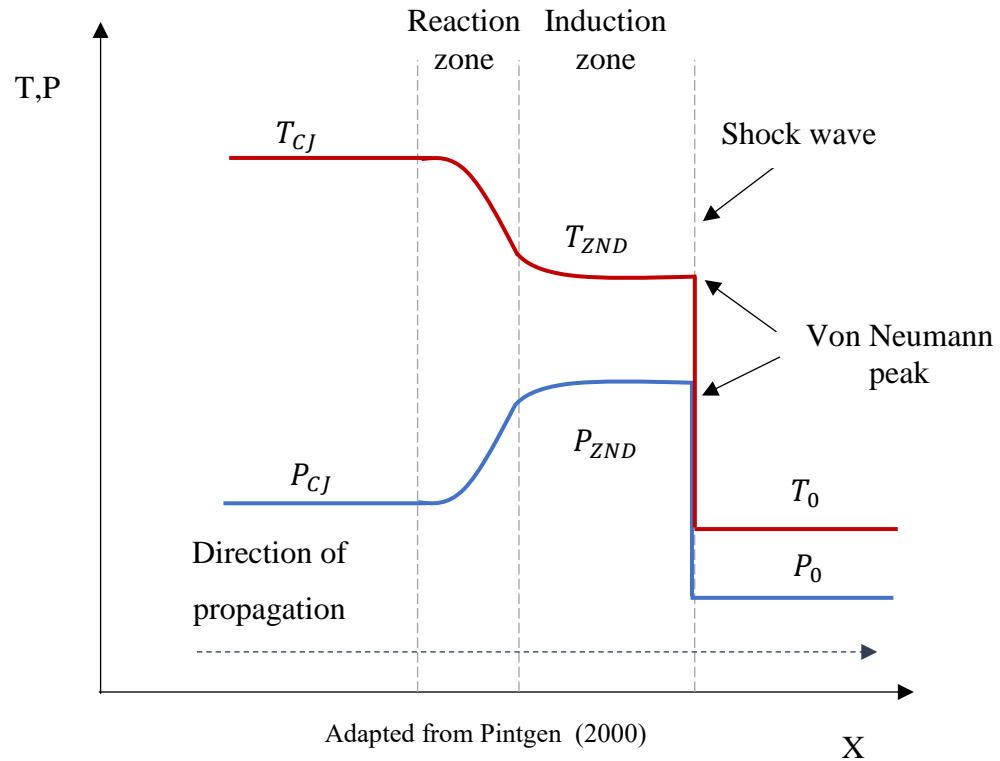
Figure 11 -Pressure-specific volume diagram for the ZND theory

Adapted from Pintgen (2000)
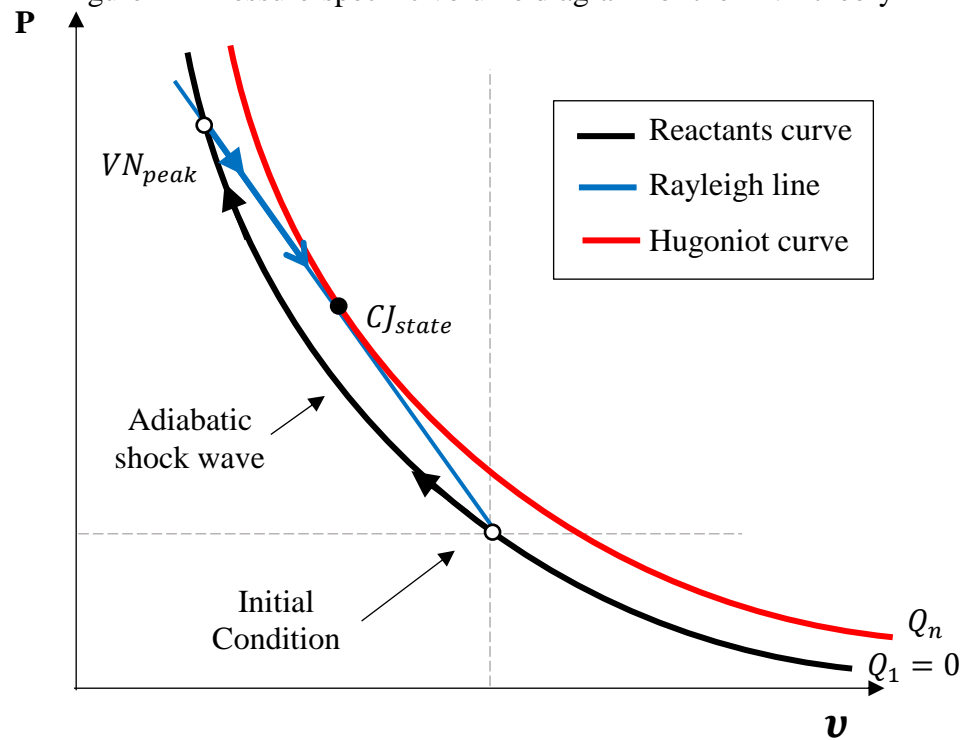
2.3. DETONATION WAVE STRUCTURE

According to the mentioned theories, the structure of both instabilities, reaction zone, and shock wave are planar, one-dimensional, and steady. Experimentally this behavior has not been detected since the detonation front, in reality, shows curved and planar sections. An intrinsic feature of detonations is its tridimensional structure, composes by the three different waves: incident waves, transverse waves, and mach stem. The structure is not constant over time since some instabilities created in the reaction zone affect the shock front directly because of its coupling. Furthermore, detonations are characterized by its cellular structure, which is profoundly influenced by the mixture compositions and amount of dilutants; the main effect is appreciated in the cell-size regularity.

A shock wave reflection phenomenon similarly creates the cellular structure obtained in the detonation front. The schematic of this phenomenon is shown in Figure 12. The structure of a Mach reflection, happening in non-reactive flow, shows the same structure recorded in detonation, using the soot-foil technique. There is not a clear understanding of how works the mentioned technique, but according to Pintgen (2000) a possible explanation for this technique relies on the high pressure created in the triple, which compiles the soot to the foil, so leaving a path of dark lines.

Figure 12-Schematic of Mach reflection
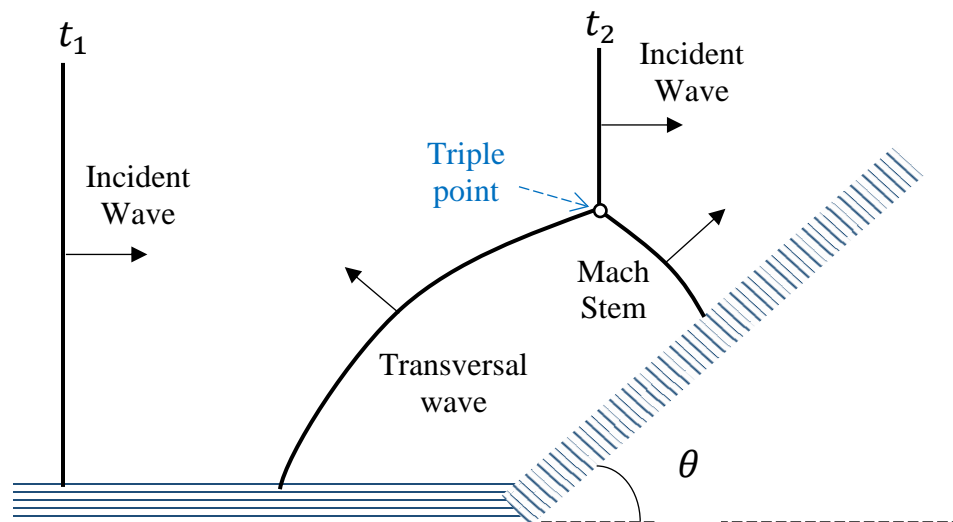
Adapted from Pintgen (2000)

Mach stem reflection happens on wedges, under specific parameters like the angle (θ) of the wedge and the velocity of the incident shock. If those requirements are not met, two possible structures might happen: the incident wave might follow the direction of the wedge, or a creation of the reflected wave parallel to the wedge surface is created. To confirm that a Mach reflection is formed, it is necessary to obtain three waves: incident wave, reflected wave or transversal wave, and Mach stem. In Figure 12, a supersonic incident wave is illustrated at initial time t_1, when the incident wave hits the tilted surface, the Mach stem phenomenon happens, creating a perpendicular wave called Mach stem and a reflected wave. The element that connects the system of waves is called the "triple point." Currently, the techniques applied to detect the cell size is based on the trace that triple point left on their trajectory.

Detonation, unlike non-reacting flows, exhibits multiples Mach reflection on the shock front, so creating a cellular structure as seen in Figure 13. This figure shows the development of the cellular pattern left by the detonation front at the time t_1 and t_2, where the reaction zone is shaded. As can be seen, the reaction zone and shock wave changes its shape along the time, depending on the cellular cycle. The cells begin leading by an overdriven Mach stem wave, which induces fast reaction due to their condition, so obtaining a short induction length between the shock wave and reaction zone. When the wave is close to the half, its velocity decreases, and so the reaction rate. At this stage, the Mach stem wave becomes an incident shock wave. When this transition happens, the triple points above and below the cell collide each other. Since then, a decoupling process occurs until the end of the cell, reaching 60% of the cell Chapman-Jouguet velocity. In this second half of the cell transverse wave interact with the unburnt mixture, shocking it for the second time, before the mixture goes through the reaction zone. Despite the negative trend of the velocity along the cell, experiments have shown that both parameters decrease up to three-quarters of the cell and then increase in the last quarter (PINTGEN, 2000).

One way to characterize detonations is by the regularity of the cell size. According to previous experimental studies, the definition of the cell size is the maximum vertical distance between two apexes. Other studies use the longitudinal distance between two transverse wave collisions; this is called cell length. These dimensions are strongly affected by the reactant composition and initial thermodynamic condition. Figure 15 shows the study performed by (AUSTIN, 2003) regarding the influence of the reactant composition on the regularity of the cell-size. Hydrogen, unlike propane, shows a regular formation of the cell, whereas working with

propane shows a wide range of cell sizes, even running at different percentages of dilution. For hydrogen mixtures, a high concentration of argon has shown excellent results on the regularity, unlike nitrogen. Despite the available cell-size database for different conditions, the reason when the cells behave regularly is not fully understood. Nonetheless, there is another approach that explains the irregularity as an amplification factor of disturbance in reacting flows. The name of this parameter is the effective activation energy, which is shown in equation (10).

$$\theta = \frac{E_i}{RT_{VN}} = \frac{1}{T_{VN}}\left(\frac{\ln \tau_2 - \ln \tau_1}{\frac{1}{T_2} - \frac{1}{T_1}}\right) \tag{10}$$
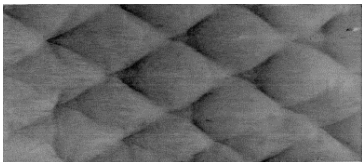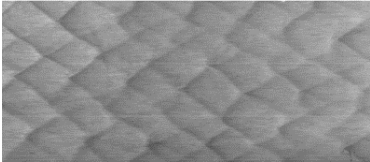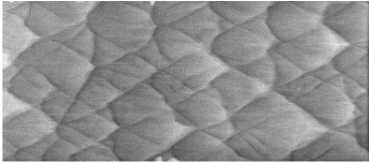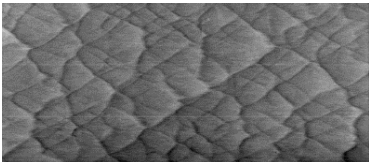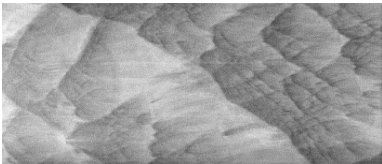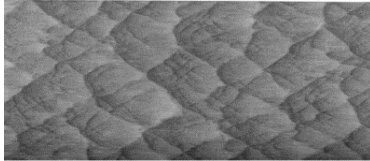
In which E_i is the activation energy, R is the perfect gas constant, T_{VN} is the temperature at von Neumann state. The induction times τ_2 and τ_1, corresponds to the period that the mixture spends from the von Neumann state until the maximum intensity of OH radical. These times are simulated at two temperatures close to the VN state, T_2 and T_1. These states are generated by varying Champman-Joughet velocity by ±1%. The higher the effective activation energy, the more irregular cell structures are found (AUSTIN, 2003; PINTGEN, 2000).

Figure 13 -Schematic of cellular structure and its involved shock waves
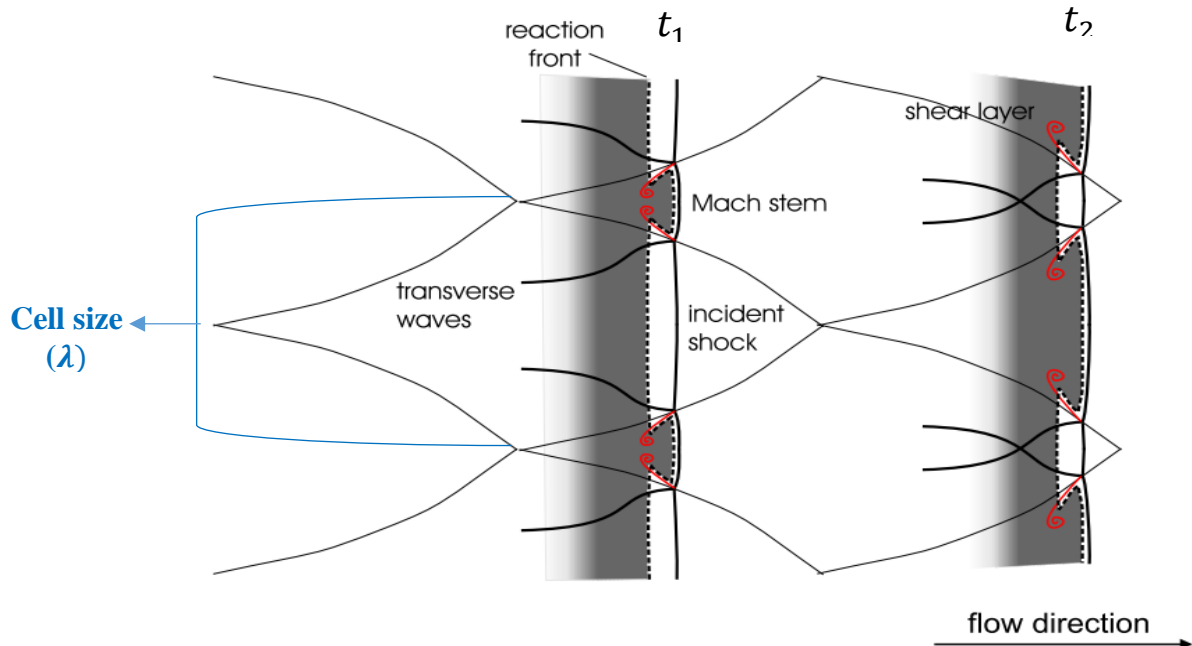
Adapted from Pintgen (2000)

Figure 14 -Cell size regularity affected by the mixture composition

Mixture	T=298 K and P=20 kPa, for every mixture	
$2H_2 - O_2$	Ar= 85%	Ar= 80%
$2H_2 - O_2$	N_2= 60%	N_2= 54%
$C_3H_8 - O_2$	N_2= 77,7%	N_2= 75%

Adapted from Austin (2003)

2.4. DETONATION INITIATION IN OBSTRUCTED CHANNELS

Detonation can occur either in confined or unconfined geometries. However, the mechanism that involves its initiation works differently for each one. One way to start detonation inside a tube is placing obstacles to generate transition from deflagration to detonation. Figure 15 provides a mechanism that explains the production of fast flames and detonations for obstructed channels.

Figure 15 -Sequence of steps for flame acceleration and detonation initiation
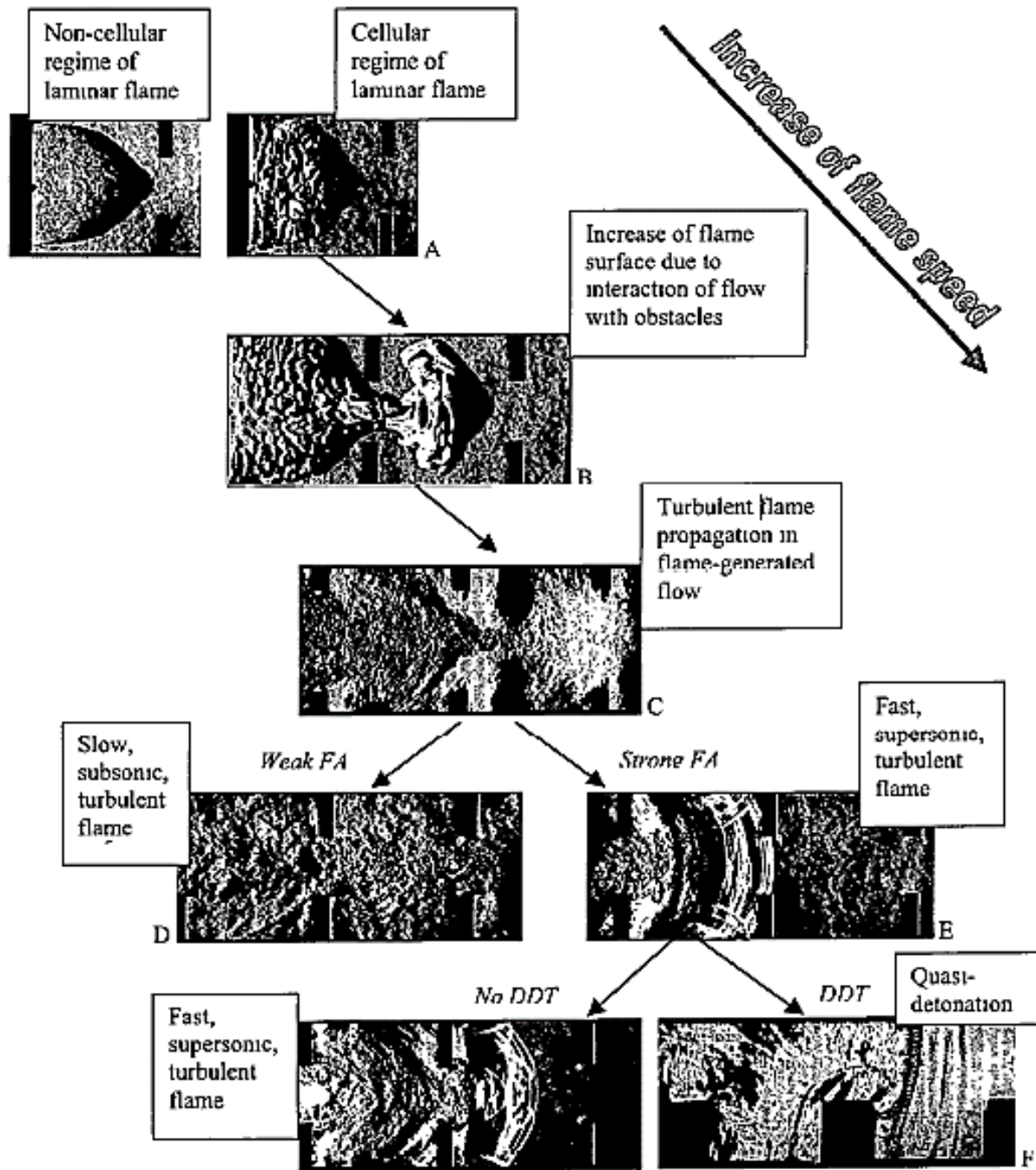
Dorofeev (2002)

The sequence begins with the expansion of a laminar flame through a smooth channel. Laminar flame can be unstabilized firstly by Landau-Darrieus instability and thermal-diffusion effects. Landau- Darrieus instability can create a wrinkling effect, whereas thermal-diffusion might

stabilize or amplify the instability. Both effects might create a cellular structure in the laminar flame. As the cellular structure is taking place in the flame, the reaction surface grows, so accelerating the rate of products and expansion. Experimental studies have demonstrated that obstacles influence in the acceleration of the flame. The expansion of the products generate movements in the fresh mixture. So the streamline of the unburnt gases which are close to the obstacle induces the increment of the flame surface, leading to further increase in the flame speed. During the continuous acceleration of the propagating flame does not exist any turbulence influence. Eventually, turbulence is created in the combustion induced flow. The effect that turbulence has under the flame propagation is the improvement of the burning rate by increasing the surface of the flame and the transport of local mass and energy. The higher burning rate generates an increment in the velocity in the fresh gases. So the same acceleration mechanism is activated but at a higher intensity. This mechanism is called "The turbulent feedback loop." Turbulent might not only create a successful transition to detonation, but it might also quench the flame as well. This feedback can result in a subsonic and turbulent flame or a supersonic flame; these two possible events are called weak and strong flame acceleration, respectively. This is a crucial step in the DDT. Strong flame acceleration consists of a leading shock wave followed by a turbulent flame. However, only under specific conditions, the fast turbulent flame might become a detonation.

Depending on the thermodynamic conditions, the property of the mixture, and inner geometry, a detonation might occur. An important parameter to achieve a good transition concerning to the geometry is the cell size dimension. The inner dimension of the confined channel and obstacle have to be larger than the cell size to make sure the existence of the intrinsical cellular structure. A clear example is shown in Figure 16, where the influence of the mixture composition influences the velocities profiles along the tube, resulting in most of the cases in failed transition and quasi-detonation.

Obstacles are an excellent option to generate DDT. Nonetheless, its presence along the channel might create a repetitive cycle of failure/re-initiation, so a proper amount of obstacle and a correct blockage ratio have to be chosen. The blockage ratio is the quotient of the obstacle blockage area and channel cross-sectional area.

Figure 16 -Influence of the amount of propane over the velocities profiles in a 174 mm tube (BR=0.3)
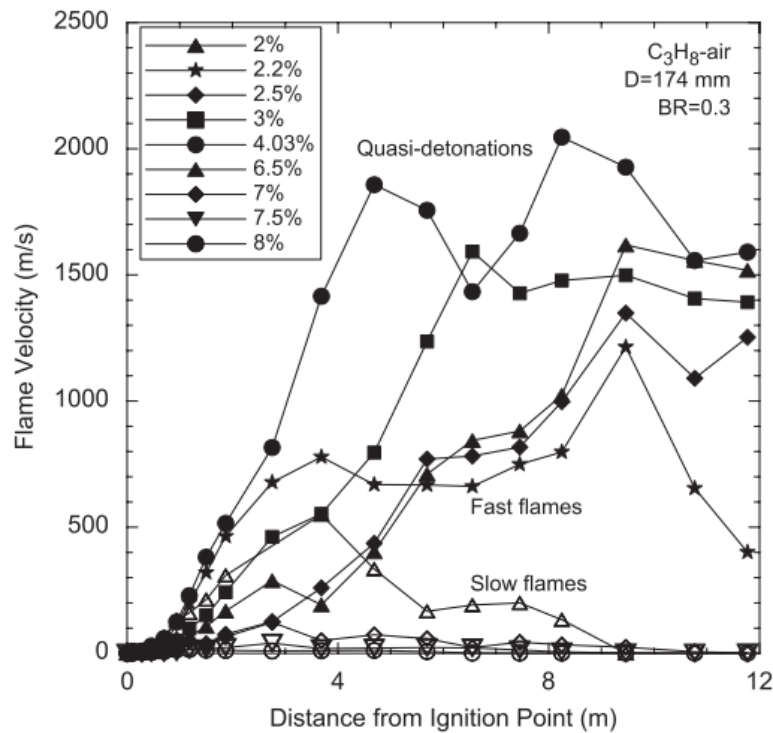
Ciccarelli; Dorofeev (2008)

2.5. SCHLIEREN TECHNIQUE

Schlieren is an optical technique that is considered to be non-invasive. Its visual results are based on the density gradient of the media under study. Indeed, the name comes from Germany, where people working with lenses call "Schliere" to the inhomogeneities created in the lens. This technique has been used in many scientific fields like combustion, fluid mechanics, heat transfer, ballistic, blast waves, aerospace, etc. The operating principle is based on the deflection property of the light created by the density gradient. The primary purpose of using this technique is to perform qualitative studies since it is almost impossible to obtain quantitative results about the density gradient because of the complexity of the geometry under study. The source light which travels across the media deflects multiple times depending on the density field, so it results in an integration of the density across the media. Nowadays, there are various variations of the Schlieren

system, though the deflection of light principle is applied for each of them (PINTGEN, 2000; SETTLES, 2001).

Light tends to propagate, keeping the same angle in a media with constant density, also called homogeneous media. Light properties might change the perception of our reality; how star look to our eyes is the most evident example. Stars lights travel throughout at nearly constant media in the space; however, when it reaches the atmosphere, the light suffers refraction by many disturbances that take place in this media. This is the reason why the starlight looks twinkle and not a point. The refraction property of the light that takes place in the atmosphere can also help us to unravel the physics within the detonation phenomenon. Figure 17 shows the light behavior when it goes through different media. The media are characterized by different indices refraction, which depends on the density. Snell's law governs refraction, see equation 11. This equation shows the dependence of the angle deflection and velocity in the media concerning the index refraction. As can be seen in Figure 17, three hypothetic cases are shown, each one with different refractive indices. For angle θ_2, the angle is much smaller than the incident angle θ_1, which means that the refractive index two is higher than the refractive index one. For angle θ_3, its value is the same as θ_1, which means both refractive indices are the same since there is no deflection in the light. For angle θ_4, the deflected angle is bigger than θ_1, therefore the index refraction is lower. According to the interpretation of this law, the incident light is deflected toward the normal of the second media; if the index refraction is more significant or the material denser, the opposite behavior happens with lighter materials.

$$\frac{\sin \theta_1}{\sin \theta_i} = \frac{n_i}{n_1} = \frac{v_1}{v_2} \tag{11}$$

The refraction index directly depends on the density of the material, the following equation valid air, and other gases express its linear relationship.

$$n - 1 = k\rho \tag{12}$$

Where n is the refraction index, k, is the Gladstone-Dale coefficient, and ρ is the density of the media. The dependence of the refraction index respect to the density is used to visualize the density gradient in combustion application, using two techniques, Shadowgraph and Schlieren.

Figure 17 -Light refraction angle as a function of the refractive index
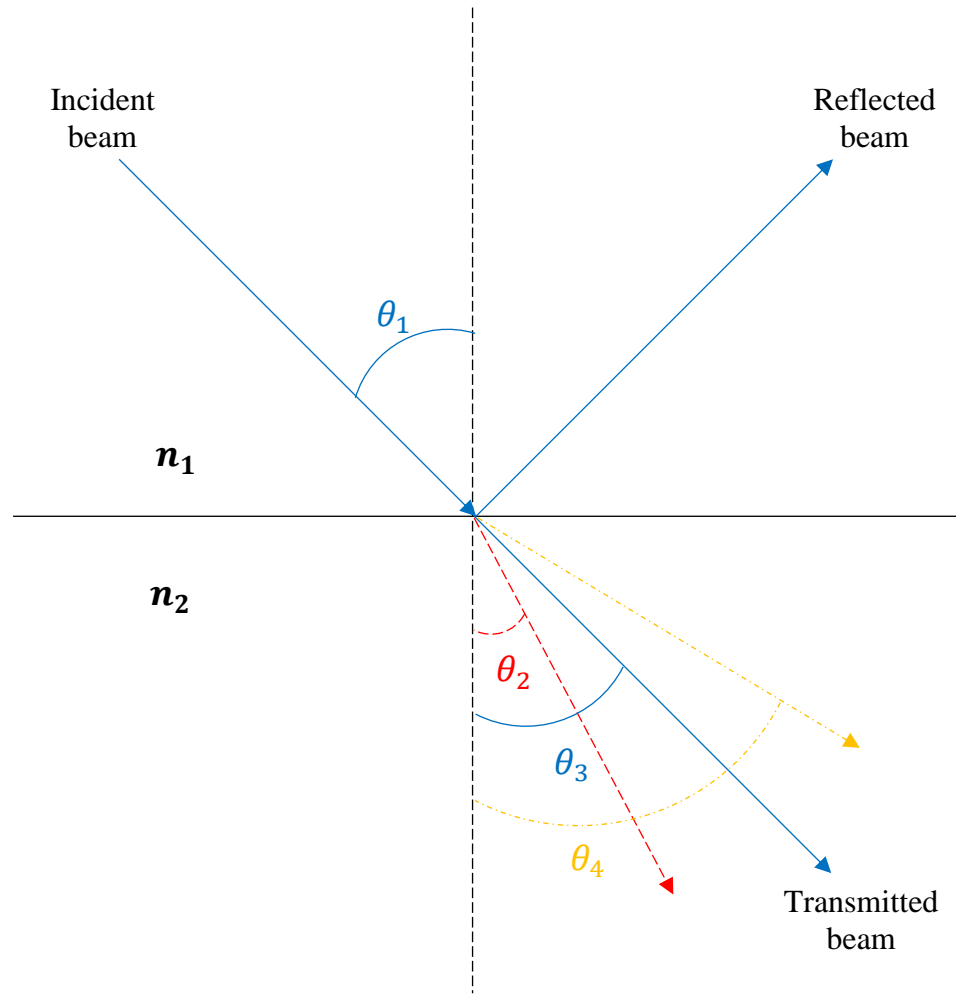
Own authorship

Let us assume a cartesian plane with x, y, z coordinate system, considering z coordinate as normal respect to the optical plane where the light goes through. X-Y coordinates represent the planes perpendicular to light propagation. In such a way that the optical inhomogeneities refract the coming the light based on the gradient of the X-Y plane. So the ray curvature is expressed in the following equation:

$$\frac{\partial^2 x}{\partial z^2} = \frac{1}{n}\frac{\partial n}{\partial x} \quad , \quad \frac{\partial^2 y}{\partial z^2} = \frac{1}{n}\frac{\partial n}{\partial y} \qquad (13)$$

Realizing integration respect to coordinate z where the light travels, the angular deflection in the X-Y coordinates are:

$$\varepsilon_x = \frac{1}{n} \int \frac{\partial n}{\partial x} \partial z \quad , \quad \varepsilon_y = \frac{1}{n} \int \frac{\partial n}{\partial y} \partial z \tag{14}$$

Considering a two-dimensional system with L of optical deep and n_0 as the refractive index of the surrounding medium, equation 14 becomes into:

$$\varepsilon_x = \frac{L}{n_0} \frac{\partial n}{\partial x} \quad , \quad \varepsilon_y = \frac{L}{n_0} \frac{\partial n}{\partial y} \tag{15}$$

The given mathematical expressions are useful to understand optical techniques, Schlieren and Shadowgraph. The last method projects a mere shadow, which results from the second spatial derivative $\frac{\partial^2 n}{\partial x^2}$. Schlieren, unlike shadowgraph, provides the information of the first derivative of the index refraction $\frac{\partial n}{\partial x}$. Meaning that Schlieren displays the deflection angle of the light beam (ε), whereas shadowgraph shows the displacement (Δa), see figure 18.

Figure 18 -Direct shadowgraph setup

Settles (2001)
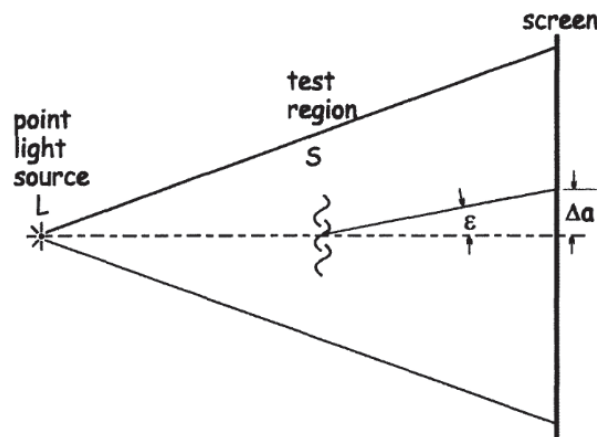
One crucial difference in applying these techniques is the use of a knife; Schlieren needs to cut part of the reflected light using a knife, whereas Shadowgraph does no need. Nonetheless, shadowgraph is a very attractive method since it is more straightforward to install. Since the Schlieren technique has been chosen to perform experimental imaging of detonations, the following paragraph will explain more details about this specific technique.

Figure 19 shows the simple Schlieren arrangement, which consists of a point source, collimated lenses, knife-edge, and a screen to display the image. The beam emitted from the point source is most of the time diverging, so a collimated lens is necessary to become the diverging beam into parallel light, which goes through the media under study. A second lens is placed after the test area to converge the beam into a point. The distance between the lens and point is called the focal point, and its value depends on the type of lens. Schlieren, unlike Shadowgraph, needs a knife to cut part of the deflected light generated by the density gradient on the media. Placing the knife in the focal point provides uniform darkness. Depending on the application, the knife can cut only the deflected light or the image of the light source, by doing this, the perception of density gradient changes as well the intensity of the light projected on the screen.

Figure 19 – Simple Schlieren set up with a point light source
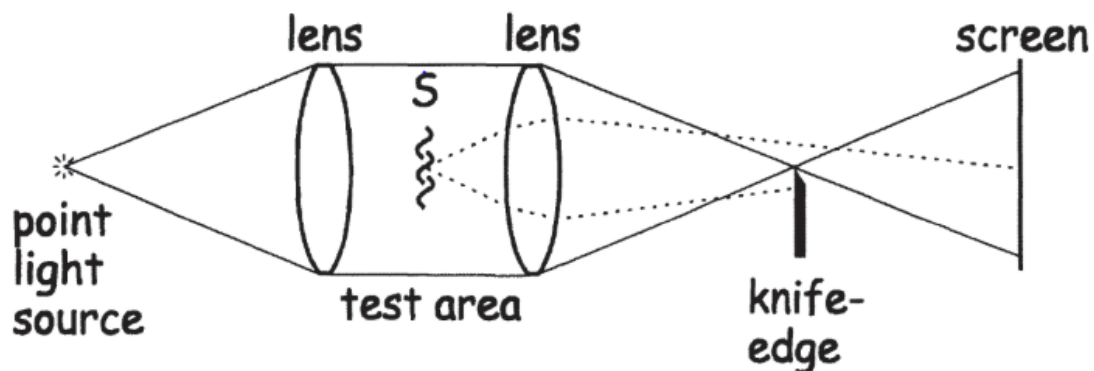
Settles (2001)

The position of the knife-edge is an important factor that needs to be taken into account to obtain reliable results. Figure 19 shows the knife placed in the horizontal x coordinate. This configuration allows only to see the gradient in the y coordinate ($\partial n/\partial y$). For any light beam deflected by the x component gradient ($\partial n/\partial x$)., it will not be detected by this configuration since these beams are hitting normally the knife. The gradients direction has to be known previously to

apply the correct cut-off technique. The influence of the type of cutoff over the contrast of the Schlieren image is shown in Figure 20.

Figure 20-Schlieren image of a turbulent flame of an oxy-acetylene torch using : (a) circular cutoff, (b) vertical knife-edge, and (c) horizontal knife-edge.

(a)　　　　**(b)**　　　　**(c)**
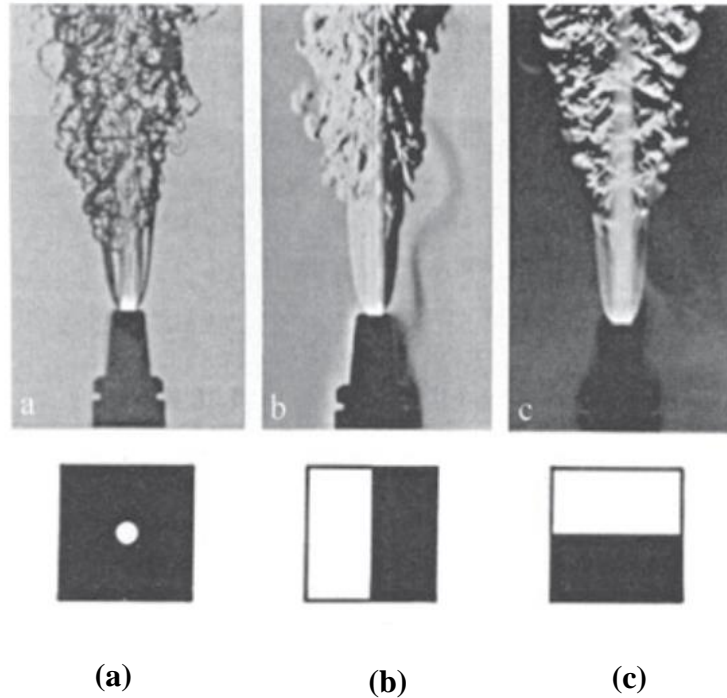
Settles (2001)

The groups of beams leaving the test area gather the deflected and not deflected beams. Even if the second lens is collecting the beams into a point, the deflection will still be projected to screen. The knife-edge is used to block part of the source image, allowing part of the light to create the background. The amount of cut-off affects the contrast of the Schlieren photography. So the image projected on the screen is based on the variation of illuminance intensity created by both the media and the cutoff process.

Figure 21 shows a knife-edge cutting horizontally h-a of the source image. According to the figure, the media have created a deflection of the beam with a vertical displacement of Δa and only allows a portion of light "a." An essential parameter when performing Schlieren is the ratio

of the shifted light to the unblocked light coming from the image source; this is shown in the following equation:

$$R = \frac{\Delta a}{a} \tag{16}$$

Figure 21 -Diagram of a rectangular composite light source after being converged by the second lens and a knife-edge blocking reflected beam in the X coordinate.
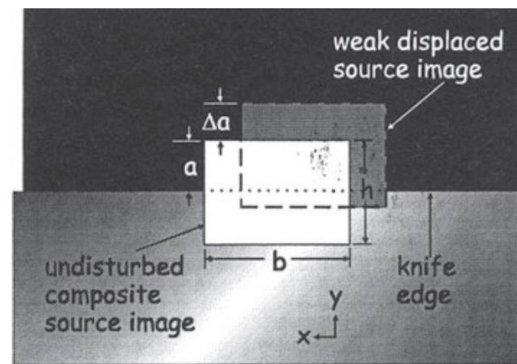
Settles (2001)

The displacement of the deflect light on the vertical coordinates is also expressed as:

$$\Delta a = f_2 \varepsilon \tag{17}$$

Replacing equation 15 and equation 17 into equation 16, results:

$$R = \frac{f_2 L k}{a \, \rho_0} \frac{\partial n}{\partial y} \tag{18}$$

Mirrors are an excellent option to be implemented in a Schlieren system. Likewise lenses, mirrors require a good quality to avoid influence on the results. The most popular configuration using mirrors is the well-known Z-type Mirror Schlieren system. The available mirrors to be used in this system are parabolic, spherical, and off-axis concave mirrors. The most famous Z-type arrangement is the one built by the astronomer William Herschel, see figure 22. This type of system

consists of one light source, two parabolic mirrors, knife-edge, and a camera. This type of configuration is more suitable for application with bigger and complicated access to the optical test region. Since the parabolic mirror converges the beams from a diverging light source, the shape of the configuration is conditioned to look like the letter "Z," hence the name. The main reason to choose mirrors instead of lenses is due to the larger field of view obtained for a given cost (SETTLES, 2001).

Figure 22- Z-type Schlieren setup
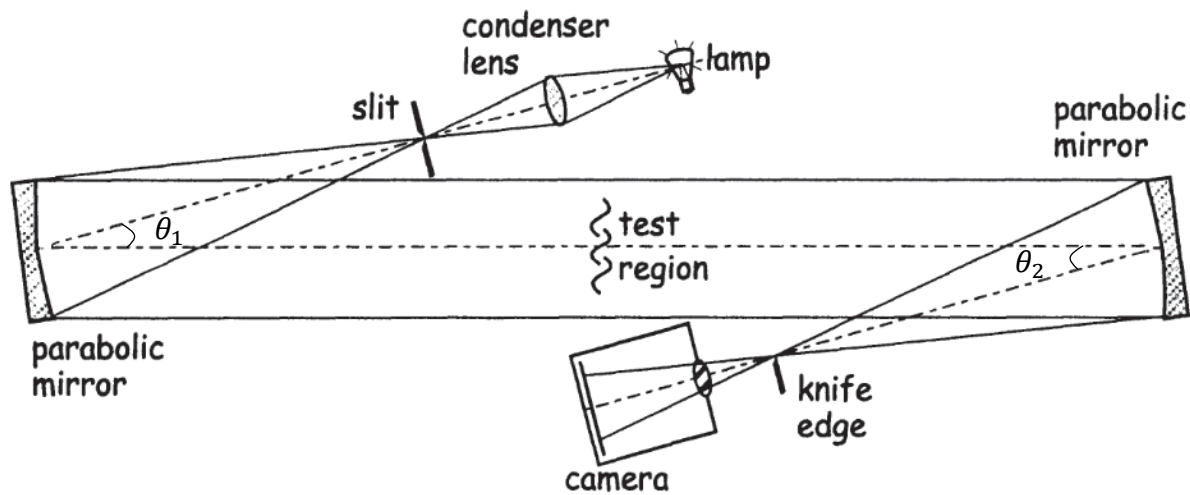
Adapted from Settles (2001)

Despite versatility that Z-type configuration offers, there are some disadvantages when adopting this system. The chief drawbacks are Coma and Astigmatism; both are off-axis aberrations. These problems are created because the optical devices are designed to work at on-axis, so using the z-type configuration the system is off-axis by θ_1 and θ_2. The changes in the angles lead to a not reliable production of the light source image in the second focal point-plane. If some corrections are not taken into account, the result will be an uneven schlieren-image. Coma aberration occurs when the light reflected by a mirror depends on the position where the light converges. Assuming that the light source is a point, the tilted mirrors off the optical axes become the point into a spread line. The point spread proportionally to the offset angle θ. So a possible correction is to decrease as low as possible the mentioned angle; however, in some application, tilting the mirrors at a minimum angle is not possible for space availability. For such setups, there

is another correction that cancels this aberration. By tilting the mirrors at the same angle ($\theta_1 = \theta_2$) in the opposite direction, the coma aberration is fixed. Astigmatism, unlike coma, cannot be canceled, but following the same correction for coma and using mirrors in a range of f/6 to f/12, the aberration can be minimized (SETTLES, 2001).

2.6. LASER-INDUCED FLUORESCENCE

Optical diagnostics techniques are made to unravel the physics and chemistry behind a specific phenomenon. They can provide information about certain variables of interest at a specific point, plane, or area of interest. Laser-induced fluorescence is a powerful tool for the combustion process since this technique helps to detect OH radicals. Identify this radical is crucial to reveal the reaction zone. The OH radical can be uncovered by inducing its emission using a laser at a specific wavelength, that has to be chosen based on the emission spectrum found in the literature and available software.

There are two types of signal casting by emission process; these can be either coherent or incoherent. LIF is an incoherent scattering process since the signal is cast out in different directions from the excited volume. So the fluorescence signal is only detected at a restricted angle, determined by the detector. The equation (19) expresses the portion of the whole emission angle, Ω is the detection angle:

$$G = \frac{\Omega}{4\pi} \tag{19}$$

LIF, laser-induced fluorescence, consists of two-step: the first step is called absorption, and the light emitted by the laser goes through the gases to excited its energy level. The second step is called spontaneous emission; this process happens when the excited molecules released energy in the way of light, to decrease its energy level. An important consideration to take into account is to shift the excitation frequency respect to the emission frequency. Following this, superposed signals coming from other scattering process are avoided, the coincidence between the both of them is called resonance fluorescence.

Based on quantum mechanics theory, the energies that compose the internal energy are the electronic energy, vibrational energy, and rotational energy, see equation (20):

$$E_{total} = E_{elec} + E_{vib} + E_{rot} \qquad (20)$$

Figure 23 shows the energy exchange processes that involve laser-induced fluorescence. These exchanges occur between electronic, vibrational, and rotation levels of energy. These energy exchange processes are collisional quenching (Q_{21}), spontaneous absorption (B_{12}), stimulated emission (B_{21}) and spontaneous emission (A_{21}). A simple description of laser-induced fluorescence is the two-step process. At the first stage, an incident light helps the OH molecules to populate a higher energy level by absorption process. The frequency of the light has to be correctly chosen from the absorption spectrum in such a way that a successful transition is achieved. Subsequently, the instability of the higher energy level causes an energy release of the molecule by emitting a photon; this process is called emission or fluorescence. Many energy transfers might happen in the exited stated, at the rovibrational level.

Figure 23 -Diagram of energy level for OH radical
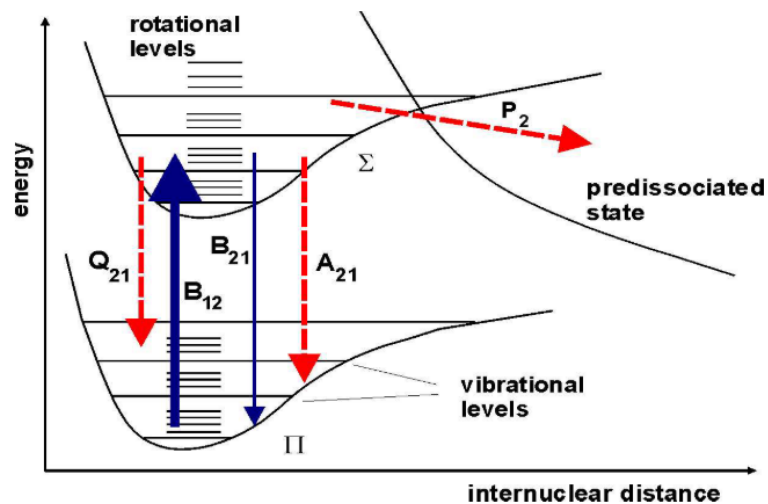
Pintgen (2005)

Since laser-induced fluorescence is a complicated process to describe, and the two-step process is a simple explanation for the whole process, a three-level model will be explained

according to Figure 24. This model was proposed by Mevel (2014) to model the PLIF process for nitric oxide. This model takes into account the following energy transfer process: stimulated absorption, stimulated emission, spontaneous emission, quenching, and rotational energy transfers. Each process is represented by arrows, according to the type of process, and letters : b_{12}, b_{21}, A_{21} and A_{23i}, Q and R. The following assumptions are taken to simplify the LIF process: (i) the energy transfers in the ground rotational state are fast, (ii) the rotational energy transfer in the excited stare are neglected, (iii) all the possible transition that happens between the excited state and the rovibrational ground state furnish fluorescence signal, (iv) the predissociation and photoionization processes are neglected (MÉVEL et al., 2014).

Figure 24 -Schematic of the three-energy-level model for laser-induced fluorescence
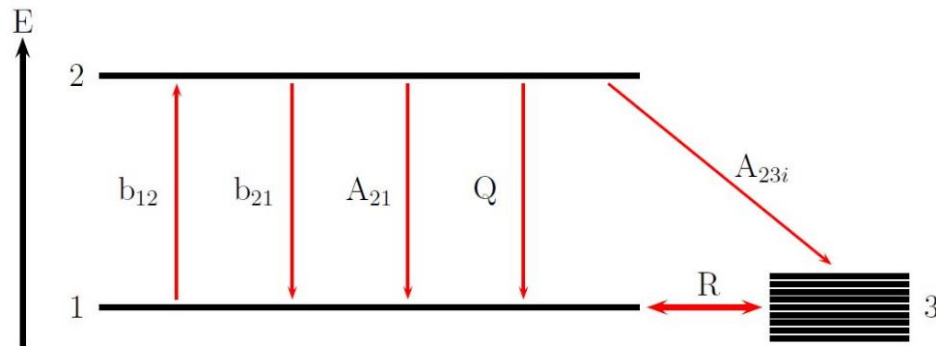
Mével et al. (2014)

The proportionality (21) gives the fluorescence intensity obtained from on single pumped transition:

$$F \propto f_B \Gamma I_v^0 I_b N_{OH} B \frac{1}{Q} \sum A_i \qquad (21)$$

f_B is the Boltzmann fraction of OH radical in the ground state, Γ is the dimensionless overlap integral, I_b is the dimensionless factor accounting for the light sheet absorption, I_v^0 is the

normalized spectral laser irradiance (J.s/m), N_{OH} is the OH radical density (1/m^3), B is the Einstein coefficient (m²/J.s), Q is the quenching rate (1/s) and A_i are the A Einstein coefficients (1/s).

The Boltzmann fraction can be calculated by using the equation 22, where Q_p is the partition function; this value can be taken from the HITRAN database (ROTHMAN; BARBE; BENNER, 2003).

$$f_B = \frac{g''\exp\left(-c_2\frac{E''}{T}\right)}{Q_p} \tag{22}$$

g'' represents the statistical weights of the lower state, E'' is the lower state energy(m^-1), c_2 is the second radiative constant (m .k), T is the temperature and Q_p is the partitions function.

The dimensionless overlap integral is calculated from the following equation:

$$\Gamma = \int_{-\infty}^{+\infty} Y_A L_L \, dv \tag{23}$$

The way to calculate the other variables is based on the model proposed by Mevel et al. (2014).

To adapt a Planar laser-induced fluorescence system, three subsystems have to be installed to obtain the proper laser sheet that will excite the OH molecules. They are the laser, optical system, and collection system.

To generate the emission of the OH radical, it is necessary to use a tunable laser; tunable is the property to vary the wavelength in a given range. Using this laser allows the user to perform the scan for the emission transition lines, by varying the wavelength. The OH emission spectrum is in the range of UV. To excite this transition, the laser has to be tuned until the proper line transition, according to the available database, the most populated and higher transition is close to 280 nm. Indeed, one of the most used transition to studying OH is the $Q_1(6)=282,99$ nm (GORDON; MASRI; MASTORAKOS, 2008).

Dye lasers are an excellent option to work with PLIF. For this type of laser, the gain medium is a liquid organic dye dissolved in liquid solvents. With broadband between 300–1100nm output, dye lasers were workhorses in scientific laboratories for many years (ABRAMCZYK, 2005). A particular characteristic of dyes is the broad absorption band, resulting in the generation of many longitudinal modes in an optical resonator that can be favored by tuning continuously across a range of wavelengths. Figure 25 shows the energy transitions that occur in a Dye laser. The transition happens at four-level, the transition occurs at the electronic level, but they are strongly affected by the molecular vibration. The light coming from the pump (1) transfers the dye from the ground-vibrational level of the lower electronic state S_0 to a higher vibrational level in the electronic state. In the vibrational state occur a relaxation in a radiationless way to a lower level. Finally, the emission (laser action) (3) occurs between the upper electronic state and the lower electronic state, following by a quick depopulation by radiationless relaxation to the ground vibrational level of the lower electronic state (4) (ABRAMCZYK, 2005).

Figure 25 -Scheme of energy transitions in a dye laser
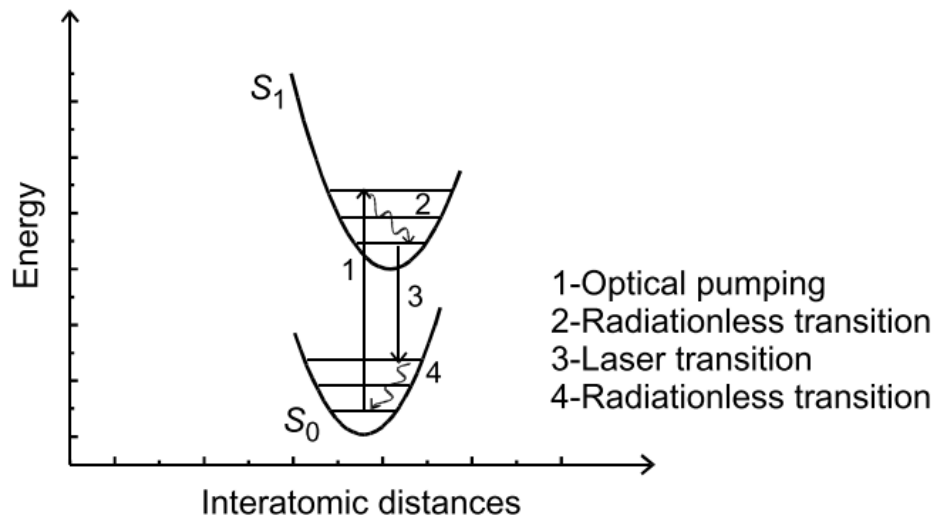
Abramczyk (2005)

The shape of the beam provided by the Dye laser is often circular. However, the area to be excited is not a single point but is planar, so an optical system has been installed to spread the

circular laser output to a thin sheet. This can be done by using an arrangement of lenses according to the desired dimensions of the test rig. Only the necessary lenses have to be chosen to perform the spreading process since each optical device produces losses. Firstly, the beam needs to go through a cylindrical lens to stretch the beam in the vertical direction; this type of lenses can spread only in one direction, so the proper vertical spreading angle has to choose in the installation. Secondly, the spread beam needs to be collimated to project a parallel beam into the test region; a spherical lens realizes this work.

A conditioner factor to choose the lenses is the height (L) of the laser sheet. This parameter is based on the resolution of the PLIF image and area to be excited. Using a spherical lens bigger than the calculated height is always an excellent way to avoid spherical aberration since this aberration is boosted on the edges. By using a negative cylindrical lens, the distance between the lenses can be reduced. Figure 26 shows how the circular shape of the laser is transformed into a thin sheet by using a negative cylindrical lens and a spherical lens. Equation 24 expresses how to calculate the height based on the focal length of the lenses.

$$L = 2\frac{r_0(f_2)}{f_1}$$

(24)

Figure 26 -Optical arrangement for PLIF
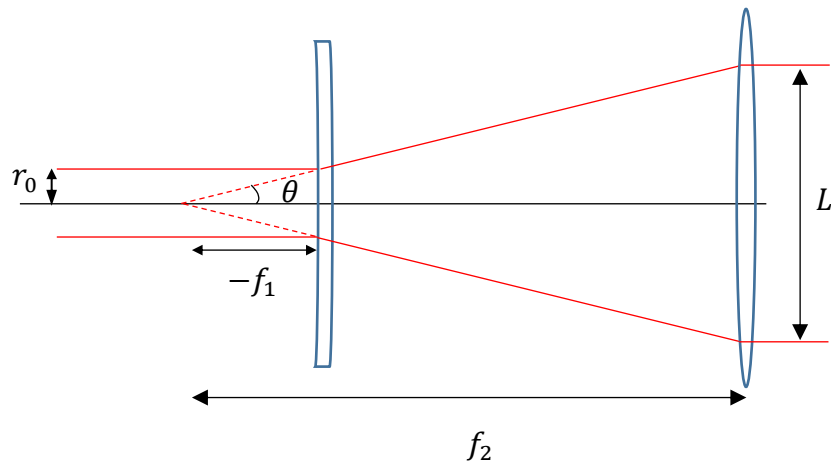
Own authorship

There are other considerations to take into account to install the optical system. The lenses to be used in PLIF need a special coated to work at the UV spectrum. Otherwise, the light will not be transmitted through the optics, or the losses due to reflection or absorption would increase. Since the intrinsic laser profile is Gaussian, the laser sheet will be characterized by the high intensity in the middle and low intensity on both sides. This configuration affects the quality of the images, creating a blurry picture because a thicker volume is excited. For this reason, a knife has to be used to block sharply the low-intensity region, also called wings. Also, the focal length of the spherical lens is another crucial parameter for experimental setups that consist of a long path to reach the test region. The correct distance to avoid the variation of the laser sheet thickness is to keep constant the same focal length (f_2) from the position of the spherical lens to the test region.

Since detonation occurs in short periods, a proper camera to study this specific phenomenon has to be chosen. ICCD cameras are a short-gateable system with a minimum gate width in the order of 30 ns (PRINCETON INTRUMENTS, 2003). This short gate allows capturing images with high resolutions, avoiding blurriness due to the fast propagation of detonation. Moreover, this type of camera can detect UV light by using its intensifier mode. Figure 27 shows the part of the intensifier and CCD chip. To collect the specific wavelength, an arrangement of lenses has to be installed in front of the camera to avoid the light coming combustion and chemiluminescence that boost the noise (PRINCETON INTRUMENTS, 2003).

Figure 27 -Structure of an ICCD camera


Princeton intruments (2003)
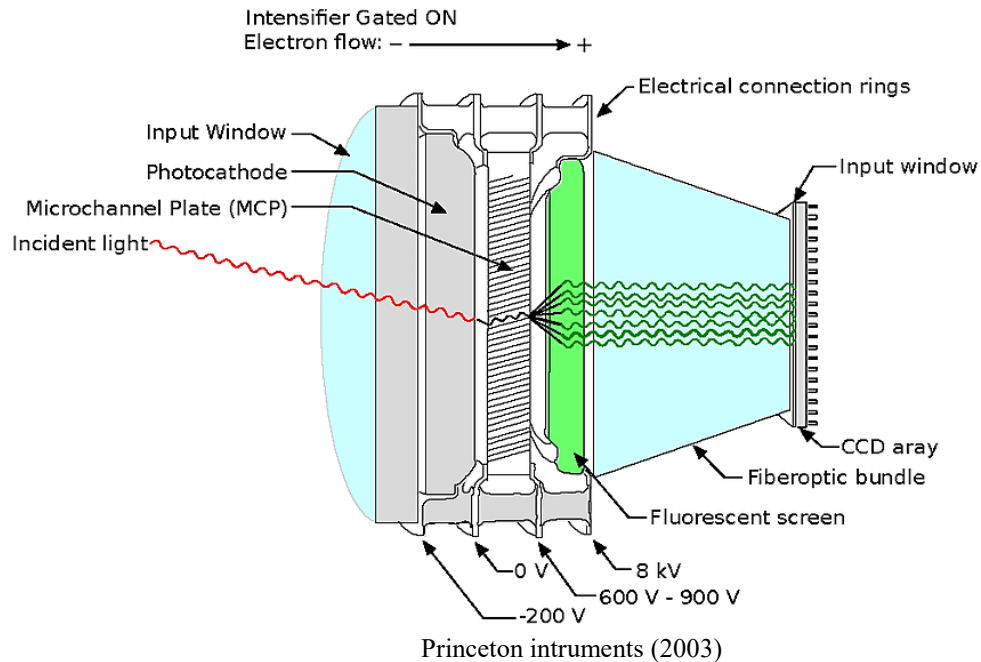
3 EXPERIMENTAL SETUP

The third chapter discusses optical diagnostics techniques to image the detonations, as well as the details of the detonations setup. Firstly, a brief introduction to the detonation test rig will show the principal dimensions and the necessary sensors to measure pressure and velocity. All the experimental procedures will be discussed to perform a detonation shot. Moreover, three strategies are proposed to obtain a reproducible detonation. Secondly, the experimental setup to image the density gradient will be showed, discussing in detail the synchronization to obtain a proper image. Thirdly, the optical technique PLIF will be installed to the detonation setup to image the fluorescence released by the OH radical, two setups are proposed, one to perform the wavelength scan and the other to realize the real detonation PLIF image. The last section presents the mixtures used for every experimental measurement.

3.1. DETONATION SETUP

The detonation setup consists of six rectangular sections, and each section is 470 mm length. Every piece in the detonation setup was made of stainless steel. The square cross-section wherein the detonation will propagate is 170 x 20 mm, see figure 28. Flanges connect the sections and are sealed with a synthetic resistant rubber gasket (ethylene propylene diene monomer rubber) that can support at most 69 bar of pressure and meet the specification of ASTM D2000. Figure 29 shows the schematic of the detonation setup. The overall length is 300 cm. The setup is closed both sides to achieve lower pressure than the atmospheric for the initial conditions. At the beginning of the setup is located a flange that contains three spark plugs (Super 305-Bosch) to ignite the mixture, as well as contain a tube for the recirculation line. The spark plugs are connected to an ignition system that supplies the high voltages to create the spark. Since the amount of energy applied by the spark plugs is not enough to generate a detonation event, obstacles have to be installed to transit flame from deflagration to detonation. In the first and second sections, there are six obstacles with a separation distance of 100 mm; these obstacles are used to enhance the transition to detonation by activating the turbulence loop described in Figure 15.

53

Figure 28 -The inner dimensions of the detonation test rig
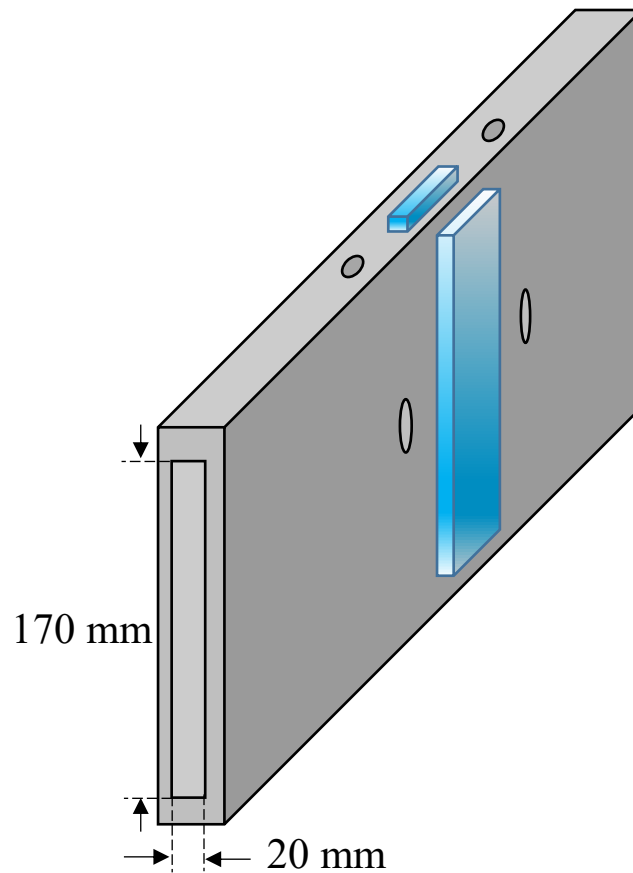
Courtesy of Professor Deanna Lacoste, KAUST faculty (2019)

The third, fourth, and fifth section contains the pressure transducers and ionic probes to measure the velocity and local pressure. The separation distance between the sensors is 20 cm. The ionic probes are low impedance spark plugs (NGK-6263), that can measure the intensity of ions contained by flame. The ionic probes are connected to a conditioner box that amplifies the voltage signal. The pressure sensors, unlike the ionic probes, are only located in the fourth and fifth sections, recording signals from the P3, P4, P5, and P6 sensors, P1 and P2 are only spots wherein will be installed new pressure sensor in future studies. This arrangement of the sensor was only used for velocity and Schlieren measurements. These quartz pressure sensors are specially designed for detonation waves and shock tubes and for applications that require very high frequency. The essential features of the sensor are the sensitivity of 10 mv/psi, the resolution 2 mpsi, and the uncertainties are in the order of ± 1 %. All pressure sensors are connected to the four-channel

signal conditioner from PCB piezotronics, and the range of frequency is 0.05 Hz to 17 kHz. Once the acquisition system records the voltage signal from both sensors, the following step is to post-process the data to determine the velocity. The propagation velocity of the wave is calculated based on the distance between two sensors (20 cm) divided by the time that the wave spends traveling from one sensor to the next sensor. Therefore, the estimated velocity is the average velocity between two sensors. Both ionic probes and pressure sensors are used to determine the velocity. The pressure and velocity measurements are crucial to confirm if the propagation is in the detonation regimen, by comparing the experimental measurement with the Chapman-Jouguet state for pressure and velocity.

Figure 29 - Schematic representation of the experimental detonation setup
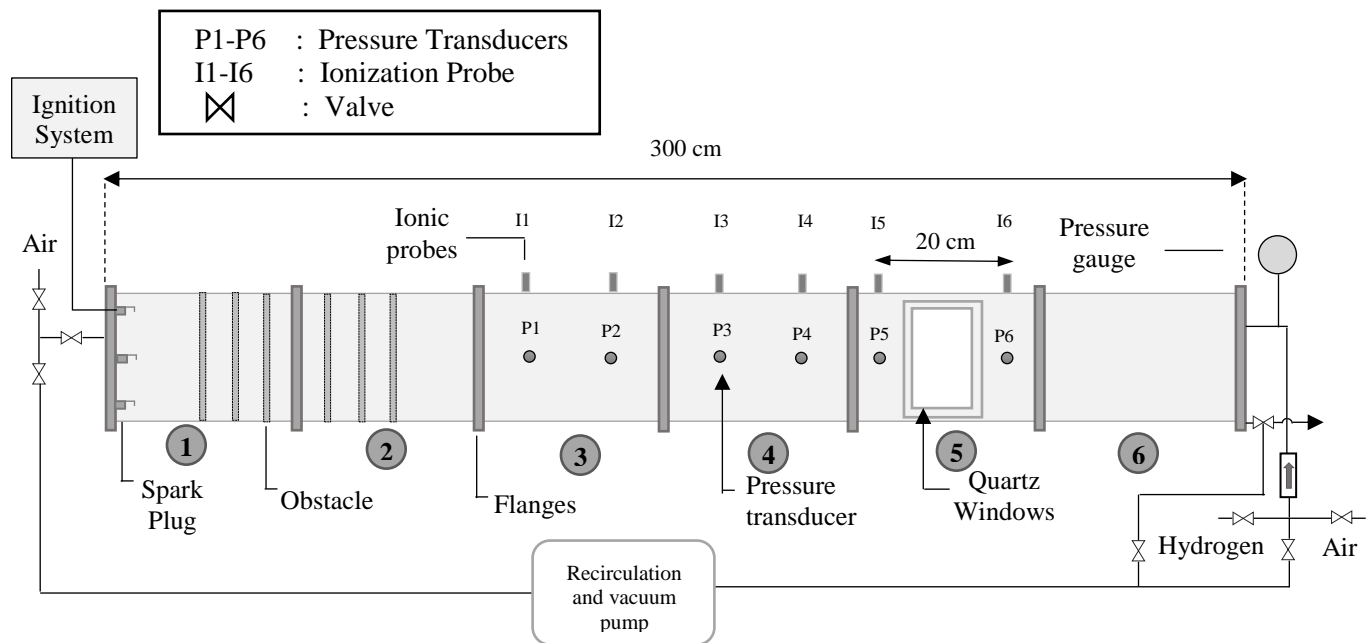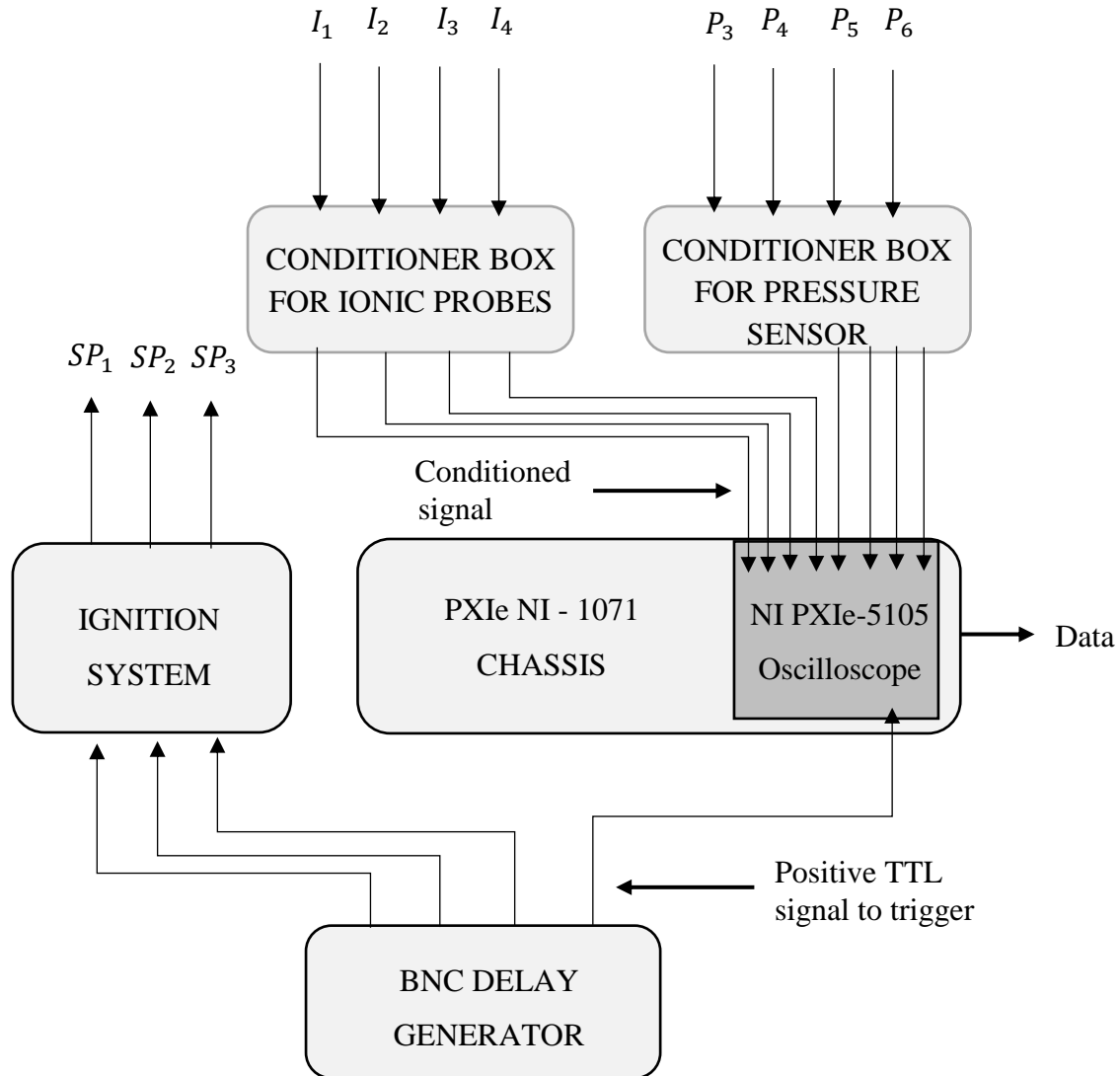

Own authorship

The conditioned signals converted in both conditioner boxes are connected to an oscilloscope module that only contains eight channels; for this reason, only four pressure sensors and four ionic probes are used on the measurements. The oscilloscope module (NI-PXIe-5105) has a maximum bandwidth of 60 MHz and is embedded in a PXIe NI–1071 chassis with a bandwidth of 3Gb/s;

both devices conform the acquisition system, after this stage, the signal becomes digital information. Figure 30 represents the schematic of the connection between the acquisition, ignition, and delay signal system. The delay generator triggers both the ignition and acquisition system, applying a positive TTL signal ($\sim$4 $volts$). The trigger signal is a single shot that allows to ignite the mixture using spark plugs and to record the signal from the sensor and ionic probes.

Figure 30 -Schematic of the acquisition, ignition, and delay signal system

Own authorship

As can be seen in Figure 31, once the delay generator's run bottom is pressed at T_0, all spark plugs are simultaneously activated during 5 ms to ignite the mixture. After the spark plugs are

activated, the acquisition system waits 10 ms to start recording the signals. The pulse applied width is 6ms, as suggested by the manufacturer. However, this pulse width is only the necessary time to trigger the acquisition, since the total recording time is 30 ms. The delay time of 10 ms was chosen in order to record the detonation phenomenon efficiently and avoid overweighted data files.

Figure 31 -Timing diagram for ignition and acquisition system
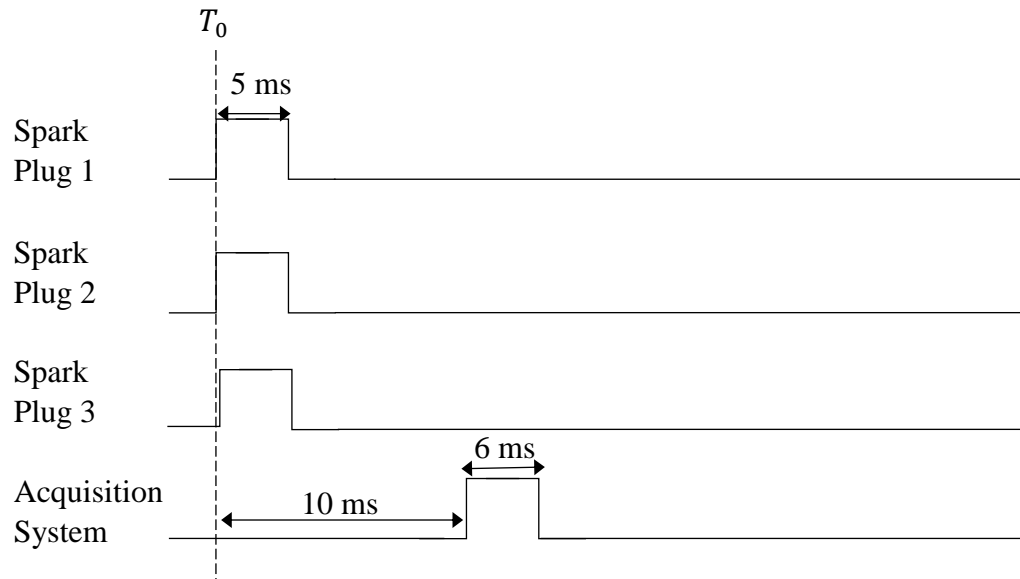
Own authorship

Moreover, the fifth section contains the optical access of 150 x 80 mm, to image the detonation wave by using both techniques Schlieren and PLIF. The windows are made of the Quartz to support the high pressures loads and transmit the UV light emitted by the fluorescence of the OH radical. Stainless steel holder crumples both windows; between the windows and holder, a rubber gasket was installed to avoid cracks in the window. The last flange of the sixth section contains two access for recirculation tubes and a small quartz window, whereby the laser sheet of the PLIF configuration will enter to the setup.

Surrounding the detonation setup is the tubing system. At the beginning of the setup three valves are connected by a T junction; both of them are for the recirculation and vacuum process, and one is to flush air inside the chamber. At the end of the setup, the tubing system contains the

valves for hydrogen and air. These valves are used to supply the amount of reactants into the setup. In the case of inadvertent fire that could damage the cylinder, a flame arrestor is located upstream to quench the propagation; this device also works as a check valve allowing to flow only in one direction. In the upper right side of the tubing system is the pressure gauge (LEO 3 – Keller). The purpose of the pressure gauge is to read the pressure that represents the amount of air or fuel added to the system, by partial pressure law. The pressure range of the gauge is from -1 to 3 bar, and its total error band is $\pm$ 0.1% FS. Furthermore, the left and right tubing systems are connected by a pump that performs the recirculation of the mixture and vacuums the remaining water molecules.

The procedures to obtain an experimental run consists of six steps. Initially, the chamber is flushed using air for 10 minutes to make sure that any water particle remaining inside is expelled to the extraction hood. Once the chamber is clean, it is necessary to vacuum the setup up to 5 mbar; however, depending on the leaks generated by the previous run, we can reach fewer pressures. The next step is the filling procedure; according to the initial pressure and the equivalence ratio, the setup is filled with fuel and air by modulating both valves and reading the pressure gauge, this process relies on the partial pressure law. As detonation works with premixture, it is essential to ignite a homogeneous mixture, so the whole volume is recirculated with the pump through the circulation line, for three minutes. After the recirculation process, the mixture should rest during one minute to avoid any influence of the movement generated by the previous step. Once the time is over, the ignition and acquisition system has to be activated, as Figure 32 shown.

In order to obtain reproducible detonation in the setup, three strategies were proposed. These strategies are related to the change of the obstacle geometry, and the amount of the spark plug used to ignite the mixture. The first strategy, shown in Figure 32, proposes to use a square obstacle (obstacle 1) and one spark plug. The obstacles are located in the top and bottom walls of the first and second sections, as shown in Figure 29. The overall number of obstacles is twelve since six pairs of the obstacles are installed next to each other, with a separation distance of 100mm. The blockage ratio of a pair of obstacles is 0.47. The second strategy, keep the same number of spark plugs, but a new geometry of obstacle (obstacle 2) is installed to enhance the turbulence in two directions, see Figure 33. Six obstacles two are installed across the section. The blockage ratio for this geometry does not vary much compared to obstacle one, the value is 0.426. So the blockage ratio can be considered as constant.

Figure 32 - Arrangement of first strategy: (a) Obstacle 1 (BR=0.47) + (b) One spark plug

(a)   (b)
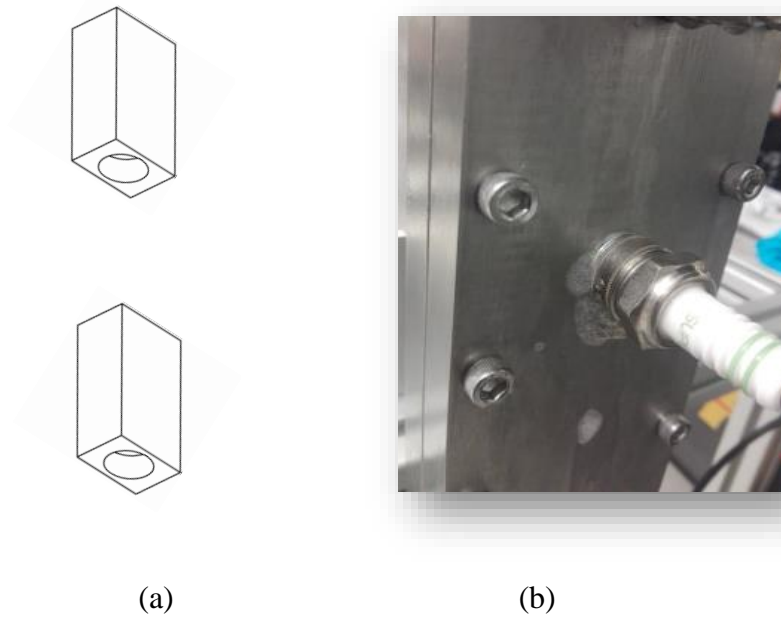
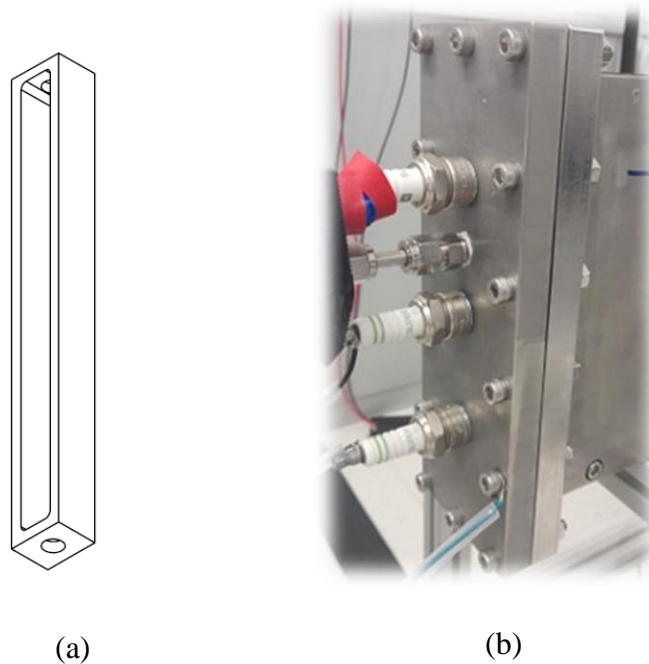Source: Own authorship

Figure 33 -Arrangement of second strategy: (a) Obstacle 2 (BR=0.426) + (b) One spark plug

(a)   (b)
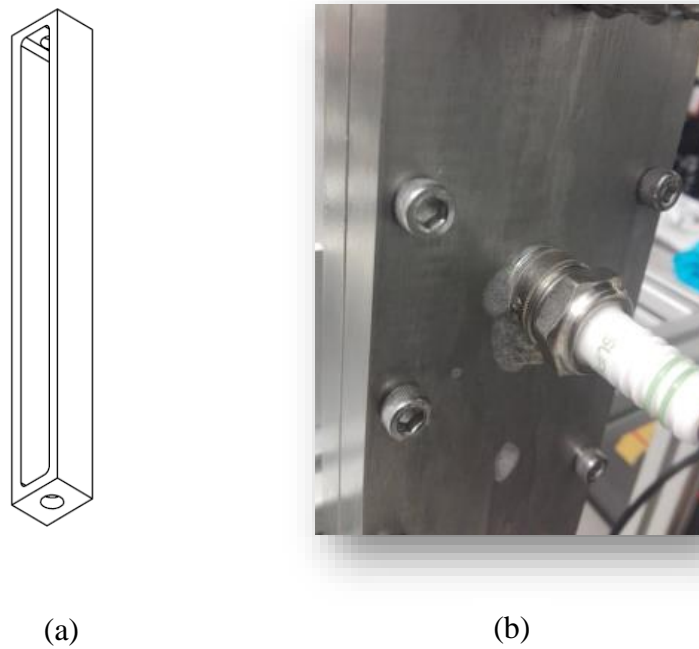
Own authorship

Finally, the third strategy combines obstacle two and three spark plugs, see Figure 34. For each strategy, the position of the obstacle, the number of obstacles, and the pulse width applied to the spark plug were kept constant. All these strategies were carried on to choose the best arrangement that produces successful transitions from deflagration to detonation. Once repeatable detonation events occur, the Schlieren setup has to be installed to image the density gradient of the detonation wave.

Figure 34 -Arrangement of third strategy: (a) Obstacle 2 (BR=0.426) + (b) Three spark plugs

(a)   (b)

Own authorship

3.2. SCHLIEREN SETUP

A Z-type Schlieren setup was installed to images the density gradient of detonation waves. The Schlieren and detonation configuration are depicted in Figure 35, detailing every part of the system. This configuration consists of one light source, two concave mirrors, one edge knife, two plane mirrors, one bandpass filter, and a camera.

The light source for the Schlieren setup is a Blue LED of 445 nm wavelength; the spectrum of the light is shown in Figure 36. Some preliminaries tests were performed to avoid any influences from the light emitted by the detonation on the Schlieren quality. The tests consisted of measuring the intensity of the light emitted by the detonation by placing a bandpass filter in front of the camera. The variation on the intensity was minimum when using a bandpass filter of 450 nm, meaning that the detonation wave does not emit light on that range. These tests allowed us to select both the light source and the bandpass filter properly. Since LEDs are intrinsically a diverging light source, an iris is located in front of it to become a point light source.

Figure 35 -Schlieren setup adapted to the detonation test bench
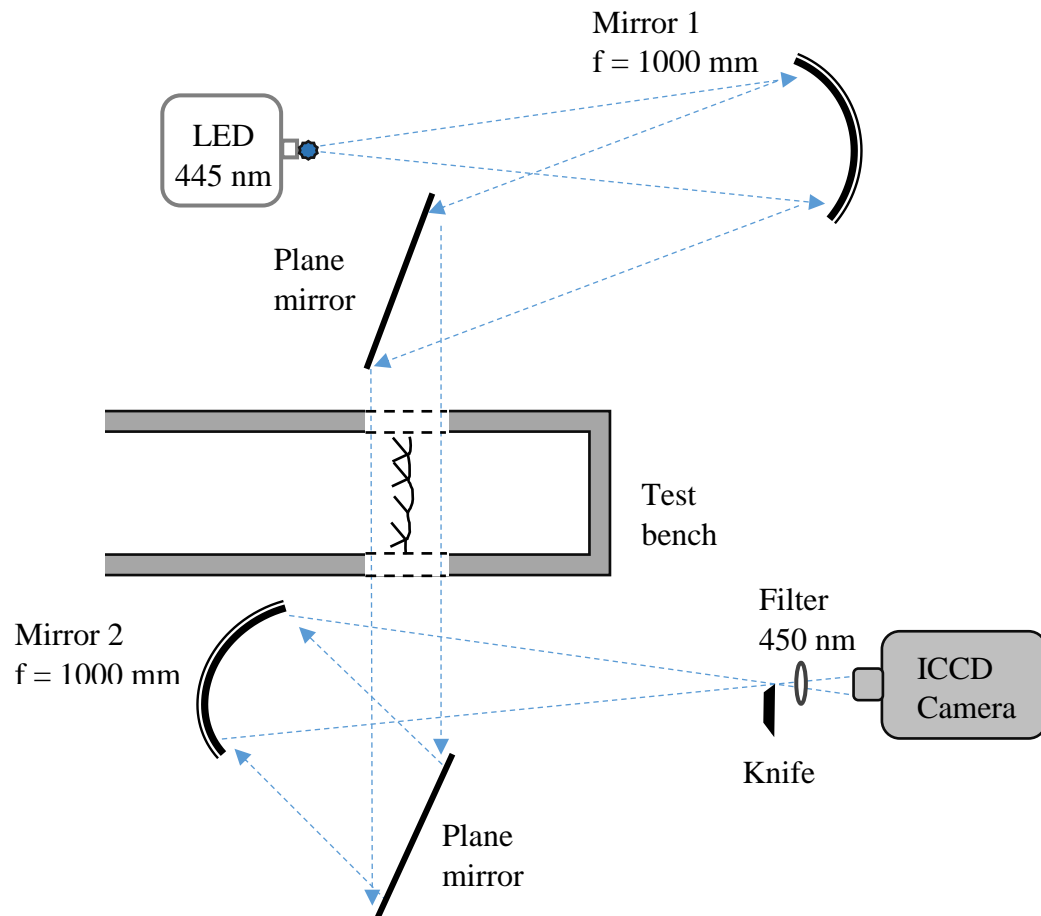
Own authorship

Figure 36 - The spectrum of LED-light source
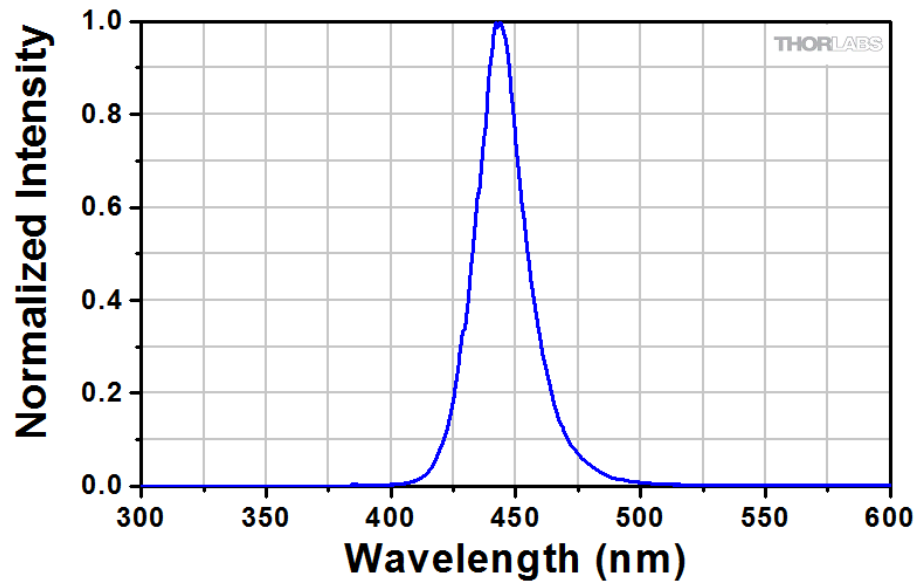
In order to send parallel beams through the detonation wave, a collimation process was carried out. The process starts by collecting the diverging light by using a concave mirror of 1000 mm focal point. So the light source is located at that distance to create a collimated light. However, a collimation crosscheck process was necessary to make sure the light is collimated, for this process was necessary two business cards with a hole in it, the holes have to be the same diameter. First, one business card is located in front of the collimated light, and the other card is located downstream. If the diameter of the light projected on the second card is expanded or reduced, the light is not well collimated, and the distance between the concave mirror and light source has to be readjusted until finding no changes in the diameter. The collimated light provided by LED is continuous; therefore, the amount of light going to the camera will be controlled by exposure time.

The collimated light coming from the concave mirror is reflected using a plane mirror of $\lambda/10$ flatness, then the light goes through the optical access of the detonations setup, where it will be deflected by density gradient created in the wavefront and reaction zone. The total size of the available optical access 150 x 80 mm; however, the real size of the lighted media is less because of the size of the mirrors, see Figure 37. Subsequently, the light is reflected in another plane mirror towards a concave that will converge all the incoming light into a point.

Figure 37 -Optical access dimensions and trajectory of the light source
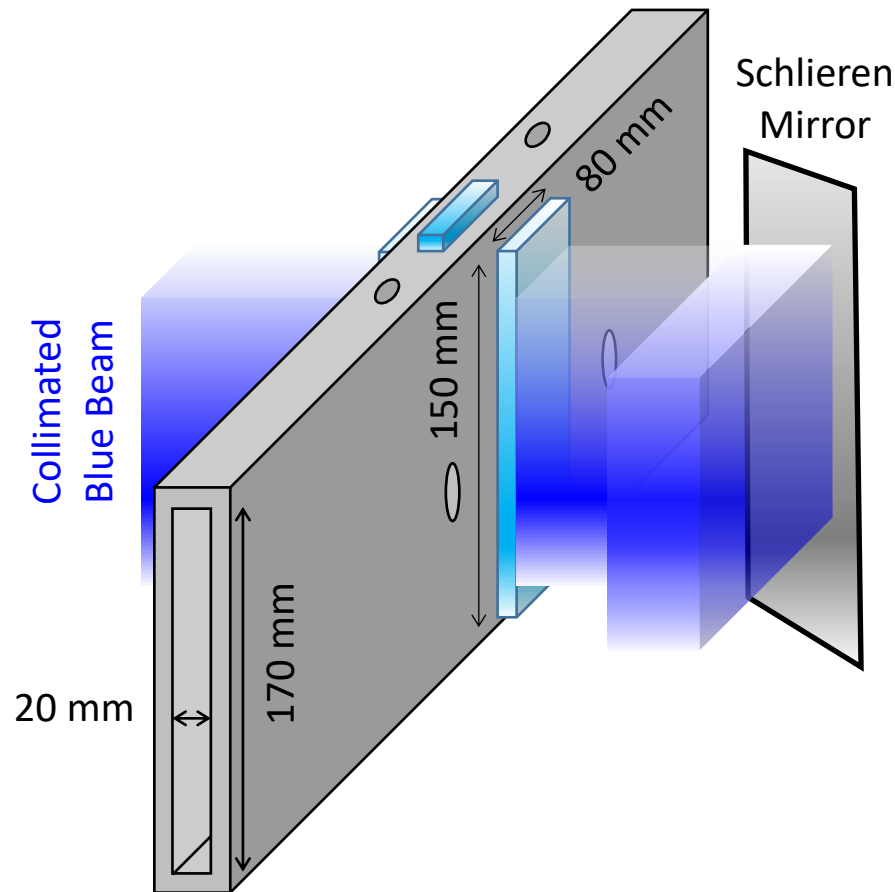
Courtesy of Professor Deanna Lacoste, KAUST faculty (2019)

Once the beams are converged into a point, the cutting process takes place. Exactly where light is a point, a knife-edge is located to cut deflected light. The knife-edge is a razor blade that cuts the vertical coordinates since the horizontal gradients are stronger because of the propagation direction. To recognize if the cutting process was well performed, the intensity of the light has to be checked on the camera. If the intensity of the light is higher in some regions than others, it means that the knife-edge is not correctly located in the focal point. So the correct position had to be found until the intensity on the image is uniform.

The chosen camera to image the detonation density gradient was an ICCD and a CMOS camera. The first images taken were done by using the CMOS camera since the repetition rate was higher than other cameras allowing to capture more than one picture of the detonation. Nonetheless,

as the repetition rate is increased, the image resolution is affected. Furthermore, because of the high exposure time of this camera and the high velocity of the phenomenon, the obtained pictures were blurry. To make sure that the blurriness is not affecting the quality of the pictures, an ICCD camera was chosen to replace the CMOS camera. This camera can work under low exposure time in the order of 25 ns. However, only a single picture can be taken because of the low repetition rate (10Hz). Two Nikon lenses were used to collect the beam into the ICCD chip, 60 mm and 105 mm. Before the camera lens, the bandpass filter was placed to allow only the light emitted from the light source and reject the light emitted by the detonation.

The synchronization to capture the Schlieren images are depicted in Figure 38 and Figure 39. As the diagram shows, the ignition and acquisition system works like Figure 30. Since the detonation phenomenon is the fastest mode of propagation, the correct timing to trigger the camera becomes complex. In order to avoid any influence of the unsteady behavior of the detonation in the first sections, the fifth pressure transducer was selected to trigger the camera. By choosing this sensor, the margin of error decreased since the distance to the optical access is shorter than other sensors. Before to use this sensor as the trigger, various preliminary tests were carried out to determine the average amplitude voltage. For the initial conditions when detonation occurs, the amplitude exceed

Figure 38 -Timing diagram for ignition, acquisition and Schlieren system
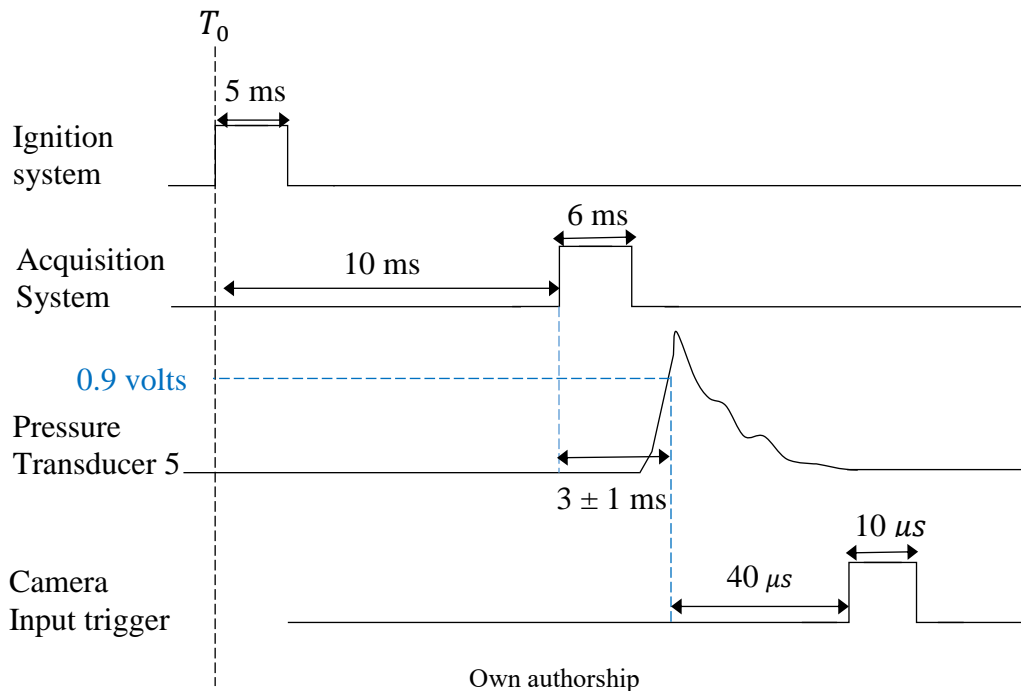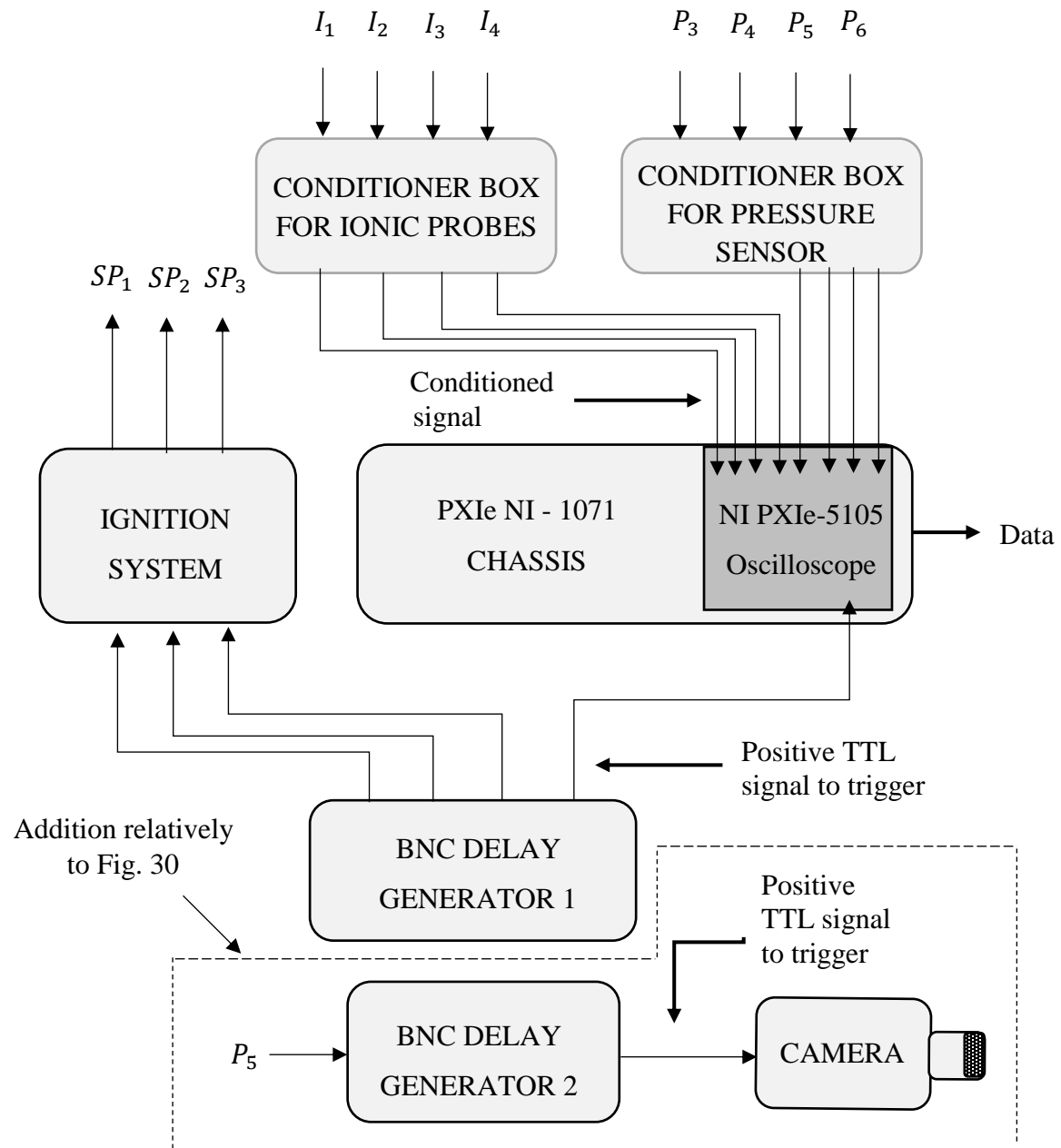

Own authorship

Figure 39 -Schematic of the acquisition, ignition, delay signal, and Schlieren system

Own authorship

one volt for every run. For this reason, the 0.9 volts was chosen as the threshold signal that the delay generator needs to trigger the camera. If higher values were chosen, the amplitude of the signal might not trigger the camera. If lower values were chosen, the camera might be triggered by

the noise or peaks of interference created by the ignition system; as a result, the camera would take an image before the detonation reaches the optical access. To determine the proper delay from the pressure transducer five to time when the detonation wave is the middle of the optical access, more preliminary tests were taken. The tests consisted of increasing the delay time for each run until finding the right conditions. The delay that image properly the density gradient of the detonation wave is forty microseconds. The pulse width to trigger the camera was ten microseconds. And the exposure time to capture the detonation was varied for some runs. Figure 40 shows the schematic for the additional connection to adapt the Schlieren system. As can be seen, to trigger the camera, another delay generator was needed to detect the threshold signal (0.9 volts) generated by the pressure sensor five. The sensor was connected to a BNC "T" junction to send two signals, one to the acquisition system and the other to the second delay generator. Then, the delay generator sends a single shot TTL positive signal to the camera, capturing the detonation wave at the proper time.

3.3. PLANAR LASER-INDUCED FLUORESCENCE SETUP

In order to image the detonation reaction zone, the optical technique called Planar laser-induced fluorescence was applied. As mentioned in Chapter 2.6, by using this technique, OH radicals can be exited emitting a fluorescence signal. Figure 40 shows the schematic of the PLIF system adapted to the detonation setup, Figure 41 represents the parallel PLIF system to perform the wavelength scan, and Figure 42 represents the connection made between the lab equipment. The PLIF setup consists of a laser, three plane mirrors, one iris, one cylindrical lens, one spherical lens, one power meter, and an ICCD camera. The laser was a Continuum (ND6000) dye laser, and the dye is a Rhodamine 590 diluted with methanol. This laser is also tunable, meaning that the wavelength can be varied. This characteristic is important to realize the wavelength scan and recognize the emission lines of the spectrum. The light emitted by the laser has to be reflected by plane mirrors until the beam reaches the PLIF lens arrangement. The mirror has a special coated that allows high reflectivity at 283 nm (UV), which is the approximate wavelength to perform the scan. At a certain stage in the laser, the original light pumped by the flash lamp and dye is visible (~566 nm), this light goes through a double frequency crystal that becomes the beam into UV light. Since the laser emits two-wavelength at different angles, a separation process had to be done using
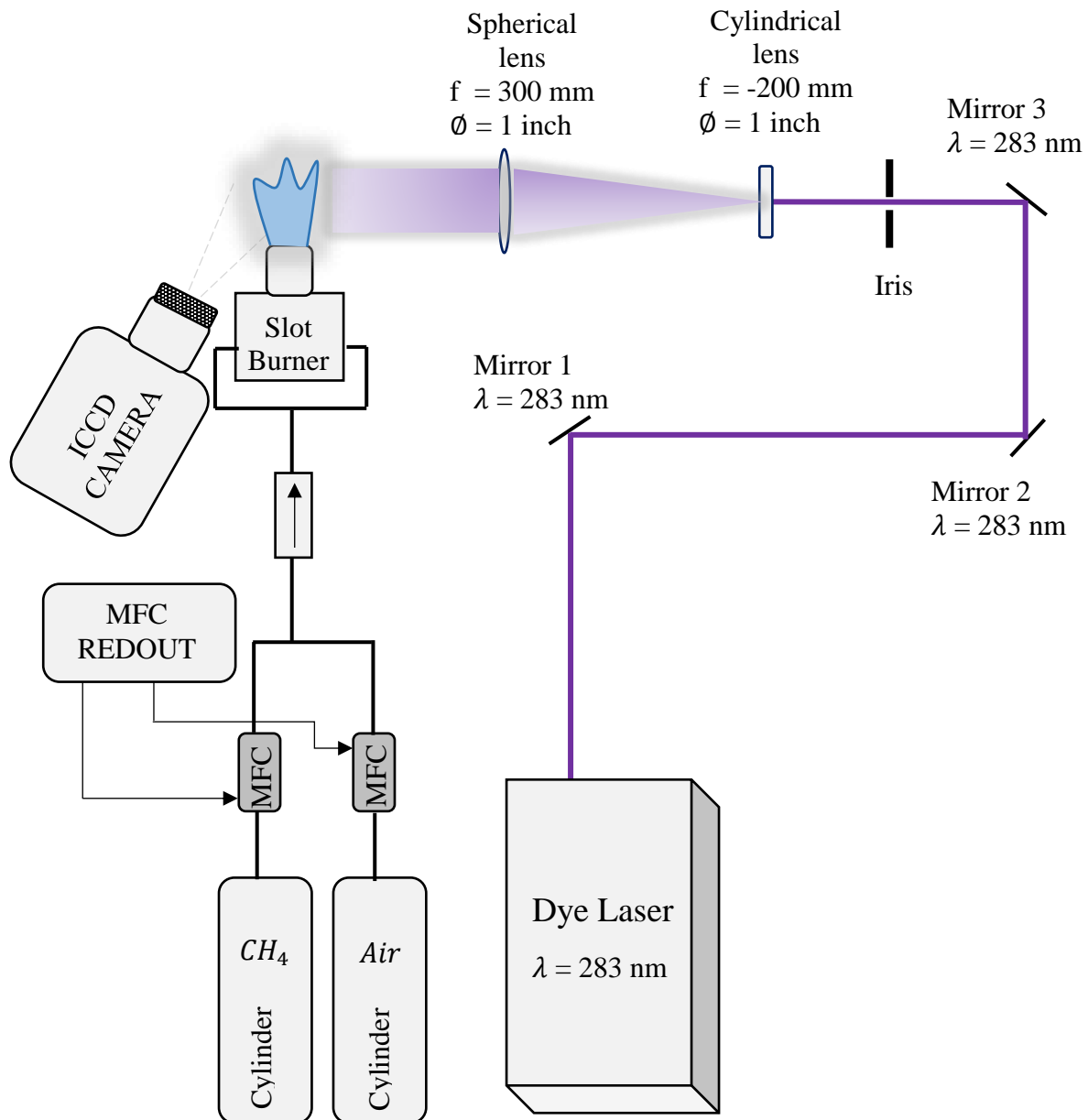
the mirror 1. The process consists of reflecting the UV beam by the mirror one and transmitting the visible beam through the mirror until it reaches a safe dump.

Figure 40 -PLIF setup adapted to the detonation test bench
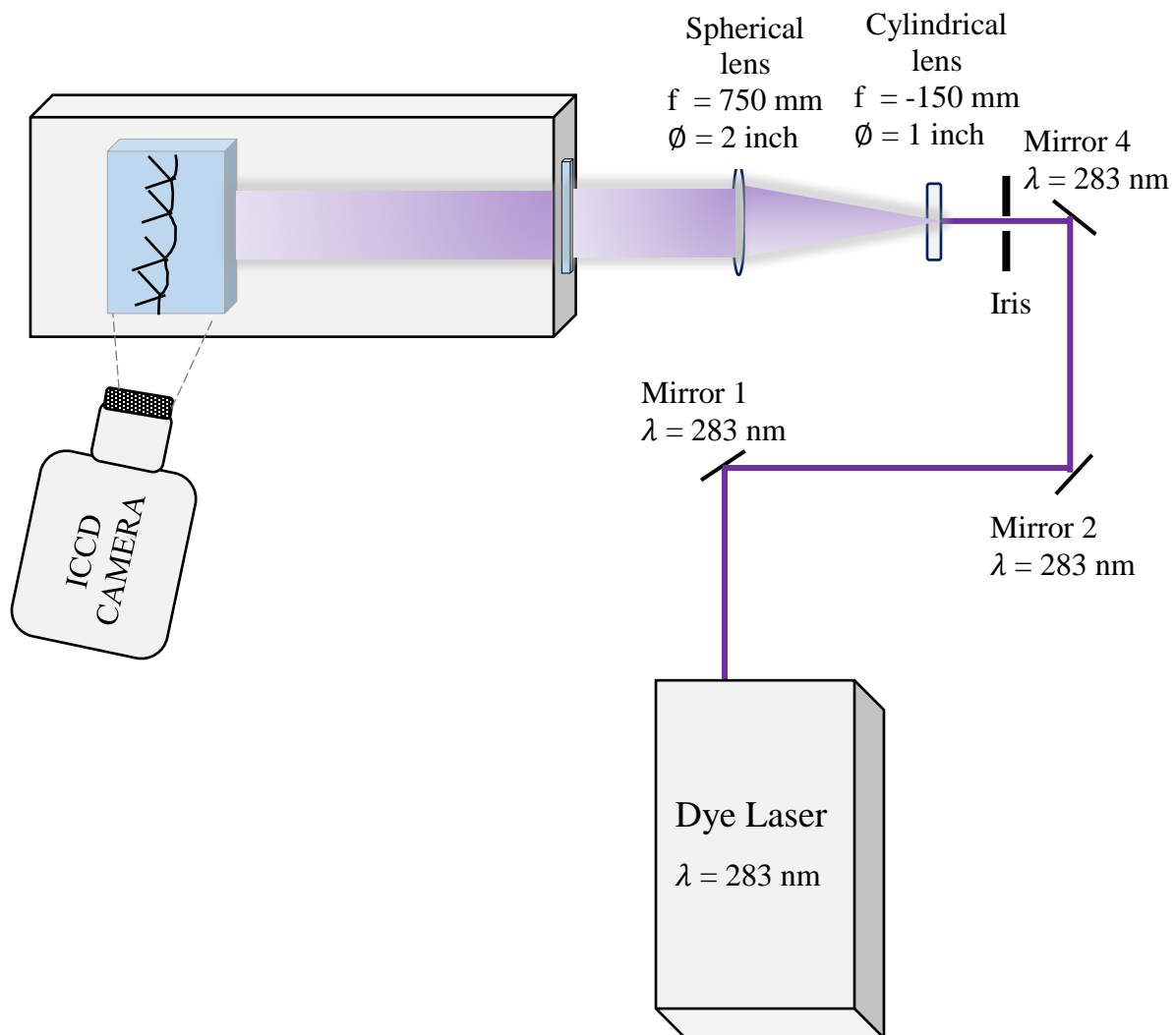
Own authorship

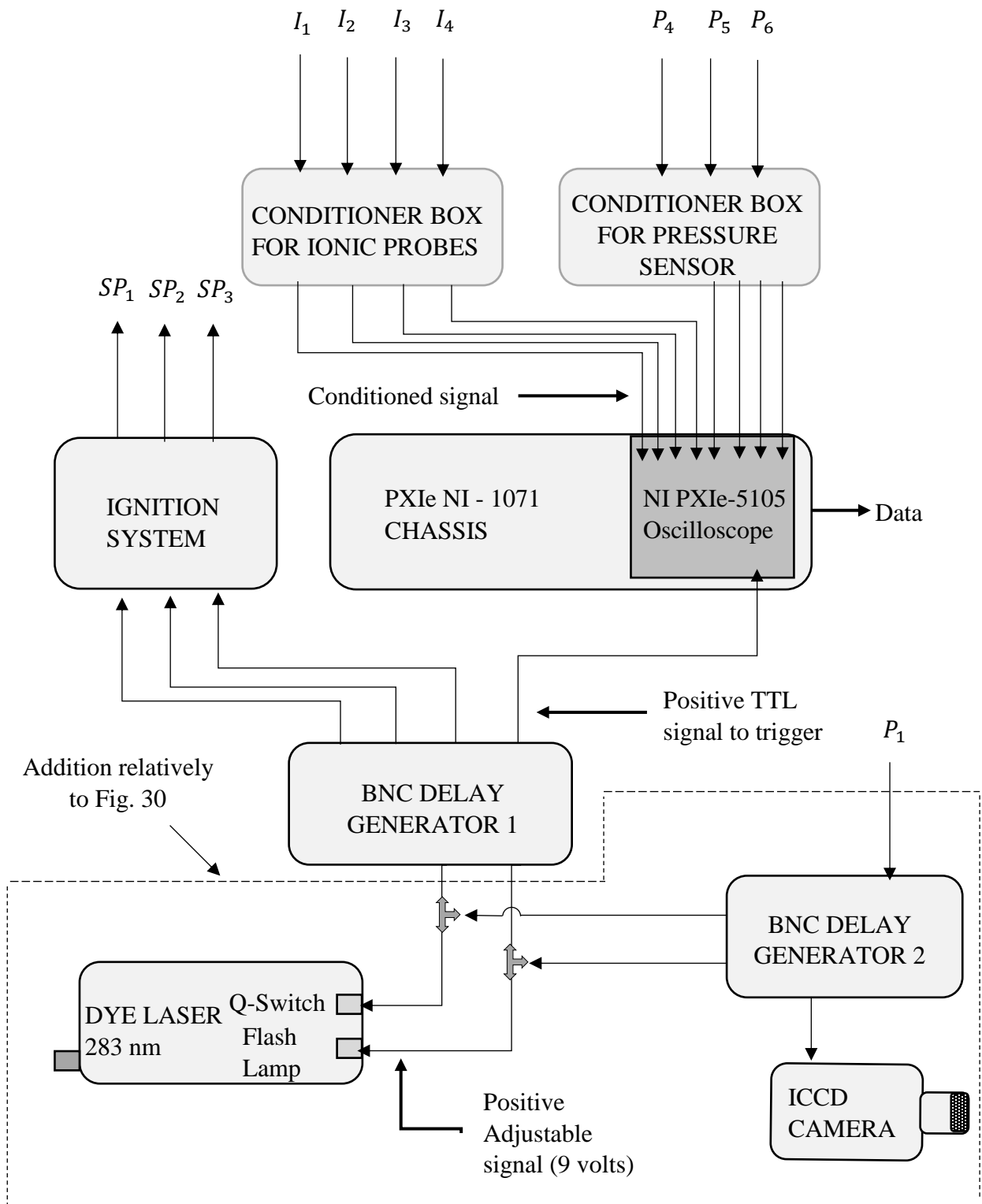Figure 41 -PLIF setup adapted to a slot burner for wavelength scan

Own authorship

Before the laser beam goes through the lenses, the distorted circular profile of the laser had to be corrected by an iris. This optomechanical device cut the outer distortion created by reflection in many mirrors. Once the beam is corrected, the light has to pass through a cylindrical lens. The negative focal length (-150 mm) was strategically selected to avoid long distance between spherical and cylindrical lenses. Cylindrical lenses can expand the laser in only one direction, so a grade

caliber needs to hold the lens to make sure expansion occurs in the vertical coordinate. The next stage is to become thinner and parallel the beam by using a spherical lens. The height of the laser sheet is constant until 750 mm, then the beam expands. So the reason why the focal length is 750 mm, is because of the long distance between the center of the optical access and spherical lens. The distance between them is 780 mm; however, for long focal length, the expansion of the beam is not dramatic compared with short focal length. To capture the fluorescence emitted by OH radical, an ICCD (PI-max 3) camera was used. As can be seen in Figure 35, a plane mirror is in front of the camera to reflect the light collimated light; for this reason, the camera was tilted forty-five degrees respect the normal, on the left side of the plane mirror. Furthermore, this modification will be useful for future experiments when the Schlieren and PLIF technique will be used simultaneously. For the present study, each technique was performed independently.

The selection of the emission lines had to be made by scanning the intensity of the fluorescence emitted by a methane-air flame. Since detonation experiments spend fifteen minutes on setting up all the necessary requirements and procedures for a single shot, an additional setup was installed to supply a constant flame. This setup was located next to the detonation setup, in such a way that by removing mirror three, the laser beam passes to the PLIF-detonation arrangement, the complete arrangement is shown in Appendix F. The dye laser, mirror 1, mirror 2, and the ICCD camera that appear in Figure 40 are the same devices for Figure 41. The expansion of the process is similar to the one explained for the PLIF-detonation setup. However, the characteristics of the lenses are different. The focal length of the cylindrical lens is -200mm, and the spherical lens is 300mm. These dimensions provide a laser sheet with a different height compared to Figure 40. Even though the height is different, the scan process is still effective in detecting the offset.

The system to generate the laminar flame consist of a slot burner, one MCF readout, two MFCs, and two-cylinder of methane and air. The composition of the mixture methane-air was stoichiometric at atmospheric pressure and 293 K. The flow rate of the mixture is controlled individually by two mass flow controllers (MFC) from MKS. Both mass controllers are connected to the cylinders, that supplies the fuel and air, and to the MFC readout (MKS-type 247) that module the flow rate transferred to the burner. To avoid flashback events and damages on the MFCs, a flame arrestor was installed upstream of the controllers. The flow rate of methane and air was 0.76 and 7.24 litter per minute during the scan, respectively.

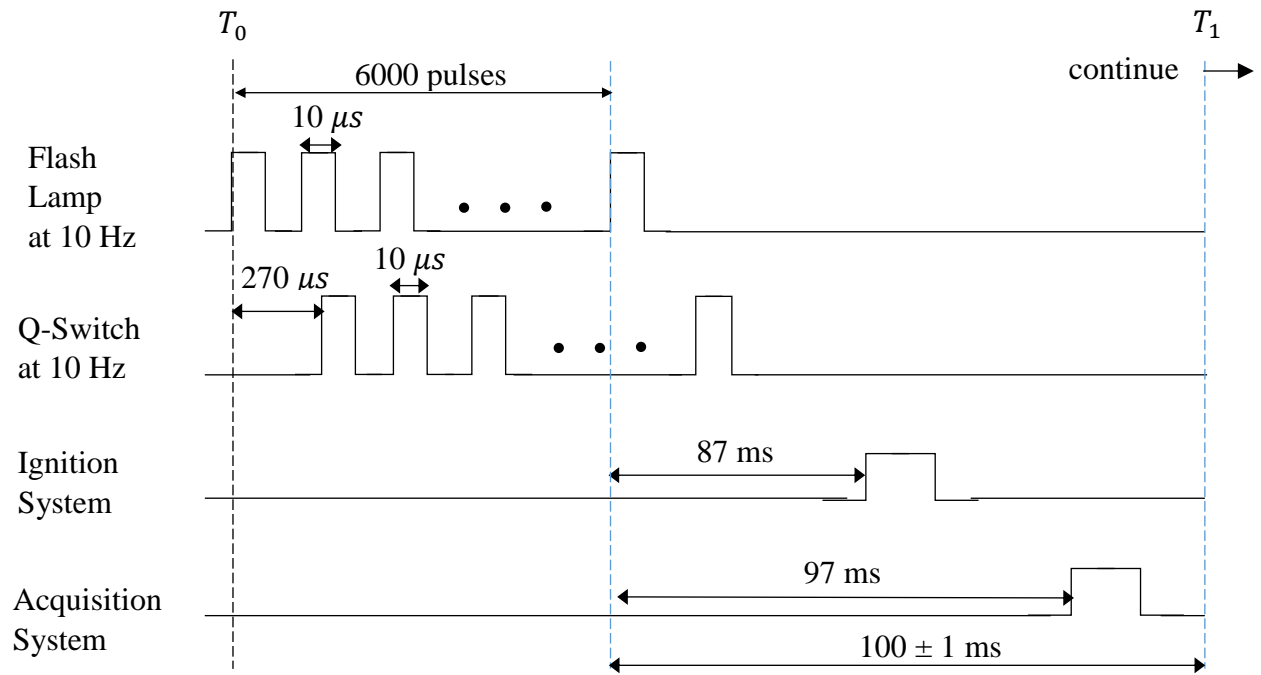Figure 42 -Schematic of the acquisition, ignition, delay signal, and PLIF-detonation system

I_1 I_2 I_3 I_4 P_4 P_5 P_6

CONDITIONER BOX
FOR IONIC PROBES

CONDITIONER BOX
FOR PRESSURE
SENSOR

SP_1 SP_2 SP_3

Conditioned signal

IGNITION
SYSTEM

PXIe NI - 1071
CHASSIS

NI PXIe-5105
Oscilloscope

Data

Positive TTL
signal to trigger

P_1

Addition relatively
to Fig. 30

BNC DELAY
GENERATOR 1

BNC DELAY
GENERATOR 2

DYE LASER
283 nm

Q-Switch
Flash
Lamp

Positive
Adjustable
signal (9 volts)

ICCD
CAMERA

Own authorship

The wavelength scan consists of vary the wavelength in the range of five or fewer picometers. Specific wavelengths will excite the fluorescence of the OH radical on the methane-air flame, at different intensities. All the intensities are recorded to plot the emission spectrum and compare, both theoretical and the experimental spectrum. The theoretical absorption spectrum is obtained from the spectral simulation tool LIF-BASE developed by (LUQUE; CROSLEY, 1999). Both spectrums, experimental and theoretical, need to be compared to determine the offset. The offset is valuable information to readjust the experimental spectrum, and so recognize the real spectral position. During the scan, triggering mode was internal, allowing the internal master lock to control the flash-lamp and Q-Switch. These devices are inside the laser and are the one that controls the amount of emitted light. As suggested by the manufacturer, both devices have to work at 10 Hz. Moreover, exist a delay between the triggering signals. The delay was 300 μs between Flash lamp and Q-switch, during the scan. However, it can be decreased until 270 μs, reaching maximum values of energy. Lower delay values can damage the dye in the long-term. The energy was measured by a power meter (Coherent-1098580), placed between mirror 1 and mirror 2. The energy emitted by the laser was kept constant in the range of 20 to 30 mJ, for each run.

The PLIF configuration includes new devices that have to be synchronized to capture fluorescence of the detonation at the right time. The dye laser had to be connected to the delay generator number one. The former device sends an adjustable positive signal at 10 Hz, to trigger the laser, acquisition, and ignition system externally. Two "T" junction was used to connect a second delay generator that will trigger externally the laser as well as the camera. Since the "T" junction affects the impedance of the system, a higher voltage had to be applied; for this reason, an adjustable voltage higher than 4 volts (TTL) was applied by both delay generators. As can be seen in Figure 42, the delay generator two was triggered by pressure sensor number one. For PLIF imaging, the position of the pressure sensor three was exchanged by position one. This change was necessary to control the delay time between Flash Lamp and Q-Switch properly.

The synchronization of the PLIF-detonation system was made by two delay generator and is depicted in Figure 43. The first delay generator (a) was in charge of triggering the externally the Flash Lamp, Q-Switch, ignition, and acquisition system. The second delay generator (b) triggers the Flash Lamp, Q-Switch and ICCD Camera. T_0 is the time when the delay generator is triggered manually. T_1, T_4, T_5 and T_6 is the time when the detonation wave arrives at the pressure sensors P_1, P_4, P_5 and P_6, respectively.

Figure 43 -Timing diagram for the PLIF-detonation system: (a) Signals created by the delay generator one, (b) Signals created by the delay generator two and continuation on timeline.

T_0

6000 pulses

10 μs

Flash
Lamp
at 10 Hz

270 μs 10 μs

Q-Switch
at 10 Hz

T_1

continue

Ignition
System

87 ms

Acquisition
System

97 ms

100 ± 1 ms

(a)

T_1 T_4 T_5 T_6

10 μs

Flash
Lamp
Single Pulse

173 μs

10 μs

Q-Switch
Single Pulse

270 μs

10 μs

ICCD
Camera

443.5 μs

(b)

Own authorship
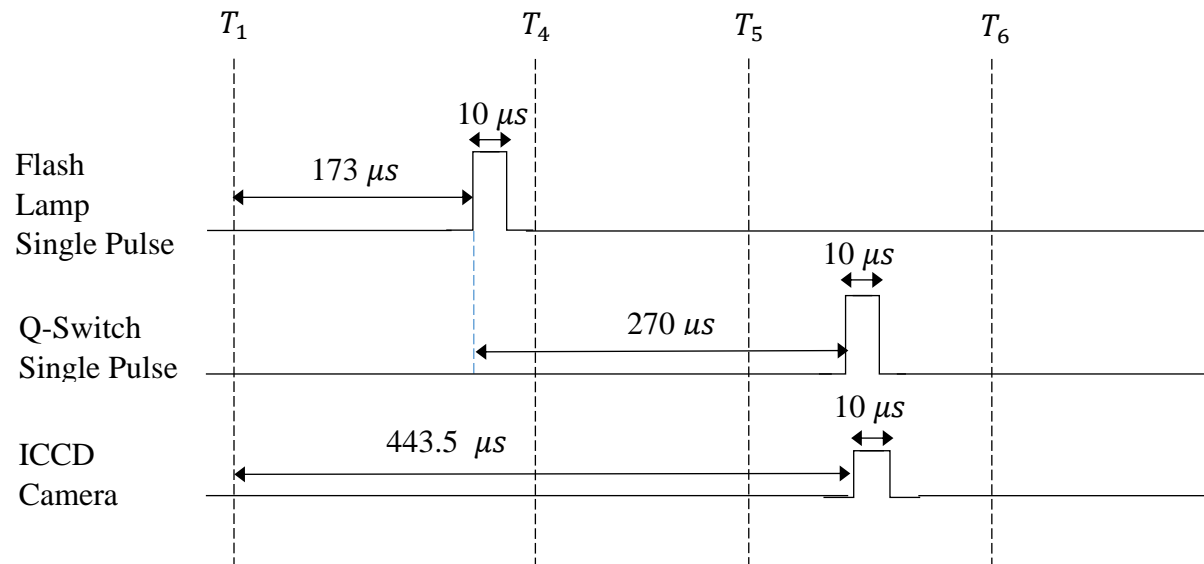
Since dye lasers cannot be trigger only for one shot, a synchronization strategy was done to warm up the laser before shot measurement. The strategy consists of sending six thousand pulses before the shot that will excite the detonation wave. This task was performed by delay generator one, given a positive TTL signal of ten-microsecond width for flash lamp and Q-Switch. To maximize the energy emitted by the laser, the delay between the flash lamp and Q-Switch was two hundred seventy microseconds. The frequency of the pulses is 10 Hz, and 6000 pulses are sent for ten minutes. The last Flash-lamp pulse triggered the ignition system with a delay of 87 ms. The delay was chosen based on the time that the wave spends since the ignition starts until it reaches the first sensor, the average time is 13 ms. Since the period of the flash lamp pulses is 100 ms (10Hz), the difference between 100 and 13 ms gives the approximate time to trigger the ignition system. As figure 31 shows, the ignition and acquisition system content a delay of 10 ms, the same delay is applied to the PLIF-detonation timing diagram, obtaining a total delay of 97 ms respect to the last Flash-Lamp pulse. The proposed timing took into account the laser period of 100 ms, for this reason, since the last Flash-Lamp pulse until the pressure sensor one is roughly 100 ms. This strategy was adopted to avoid damage on the dye laser and the optomechanics devices inside the laser. The variation of ±1 ms is caused by the changes in the mixture composition and oxidation process on the tip of the spark plugs. Even though the period (100 ms) is not precisely applied, the small variation of ±1 ms does not affect the dye detrimentally.

Once the mixture is ignited, the detonation propagates along the detonation tube. When the wave reaches the pressure sensor one, the second delay generator follows the synchronization. For the second stage of the synchronization, some preliminaries tests were carried out to determine the average time flight time between pressure sensor one and pressure sensor five. The average obtained of six runs at the same initial conditions is 403 μs. Therefore, take into account the time between pressure sensor five to the middle of the optical access mentioned on the Schlieren configuration (40 μs), the total time from pressure sensor one to the middle of the optical access is 443 μs. For this reason, Q-Switch is open at 443 μs to release the laser beam. Based on the preliminary measurements, the delay between the pressure sensor one to the flash lamp is 173 μs, to keep the 270 μs of delay time between Flash lamp and Q-Switch. Since the Q-Switch and flash lamp receive the triggering signal from both delay generators, the impedance decreases the applied voltage. So an adjustable voltage (9 volts) was applied to pass the threshold signal. TTL positive signals were only applied to the ICCD camera, acquisition system, and ignition system.

3.4. INITIAL CONDITION

All experiments were conducted at initial temperature of 20 °C. The initial pressure was varied among 400 mbar, 500 mbar, and 1bar. During the study, the equivalence ratio was varied in the lean zone, from 0.5 up to stoichiometric conditions. Either the initial pressure and the equivalence ratio of the mixture was controlled based on the partial pressure law. These initial conditions were used to find the cell size in the literature, see Appendix G . Measurements of the deposition energy by the spark plug was not taken into account; however, the same pulse width was applied for identical spark plugs. Around two hundred thirty runs have been performed in the laboratory. Most of those measurements are part of the preliminary studies to find the appropriate conditions to obtain detonations. In the results, only the most representatives run will be shown.

4   RESULTS

This chapter discusses the experimental results obtained on the detonation setup. In order to accomplish the first objective of this study, not only measurements had to be done, the building process of the whole detonation setup is necessary to be considered. Initially, the experimental setup has to be mounted according to the design. Some essential considerations had to be taken to design the setup; one is the cross-section width; this dimension has to be slightly more significant than the cell size so we can obtain a detonation. In addition to that, a metallic structure has been built to support the whole setup at the level of the laser beam. Static pressure tests were carried out before to take experimental measurements since leaks in constant volume vessel is one of the main issues. The leaking tests were important to choose the most effective gasket material that seals every junction. Once we made sure that leak rates were not considerable, we decided to start with the first experimental run.

The detonation results consist of pressure trace and velocity measurements. Firstly, the pressure trace of detonation wave and fast flames will be shown to point out the difference according to the detonation theory. Then, the propagation velocities of the shock wave will be presented for the three strategies proposed to enhance the transition from deflagration to detonation.

The images captured by the Schlieren process is shown for various conditions. Some of the results are for fast flame and others for detonations. Part of the results was captured by the CMOS camera and others by the ICCD camera; this variation will be pointed out on the results.

The PLIF results are divided into two sections, the scan process, and PLIF-detonation. The first section will show the results of the intensity recorded for the absorption spectrum scan. Based on the scan results, the calculated offset will be considered to perform the PLIF-detonation image.

4.1.   PRESSURE TRACE

One feature that highlights the ZND theory is pressure behavior over time. Figures 44 and 45 show the pressure trace collected by four pressure transducers. Figure 44 was performed at 0.7 equivalence ratio and 1 bar; this result was obtained using one spark plug and obstacle type one (First strategy).

Figure 44 -Fast flame pressure trace at 0.7 equivalence ratio and 1 bar, first strategy.

ER= 0.7
P = 1 bar
V = 682.6 m/s
Vcj= 1788.8 m/s
Pcj = 14 bar

Own authorship
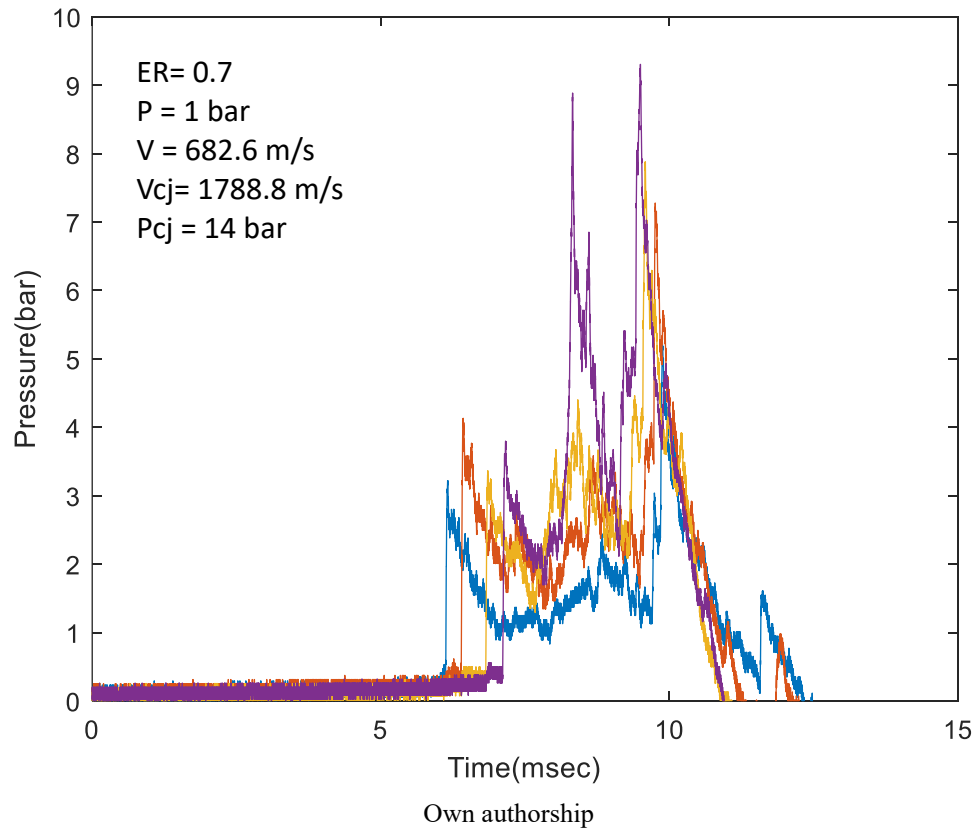
Figure 45 shows the pressure trace for 0.9 equivalence ratio and 1bar; this picture depicts the pressure behavior of a detonation, for this shot was used three spark plugs and obstacle type two (third strategy). The mains differences between both figures are the arrival time and pressure behavior. Since the transition to detonation was not successful, the arrival time between each sensor is wider for Figure 44 than Figure 45. Figure 45, unlike Figure 44, shows a narrow flight time because of the successful DDT. According to the ZND theory, the pressure of the mixture is compressed until the ZND state. Upstream this state, the pressure of a detonation slightly decreases. This pressure behavior is only observed in Figure 46, where the signal of each pressure sensor decreases gradually. The peaks registered at 6 ms is not part of the detonation pressure trace; it is a reflection of the detonation wave. The same pressure trace was not recorded for fast flames since high-pressure peaks were obtained upstream of the shock wave. The high peak register for fast flame, 9 bar, is a common explosion event that occurs when the mixture reaches the necessary temperature and pressure condition to auto-ignite.

Figure 45 -Pressure trace of detonation at 0.9 equivalence ratio and 1bar, third strategy

ER= 0.9
P = 1 bar
V = 1869.16 m/s
Vcj= 1918.9 m/s
Pcj = 15.48 bar
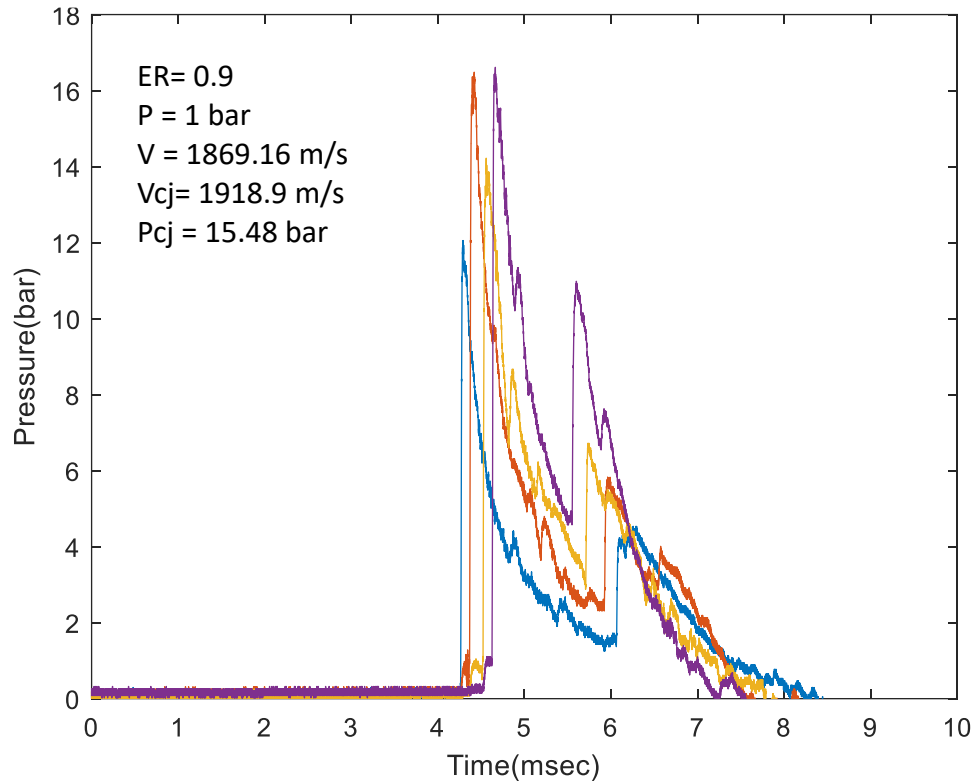
Since the most important velocity for optical diagnostic purposes is the average time of flight between pressure sensor five and six, the graphs only reported those. Obtaining a velocity of 682.6 m/s, for fast flame, and 1869.16 m/s for detonation. By comparing the measured velocity with the Chapman-Jouguet velocity, the variation for the fast flame is 61.58 %, and for detonation is 2.58 %, less than the theoretical speed. This comparison procedure was useful to confirm the regimen of the propagation. Another way to establish the occurrence of a detonation is by comparing the highest peak of pressure with the Chapman-Jouguet pressure. For the fast flame, the highest pressure was 4 bar; however, the ideal pressure for detonation is 14 bar; this confirms the lack of the detonation event. This discrepancy does not happen with the detonation run since the measured pressure roughly reaches 16 bar, and the ideal pressure is 15.48 bar. By making these comparisons, the regimen of the propagation was recognized for every run.

4.2. VELOCITIES

Four pressure transducers, mounted along the tube, recorded the detonation pressure and time-of-flight, which is used to calculate the wave-speed. For some measurements, both ionic probes and pressure sensors worked together to measure the velocity, recording six average speed points. For other runs, the concentration of ions was not enough to detect the peak of voltages on the ionic probes, creating a low signal to noise ratio; for these measurements, only the velocity determined by the pressure sensors is reported (3 average speed point). The measured velocity U, shown in the figures of this chapter, was obtained using the spent time to cross two sensors. Since detonation waves are imaging by Schlieren and PLIF in the fifth section, pressure transducer five and six reports the most important velocity. This velocity is determined at two meters downstream of the ignition system, in other words, in the middle of the optical access. This velocity has to be close to the Chapman-Jouguet velocity to imaging, by using the optical techniques, a real detonation. The reported Chapman-Jouguet velocity was obtained from the online tool: Chemical Equilibrium and Application, from NASA (SNYDER, 2019).

Typically, the behavior speed is not steady along the tube; this is the case for most of the runs performed on this thesis. As can be seen in Figure 46, after the detonation wave left the obstructed sections, the wave speed is 3100 m/s; this regimen is called overdriven detonations. Then, the velocity drops until 2020 m/s, relaxing the velocity and remaining almost constant until the optical access section; this stage is called the relaxation stage. The initial condition for this run is 0.5 bar and stoichiometric equivalence ratio. The given figure is detonation since the relaxation velocity is in the range of the CJ velocity (1950 m/s). This result was obtained by using the third strategy.

The first, second, and third strategies proposed in chapter 3.1 were carried out, obtaining the results shown in Figure 47, 48 and 49, respectively. The most representative results are solely shown on the figure to avoid many stacked lines on the graph.

The result obtained applying the first strategy are shown in Figure 47. By using this strategy, obstacle one and one spark plug the propagation velocities are in the regimen of fast flames. The geometry of the obstacle one does not create enough turbulence to activate the "turbulence loop" mechanism to transit to detonation. Even though the regimen is fast flames, the relaxation stage registered for detonation also occurs for these conditions. For a fast flame regimen, the equivalence ratio does not play a clear role over the velocity, since for high equivalence ratio (ER=1) was

registered high velocities but also the lowest one (ER=0.9). An important fact to mention is the lack of repeatability on this data, as can be appreciated in the values registered for 0.8 equivalence; they are differing 50 m/s. The no reproducible results might be the reason for the unclear influence of the equivalence ratio. By using this configuration, the behavior of the velocity in each run is not reproducible. However, an overall view of the result shows that the cell size for the highest velocity is 15 mm according to the database provided by Shepherd (2009), which is close to our cross-section width (20 mm). For the lower equivalence ratio, such as 0.5 or 0.6, the cell size is in the order of 80 mm, dimensions more significant than the cross-section width.

Figure 46-Development of the front wave propagation speed obtained from time-of-flight measurements using pressure transducers, initial condition: equivalence ratio 1 and 0.5 bar. (Third strategy)
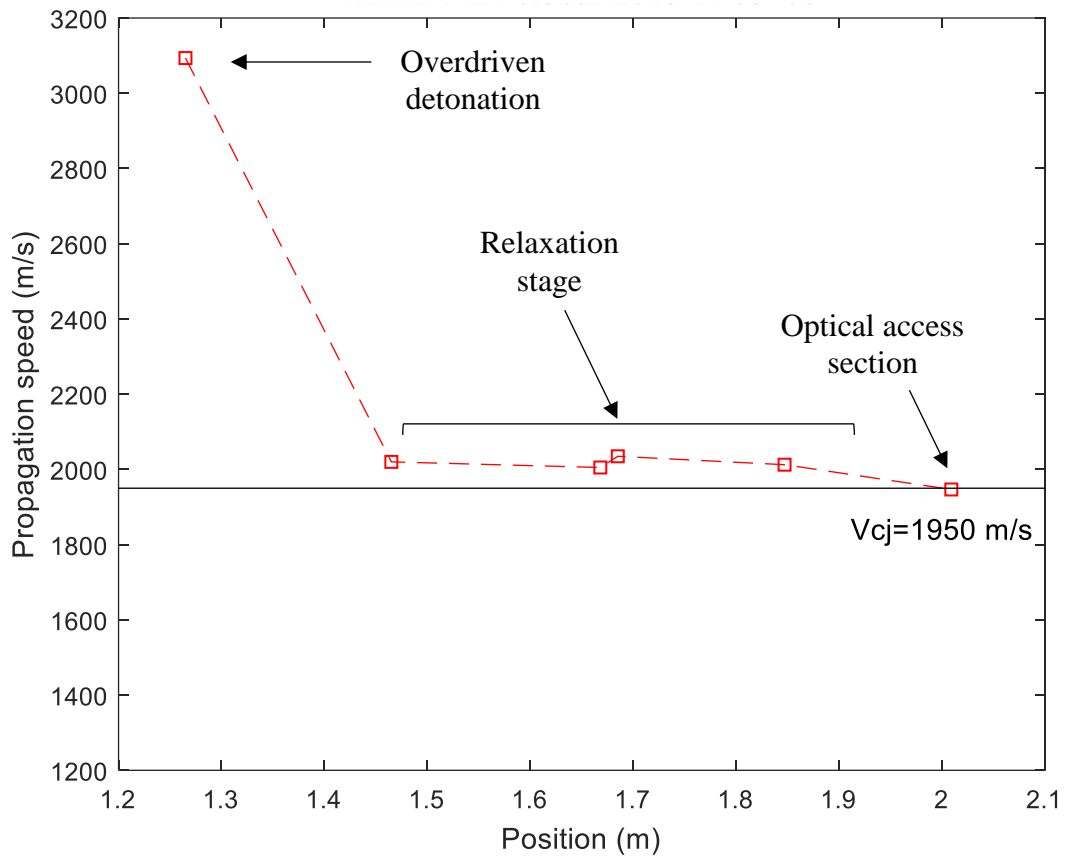
Own authorship

Figure 47 -Propagation speed using the first strategy

P=1 bar, BR= 0.47 and One spark plug
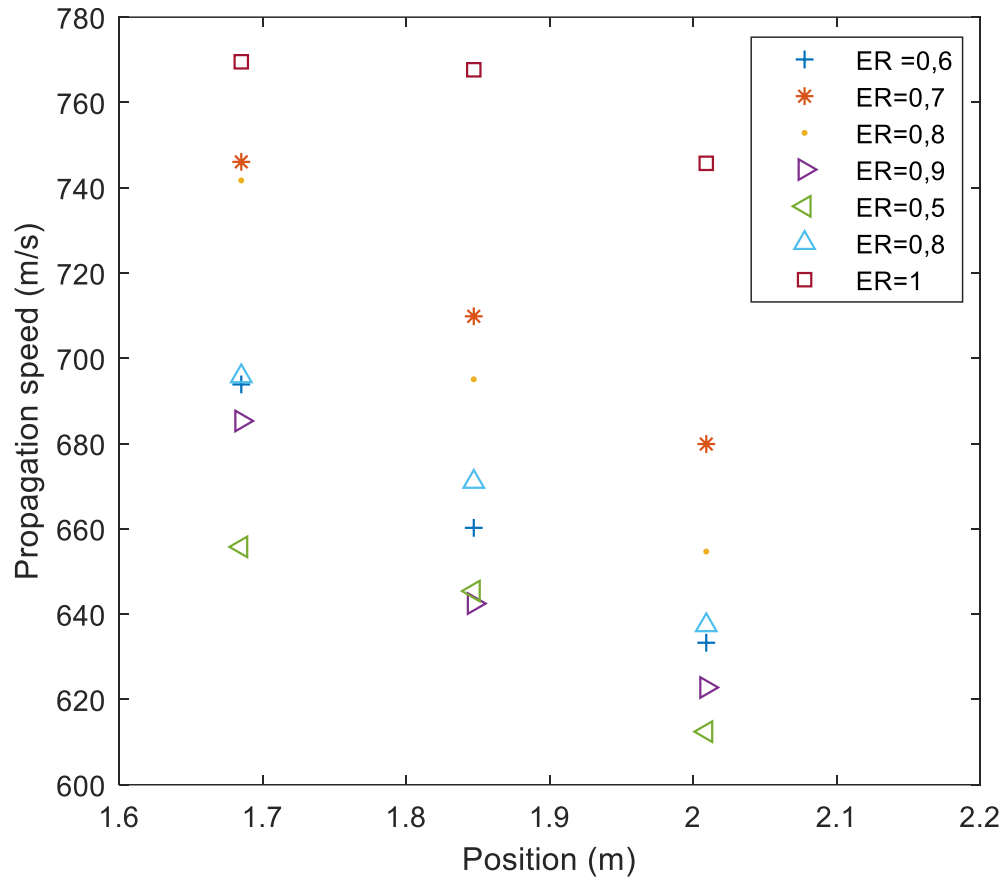
Own authorship

Figure 48 shows the track of the velocities along the setup working under four different initial conditions. For this graph, the second strategy was adapted to the detonation setup. The measured values show detonation events for 0.8, 0.9, and 1 equivalence ratios. At the beginning is noticed an overdriven detonation reaching velocities close to 3000 m/s, then the velocity drop lower than the CJ velocity to reaccelerate in the last section, the velocities registered in between in optical access are ± 2.5 % CJ velocity. For equivalence ratio 0.7, a particular behavior is appreciated since the cell size is larger than the cross-section width (27 mm); the front wave experienced a similar

behavior of a galloping detonation. This type of detonation was registered on the literature for long-distance, where detonation speed increase and decrease along the tube, suffering for reinitiation events, although this result seems to be failed detonation because the cell size (27 mm) and the low velocity achieved (756.4 m/s).

Figure 48 -Propagation speed using the second strategy

P=1bar, BR= 0.426 and one spark plug
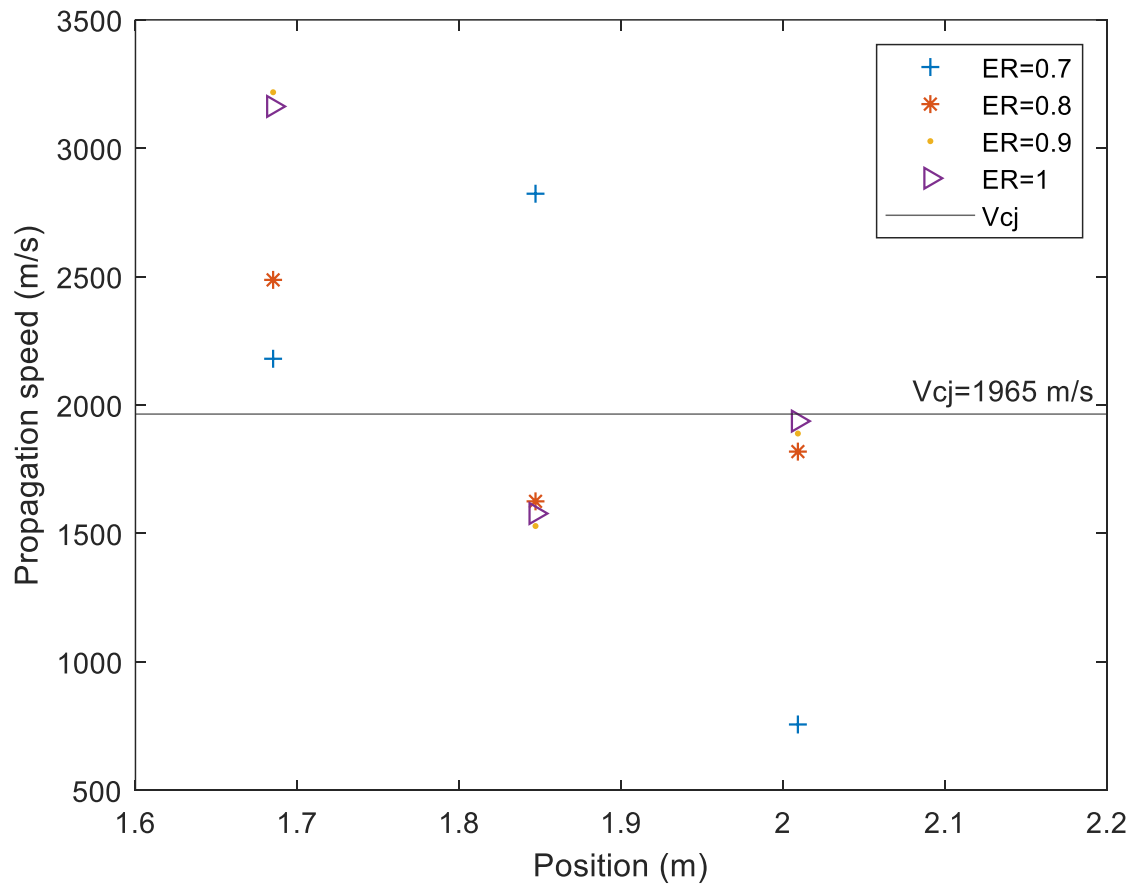
Own authorship

Even though the velocities in the optical access are in the detonation regimen, the trend is not close predictable. Based on the measurements, it is not possible to say that the detonation wave is roughly steady since the velocity suffers drops and peaks. Furthermore, the results are not constant, and this is proven in Figure 49. A study was done at 0.9 equivalence ratio and 1 bar, to prove the repeatability of the results. The result shows a gradual decrease in the velocity, behaving differently than Figure 49. The trend of the speed shows the same unsteady behavior of the detonation wave, as the previous figure. Also, three velocities, recorded on the optical access, underwent low values compared to Chapman-Jouguet velocity.

Figure 49 - Propagation speed using the second strategy

P=1bar, ER=0.9, BR= 0.426 and one spark plug
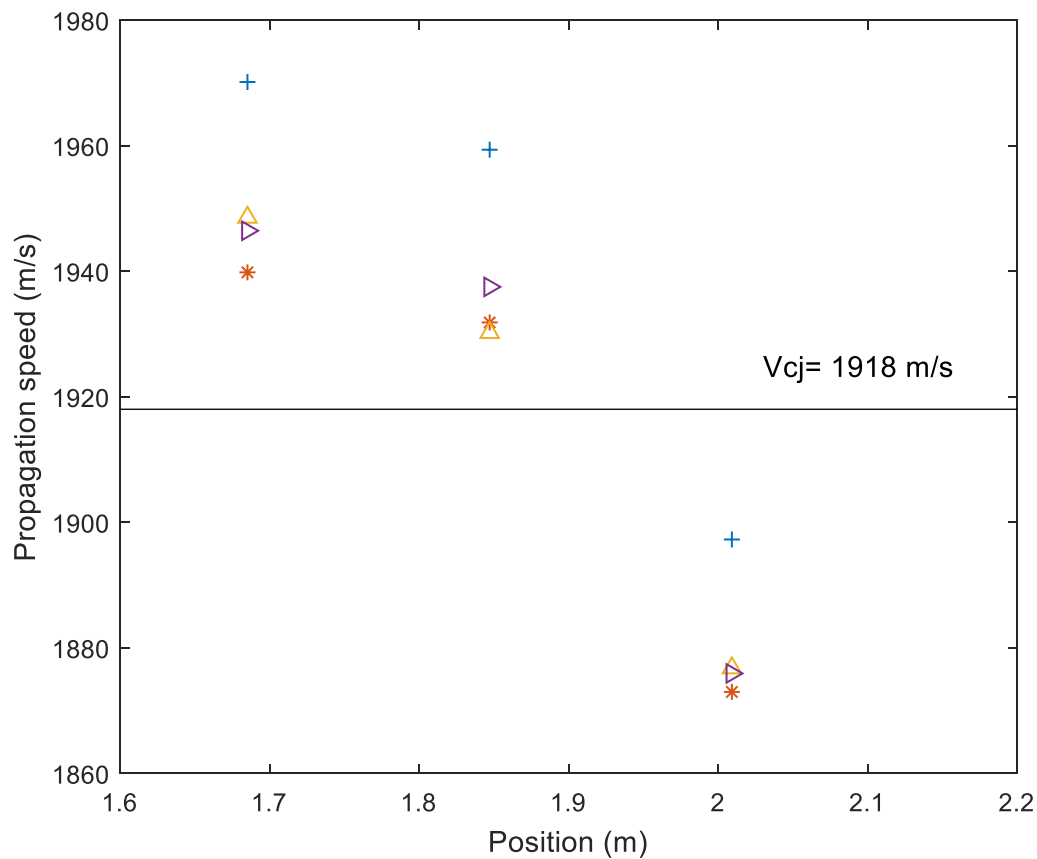
Own authorship

.

Figure 50 showed the results when the third strategy was adapted. The initial conditions for these measurements were selected in such a way that the cell size is not larger than the cross-section width. The trends of the velocity show a roughly steady detonation wave. The average velocities in the optical access are in the range of ± 5% CJ velocity, which is acceptable to imaging through the optical techniques.

Figure 50 -Propagation speed using the third strategy
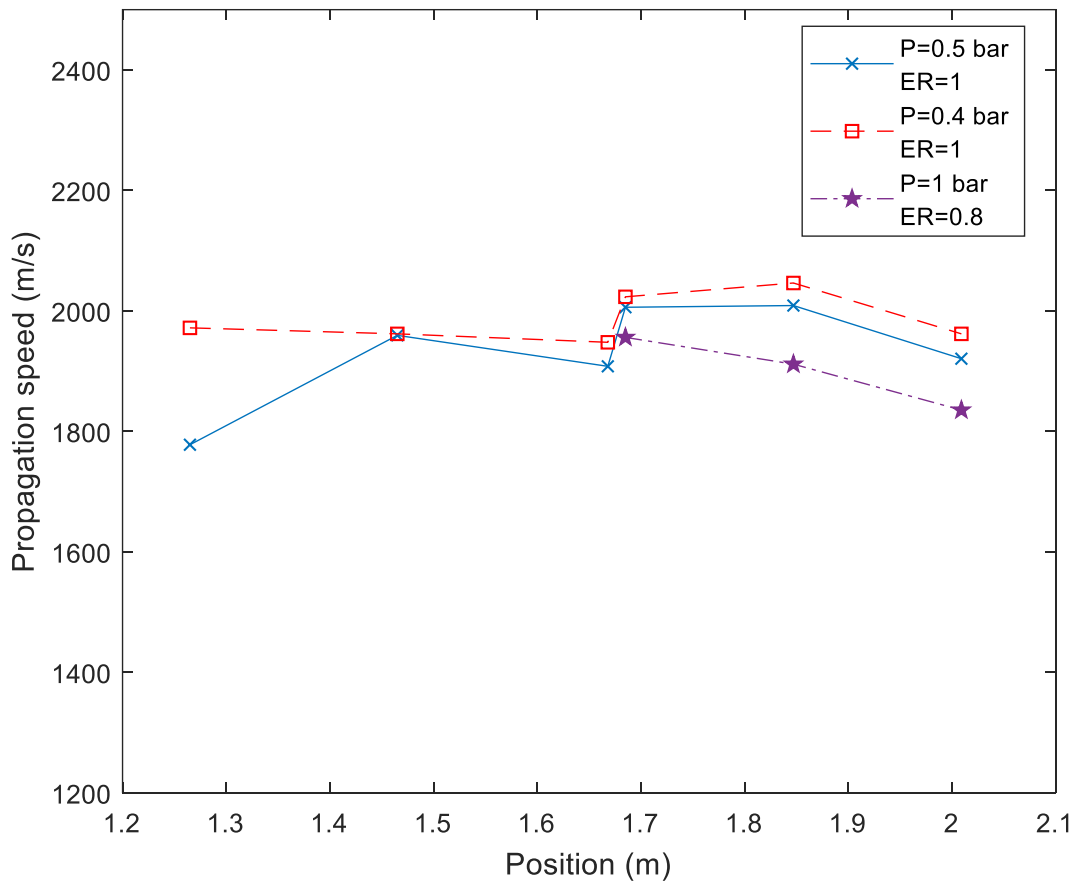
Own authorship

Based on measurements performed on the detonation setup, working with strategy three, a detonation map was depicted in Figure 51. This map shows two areas, detonation, and no

detonation. The initial condition working over the red line shows the combination that produces a detonation event.

By comparing the results of all strategies, the influence of the obstacle shape and deposition energy are the most influential parameters to obtain a steady detonation. The second obstacle has shown that it can increase the speed of the wave drastically. Moreover, the deposition energy provided the steadiness to the detonation wave.

Figure 51 -Detonation map occurrence for the square cross-section detonation setup
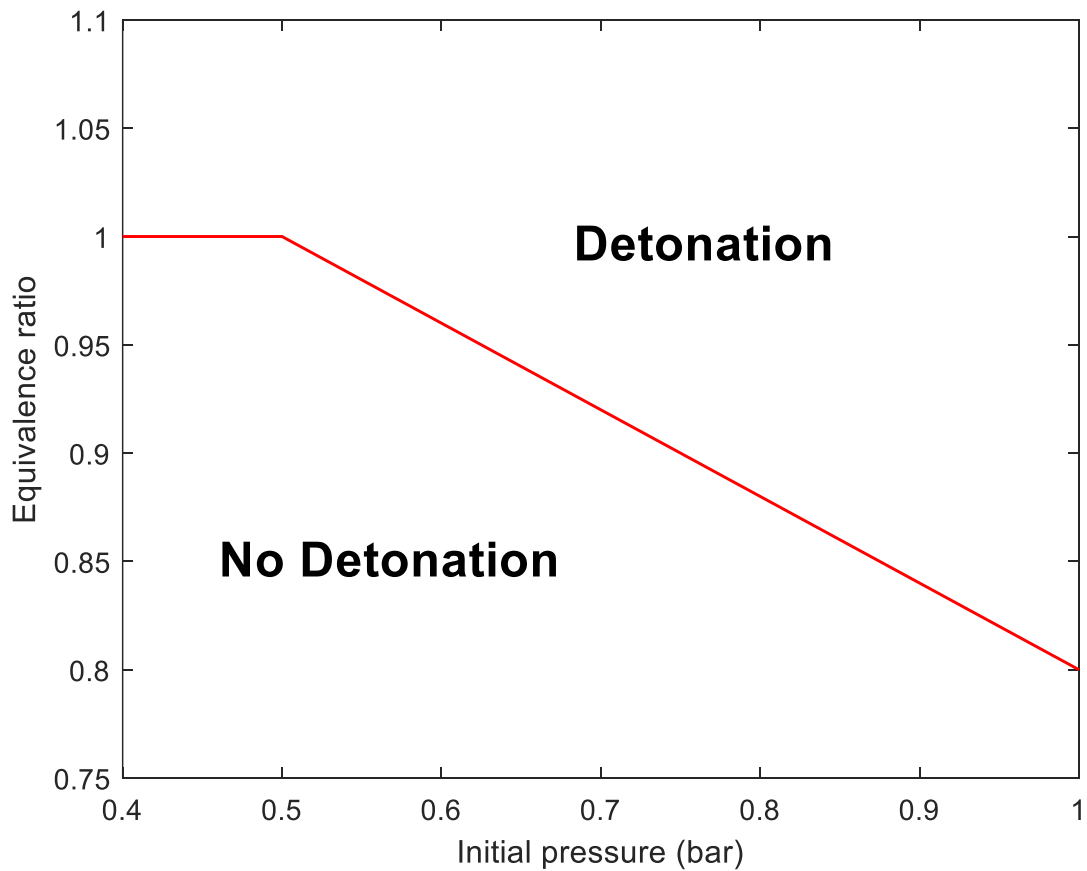
Own authorship

The dependence of the cell size on the velocity behavior was also studied under the last strategy. The result of this study is shown in Figure 52 and Figure 53. At the initial conditions of Figure 52, the cell size is 18.45 mm, and the cell size under Figure 53 conditions is 15.2 mm. The results showed a significant variation of the velocity for cell size close to the cross-section width (20 mm). The velocities for 0.4 bar varies in the range of ± 475 respect to the mean velocity. This fluctuation might be created by the high influence of the equivalence ratio on the cell size since a small change on the equivalence ratio can increase the cell size larger than 20 mm, so creating the unsteady behavior of the detonation wave. Detonation at 0.5 bar, unlike at 0.4 bar, shows a more steady trend of the velocity. In the beginning, the wave is highly unsteady, reaching low velocities as 1319 m/s. However, between 1.46 m and 2 m, the results showed a steady detonation wave, proving that working at relative lower cell-size dimensions than the cross-section width contributes with the steadiness of the wave.

Figure 52 -Propagation speed using the third strategy,

P=0.4 bar and ER=1
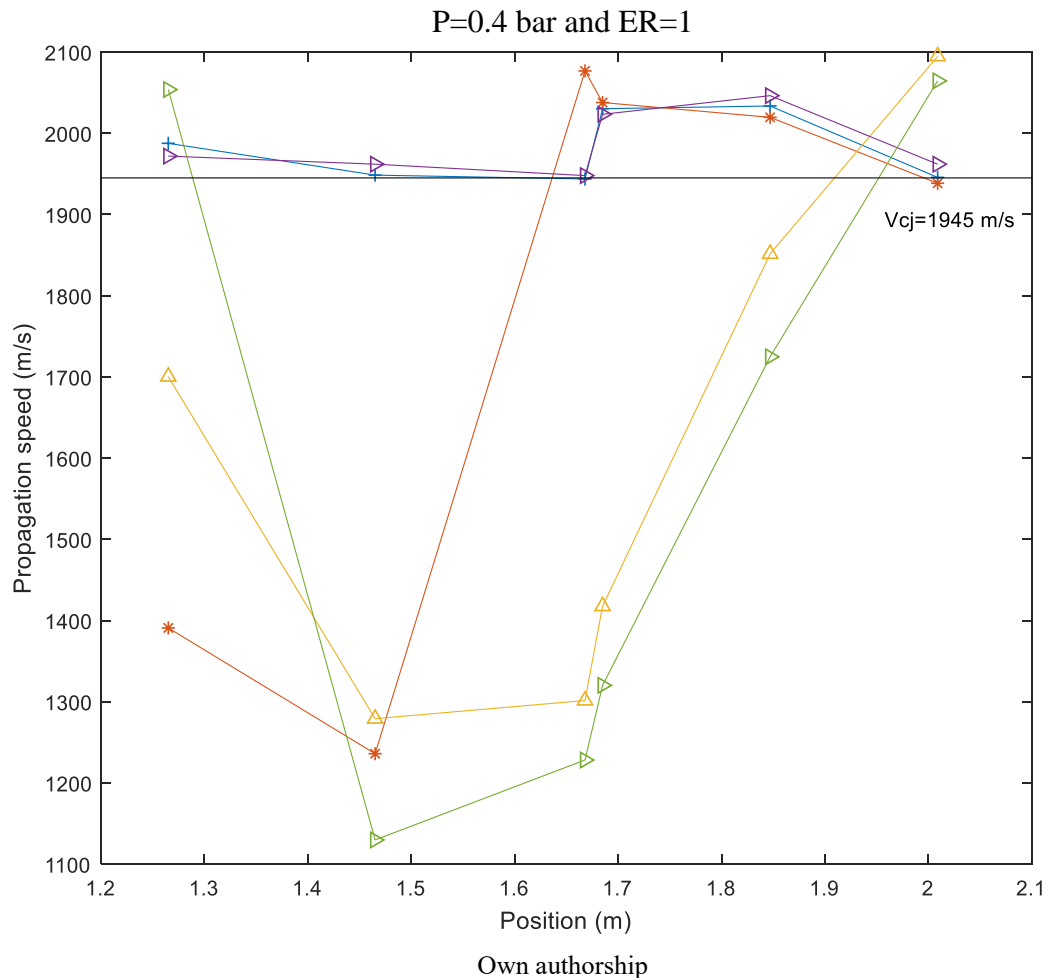
Own authorship

Figure 53 -Propagation speed using the third strategy,

P=0.5 bar and ER=1
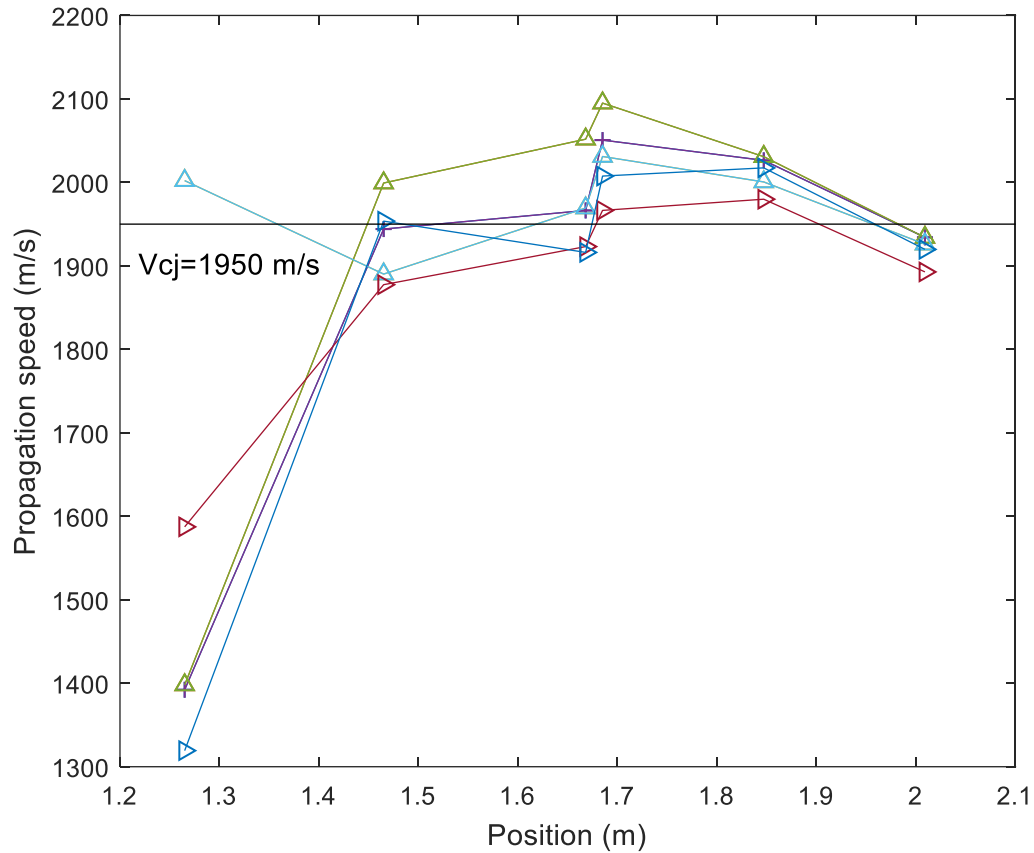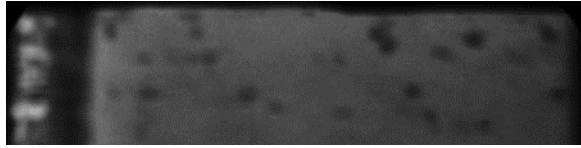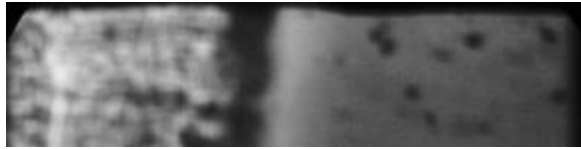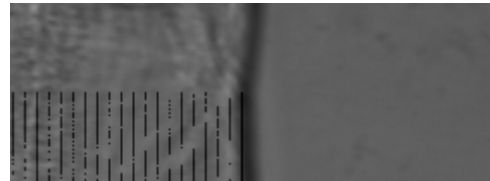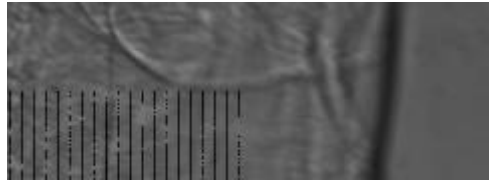
Own authorship

4.3. SCHLIEREN IMAGES

This chapter discusses the Schlieren pictures taken by the system depicted in Figure 35. However, not all the pictures belong to that system; actually, Figure 35 is the final Schlieren arrangement. In the beginning, a white light source and a CMOS camera were used. By using this camera, a slow track of the wave can be done by reducing the resolutions. The CMOS camera was used for Figure 54. The initial condition for both sets of images is 0.8 and 0.9 equivalence ratio,

and atmospheric pressure. These runs were performed under the first strategy. The frame rate of the camera was 100 kHz.

Figure 54 -Schlieren photograph of two fast flames development

Time	FAST FLAME (a) P=1 bar , ER=0.8, V = 640 m/s	FAST FLAME (b) P=1 bar , ER=0.9, V= 620 m/s
t= 0 s		
t=10 μs		
t=20 μs		

Own authorship

Both fast flames have low velocity compared to Chapman-Jouguet velocity. For this regimen, flames show a sharp shock following by transversal waves. These measurements were taken without any filter, in such a way that the light coming from the detonation is highlighted. However, for these images, only was detected the density gradient created by the shock wave. These results

mean for fast flames, the shock wave and the reaction zone are decoupled, contrary behavior than detonations.

In order to reveal more details of the waves, one single picture was taken by increasing the resolution at the maximum level of the CMOS camera. The images shown in Figure 56 have not used any filter in front of the camera. The exposure time for each picture was 1 μs. Image (a) fast flame close to the regimen of detonation. In the middle of the figure, a dark line represents the shock wave. Behind the shock wave reaction zone is represented by a bright area. Both the reaction zone and shock are decoupled, although the distance is not larger than the image (b). At the same condition but with a lower velocity, the reaction zone is delayed for image (b). Both images prove the dependence of the velocity to couple the reaction zone and shock wave. The same behavior occurs at lower pressure for image (c). This measurement was taken at 0.5 bar, and results show a fast flame with a high velocity, 22% of difference compared to the CJ condition. Even though the initial conditions are different for images (a) and (c), the results show a decoupled reaction zone and shorter induction length than the image (b).

Figure 56 shows Schlieren images for detonation events at different initial conditions. For images (a) and (b), the knife-edge was covering only the deflected light, allowing more light to integer during 1 μs of exposure time. For images (c) and (d), the knife-edge covered almost 50% of the light source image on the focal point, rejecting more light and so becoming darker. Image (a) shows a bright shock wave and blurry reaction zone that barely can be distinguished because of the light emitted by the detonation. For images (b), unclear cellular structure is possible to see in the shock wave. The cellular structure is covered by a bright vertical light representing the detonation light that affects the contrast of the picture. For images (c) and (d) a bright light represents the shock wave of the detonation. For both images, the cellular structure is not evident since the light emitted by the detonation is confused with deflected light that represents the shock wave. The purpose of these experiments was to prove experimentally the coupling of the reaction zone with the shock wave, an assumption taken by the ZND theory.

Figure 55 -Schlieren photograph captured by CMOS camera for hydrogen-air fast flames
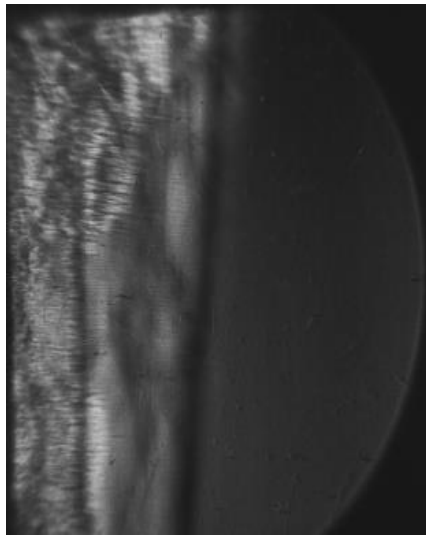
(a)

P=1 bar, ER=0.7

V=1500 m/s, Height=10 cm
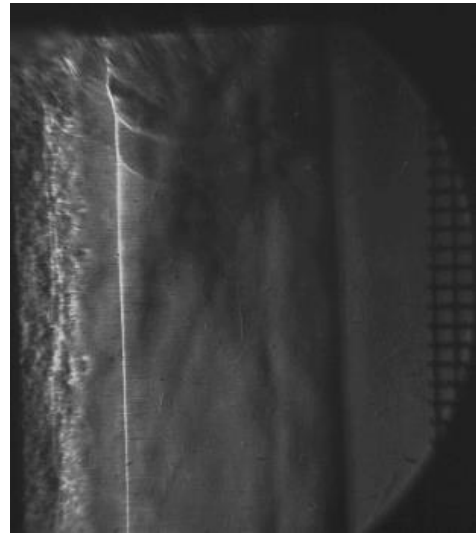
(b)

P=1 bar, ER=0.7

V=909 m/s , Height=10cm
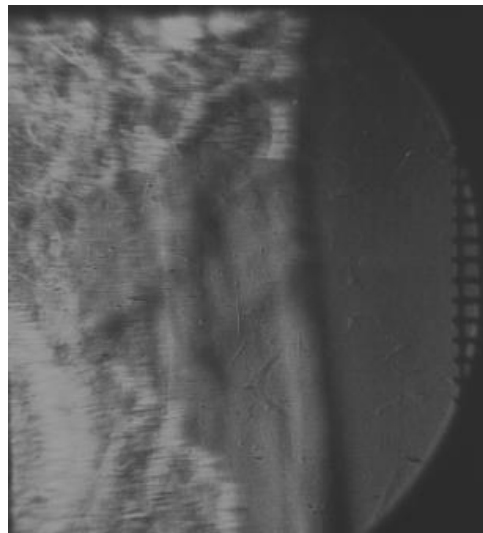
(c)

P=0.5 bar, ER=1

V=1460 m/s, Height= 10 cm

Own authorship

Figure 56 -Schlieren photograph captured by CMOS camera for hydrogen-air detonations
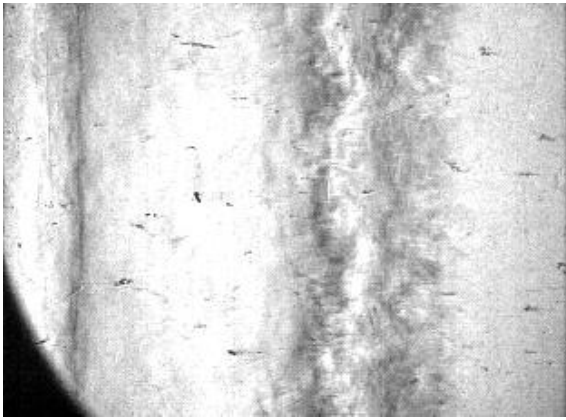
(a)

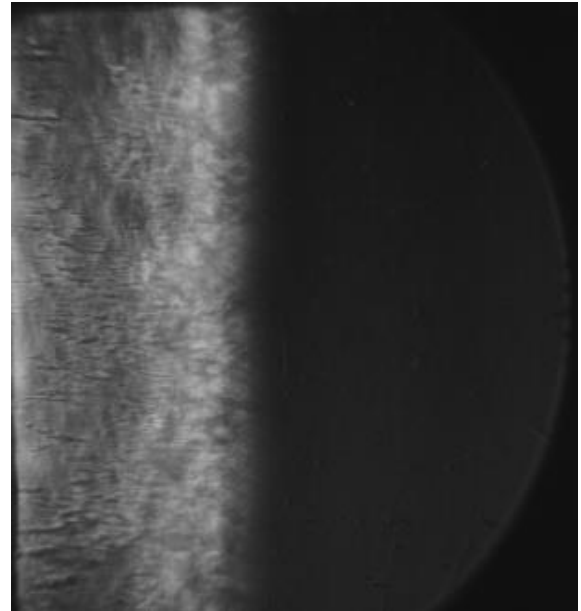P=1 bar, ER=0.9

V=1869 m/s
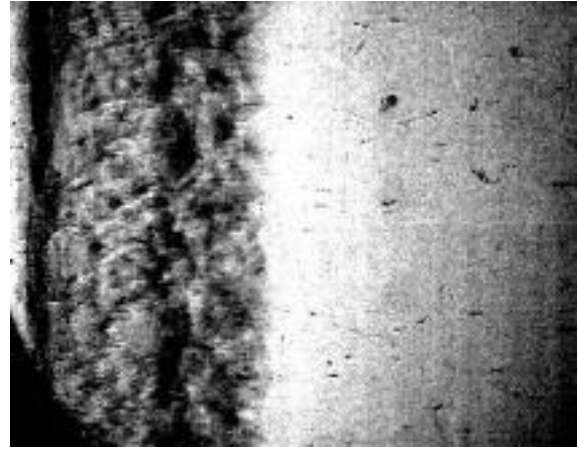
(b)

P=1 bar, ER=0.9

V=1852 m/s
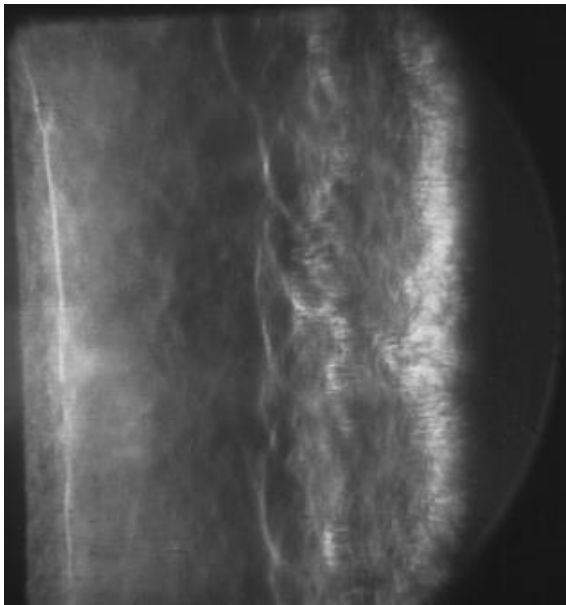
(c)

P=1 bar, ER=0.9

V=1875 m/s, Height= 10 cm

(d)

P=1 bar, ER=0.8

V=1818 m/s, Height= 10 cm

Own authorship

Some changes had to be made to image the cellular structure of the detonation and avoid blurriness caused by the interaction with light emitted by the reaction zone and long exposure time. These are a new blue light source, a bandpass filter (450 nm), and an ICCD camera. This is the last Schlieren configuration and is depicted in Figure 35. By doing these changes, the system can only detect the deflected beam of the light source, avoiding interference with the reaction zone. Figure 57 shows the Schlieren images for detonation events. The height of the images is 8.2 cm. The exposure time is 500 ns; this period avoids blurriness due to the high velocity of the wave. For these images, the bright light represents the regions with more density or more deflected light. The cellular structure can be easily recognized in each condition. The purpose of this set of experiments was to recognize the correct detonation structure and verify if the detonation wave is vertical or tilted. The former information is crucial to adapt the planar laser-induced fluorescence since tilted waves distort the intensity data from the wave, so avoiding an appropriate validation process for PLIF models. Figure 57 shown vertical detonation waves for all the conditions, meaning that the PLIF-imaging process will adequately record the intensity information of the reaction zone. More Schlieren images taken at the same conditions are in Appendix H.

Figure 57 -Schlieren photograph captured by ICCD camera for hydrogen-air detonations
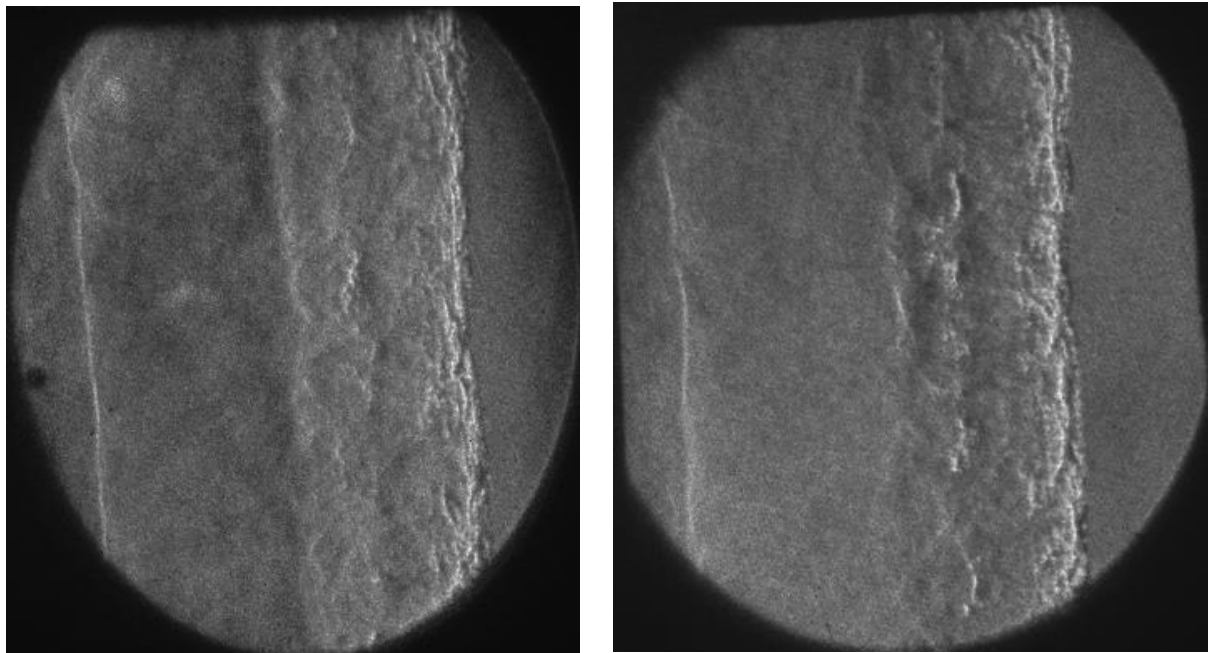
| (a) | (b) |
| P=0.4 bar, ER=1, V=1904 m/s | P=0.5 bar, ER=1, V=1904 m/s |
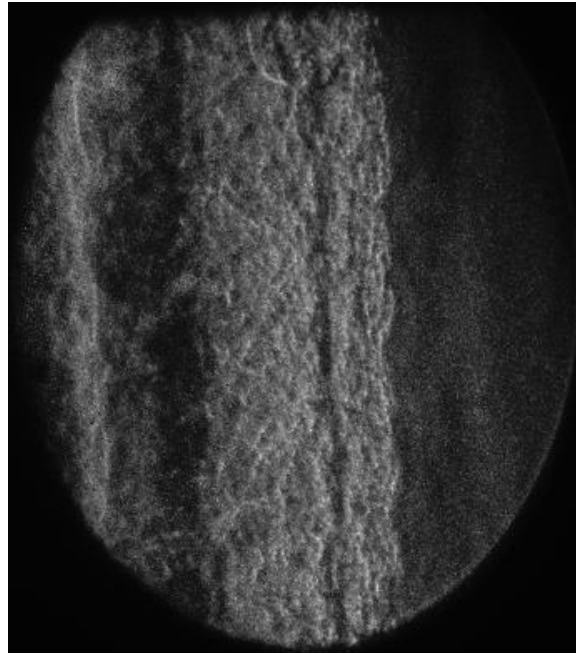
(c)

P=1bar, ER=0.9, V=181 m/s

Own authorship

4.4. PLANAR LASER-INDUCED FLUORESCENCE

The last optical diagnostic technique to be used was Planar Laser-Induced Fluorescence. This technique provided a different insight than Schlieren. By adopting this technique, the reaction zone of the detonation wave was revealed. Even though the Schlieren and PLIF techniques were no applied simultaneously, the single PLIF image provided useful information about the intensity profile and reaction zones. The process to perform PLIF measurements are two for these experiments: scan process and single-shot PLIF-image. The scan process was done by using a laminar methane-air flame to realize continuous measurements. By sending a laser beam pulse at 10 Hz, the OH radical was excited to record the experimental spectrum. This spectrum was compared with the simulated spectrum obtained from the LIF-base software. The purpose of the process is to identify the offset and applied the correction when the transition wavelength is chosen. The scan process consisted of applied a wavelength on the laser controller and record the average

intensity registered by the ICCD camera by post-processing the virtual file obtained from the Winspec software. The process needed to increase gradually $5.10^{-3}\ nm$ to the previous wavelength and record the average for each new wavelength. The result obtained from this scan is shown in Figure 58. This image was taken by the PLIF configuration depicted in Figure 42. This figure depicts the experimental and simulated spectrum. Although the step width was large, the shape of the experimental spectrum match with the simulated spectrum, allowing the determination of the offset. The offset was calculated on the LIF-base software giving the result of 60 pm. The values are also shown in Appendix I.

Figure 58 -Experimental Methane-air flame spectrum and simulated spectrum by LIF-base.

Step width $= 5.10^{-3}\ nm$

Own authorship
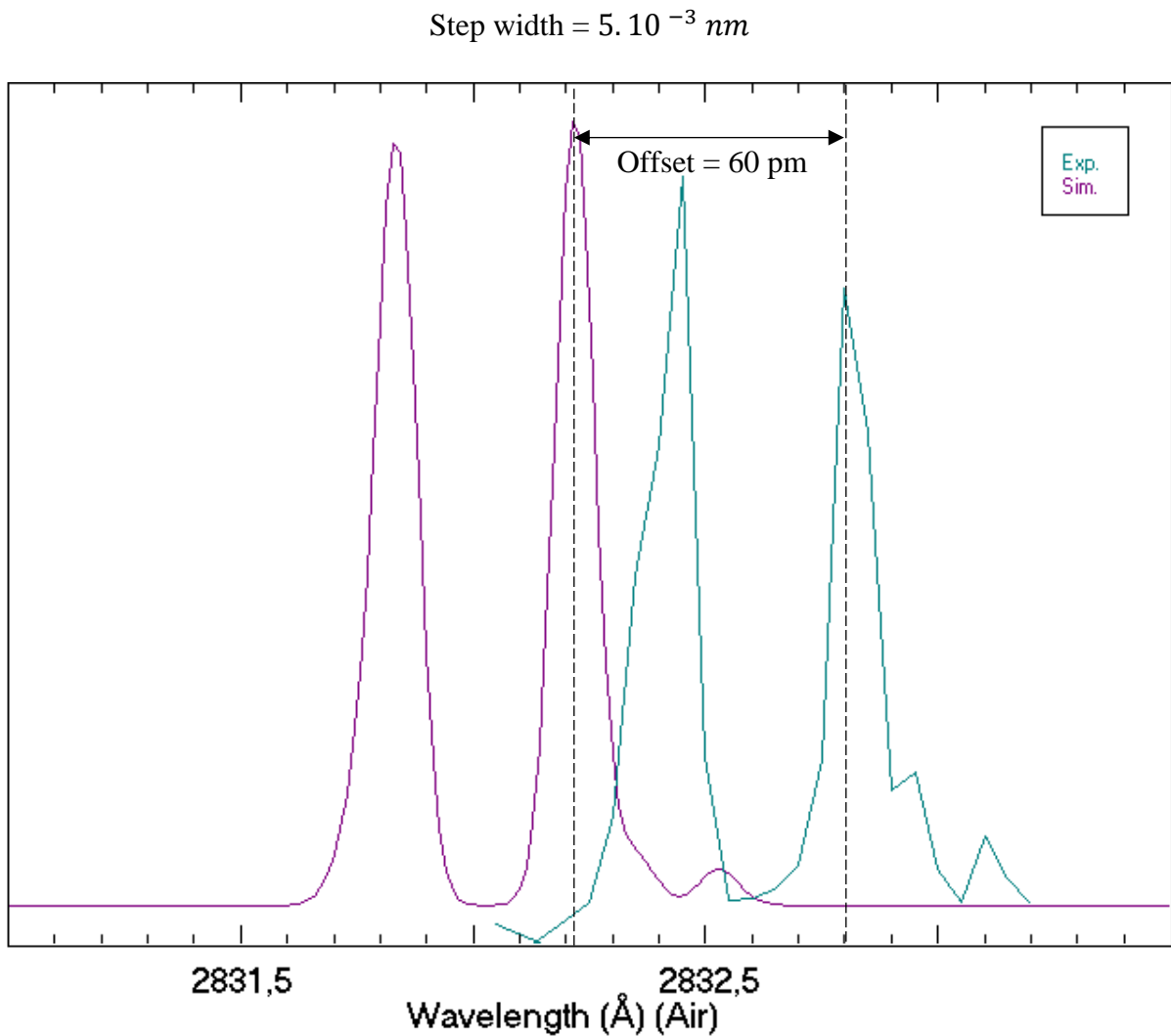
The OH distribution for hydrogen-air detonation at 0.5 bar, 293 K of temperature, and stoichiometric mixture is shown in Figure 59. The chosen transition line was 2832,219 Å, but the adjusted wavelength by the offset was 2.832,819 Å. This image was taken by the PLIF configuration depicted in Figure 41. This single image provides the reaction zone for the different wave structure on the detonation wave. As can be seen, the coupling between the reaction zone and the shock wave also affect reaction zone structure since the OH distribution shapes depend on the cellular wave structure created on the shock wave. The interaction between cellular structure and reaction zone can be analyzed in detail by using the Schlieren and PLIF technique simultaneously. The most important insight provided by this picture is the intensity profile, image (b) depicts the development of the OH intensity along the detonation. To obtain this profile, a picture of the background had to be taken. The array of intensity was obtained by subtracting PLIF and the background image. Then, the sum of intensities registered by each column of pixels was performed. The normalization was done concerning the maximum intensity value obtained on the array. The size array was the 1024x500, the means that the region of interest was the left side of the image divided by the reference line. The x-axis starts from the reference line, and it develops upstream of the detonation wave. The fluorescence profile shows a sharp increase in the intensity at the beginning of the reaction zone, reaching its maximum value at 16 mm respect to the reference line. Then, the intensity undergoes a fast decrease until it reaches the background level at 40 mm. The intensity could be slightly higher than zero upstream the 40 mm because the wave was captured almost at the beginning of the FOV. This profile can be performed for small cellular regions and provide a useful intensity profile for validation of PLIF-models.

Figure 59 (a) PLIF images of OH distribution for hydrogen-air detonation, (b) intensity profile of hydrogen and air detonation

P=0.5 bar, ER=1, V=1923 m/s, length= 141.20 mm
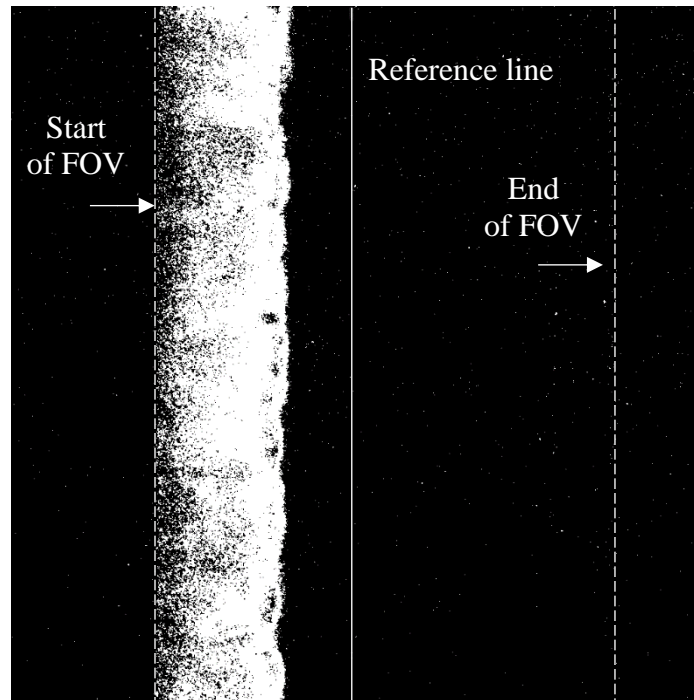
(a)
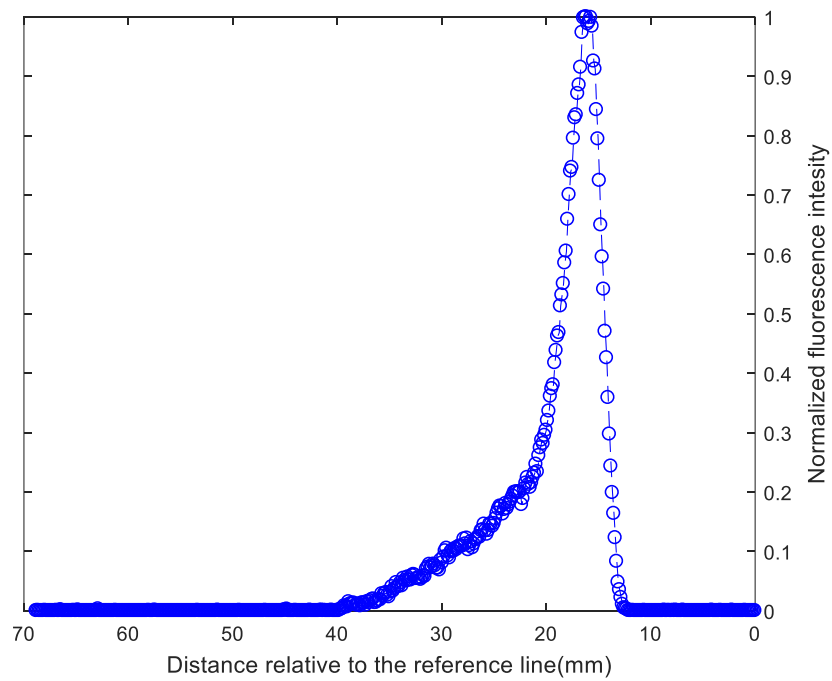
(b)

Own authorship

5   CONCLUSIONS

Experimental measurements of hydrogen-air detonations have been studied in the square section cross-section setup. The performed measurements were related to the pressure and velocity of the detonation waves. The pressure trace recorded for detonation and fast were different n terms of the maximum values. Detonation, unlike fast flame, registered high peak pressure in the range of Chapman-Jouguet state. These results revealed the importance of the pressure exerted over the reactants to start the formation of radical through chain branching process. Since all the detonation events happen at the Chapman Jouguet pressure and every fast flame event occurs at a lower pressure than Chapman Jouguet, this leads to the conclusion that detonation events can only be triggered if the reactants reach the required pressure obtained by the CJ theory.

The propagation speed of the detonation wave was recorded to study the influence of obstacle shape and number of ignitions sources. Comparing the results of the first and second strategies, it was proved that the uniform shape of the obstacle enhances the transition from deflagration to detonation. These results highlighted the importance of the shape of the obstacle to characterize DDT events rather than used the blockage ratio. The influence of the uniform obstacle might be related to the fact that the flame front is obstructed in two dimensions, thus creating more waves that interact with each other and so creating more turbulence, which is a key parameter to accelerate the flame according to the "turbulent loop" mechanism for obstructed channels. Even though the shape of the obstacle highly influences the velocity of the flame, this does not ensure constant velocity along the detonation tube. The addition of more ignition source has achieved the stabilization of the velocity at near two meters downward the position of the spark plugs, proving the importance of the amount of the spark plugs to obtain stable detonations. The explanations for this result relays on the creation of multiples flames front that interacts before they go through the obstacle, so creating early turbulence. A third study based on the velocity was done to understand the influence of the cell size on the steadiness of the propagation speed. The initial conditions that contain cell size larger than the cross-section width underwent transient behavior of the velocity. This behavior might happen because the cellular structure is an intrinsic feature of detonation, so conditions that allow the existence of the cellular structure can become in a steady detonation.

The Schlieren pictures recorded for fast flames revealed the strong decoupling between the reaction zone and the shock wave. The decoupling between both discontinuities can be recognized by the larger induction length or separation of them. According to these results and pressure trace recorded for fast flames, it is concluded that the pressure influence in the induction length. Since the Chapman Joughet pressure is not achieved for these runs, the reactants take more time in the induction zone creating the necessary radicals to release energy in the reaction zone. Even though the reaction zone is created, the discontinuities are not close enough to sustain the detonation. For detonations, Schlieren images without a bandpass filter show that the light emitted by the detonation covers the shock wave, hiding the cellular structure. This experiment proves that at detonation regimens exists a coupling between the reaction zone and shock wave. Schlieren images of the detonation with the bandpass filter (450 nm), showed the cellular structure in the shock wave was recognize. These pictures confirm the existence of cellular structure occurred at different initial conditions that allow detonations. Furthermore, detonation with unsteady speed behavior has not shown the cellular structure; this was the case for some runs shown in Appendix H at 0.4 bar and stoichiometric mixture. This experiment proves that the cellular structure only happens under steady conditions.

The picture obtained by using the technique planar laser-induced fluorescence has shown a reaction zone affected by the cellular structure of the shock wave. This pattern might be created by the gradient of velocity in the shock wave that pulls some areas of the reaction zone towards the shock wave for higher velocities and leaves other areas behind for lower velocities. Unlike results at lower pressure and high dilution conditions shown in the literature, this image does not show any keystone structure in the reaction zone. The reason might be due to the lack of regularity of the cell size, as can be seen in figure 59. The intensity profile revealed a rapid increase at the beginning of the reaction zone followed by a fast decrease. This behavior was already found by other experimental studies. However, further studies need to be performed to understand the influence of the high absorption at the beginning of the reaction zone and how it might affect the profile of the intensity behind it.

REFERENCE

ABRAMCZYK, H. Introduction to laser Spectroscopy. **Elsevier**, Poland, v. 53, n. 9, p. 50–52, 2005.

AUSTIN, J. M. K. **The role of instability in gaseous detonation**. 2003. 202 p. Dissertation (Ph.D.), California Institute of Technology. Pasadena, 2003. Available in: doi:10.7907/X7YH-T687. Access in: 26 feb. 2020.

AUSTIN, J. M.; PINTGEN, F.; SHEPHERD, J. E. Reaction zones in highly unstable detonations. **Proceedings of the Combustion Institute**, Pasadena, v. 30, n. 2, p. 1849–1857, 2005.

CHAPMAN, D. On the rate of explosion in gases. **Philosophical Magazine and Journal of Science**, [*S. l.*], v. 47, 1899.

CHATELAIN, K. et al. Effect of Incident Laser Sheet Orientation on the OH-PLIF Imaging of Detonations. *In*: INTERNATIONAL COLLOQUIUM ON THE DYNAMICS OF EXPLOSIONS AND REACTIVE SYSTEMS, 27., 2019, Beijing.**Anais** [...] Beijing: Institute of Explosions and Reactive Systems, 2019.

CICCARELLI, G.; DOROFEEV, S. Flame acceleration and transition to detonation in ducts. **Progress in Energy and Combustion Science**, Canada, v. 34, p. 499–550, 2008.

MEVEL, R. et al. Application of a laser induced fluorescence model to the numerical simulation of detonation waves in hydrogen-oxygen-diluent mixtures. **International Journal of Hydrogen Energy**, Pasadena, v. 9, 2014.

DOERING, W. On detonation processes in gases. **Annalen der Physik**, Russia, v. 43, 1943.

DOROFEEV, S. B. Flame acceleration and DDT in gas explosions. **Journal De Physique. IV : JP**, France, v. 12, n. 7, 2002.

FORMAN, W. **Combustion Theory**. 2 .ed. London: CRC press, 1985.

FROLOV, S. M.; AKSENOV, V. S.; IVANOV, V. S. Experimental proof of Zel'dovich cycle efficiency gain over cycle with constant pressure combustion for hydrogen-oxygen fuel mixture. **International Journal of Hydrogen Energy**, Russia, v. 40, n. 21, p. 6970–6975, 2015.

GORDON, R. L.; MASRI, A. R.; MASTORAKOS, E. Simultaneous Rayleigh temperature, OH- and CH2O-LIF imaging of methane jets in a vitiated coflow. **Combustion and Flame**, Germany, v. 155, n. 1–2, p. 181–195, 2008.

GRAY, J. A. T.; LACOSTE, D. A. Enhancement of the transition to detonation of a turbulent hydrogen–air flame by nanosecond repetitively pulsed plasma discharges. **Combustion and Flame**, Saudi Arabia, v. 199, p. 258–266, 2019.

GRAY, J. A. T. et al. Thermodynamic evaluation of pulse detonation combustion for gas turbine power cycles. *In*: TURBOMACHINERY TECHNICAL CONFERENCE AND EXPOSITION, 2016, Seoul. **Anais**.[...] Seoul: Proceedings of ASME Turbo Expo, 2016.

JOUGUET, E. On the propagation of chemical reactions in gases. **Journal de Mathematiques Pures et Appliquees**, France, v. 1, 1905.

KESSLER, D. A.; GAMEZO, V. N.; ORAN, E. S. Simulations of flame acceleration and deflagration-to-detonation transitions in methane – air systems. **Combustion and Flame**, United States, v. 157, n. 11, p. 2063–2077, 2010.

LEE, J. **The detonation Phenomenon**. 1. ed. United States: Cambridge University Press, 2008.

LIBERMAN, M. A.; KIVERIN, A. D.; IVANOV, M. F. On detonation initiation by a temperature gradient for a detailed chemical reaction models. **Physics Letters A**, Russia, v. 375, n. 17, p. 1803–1808, 2011.

LISANTI, J. C.; ROBERTS, W. L. Pulse combustor Driven Pressure Gain Combustion for high efficiency Gas Turbine Engines. **Combustion for Power Generation and Transportation: Technology, Challenges and Prospects**, United States, v. 1, p. 3–8, 2017.

LUQUE, J.; CROSLEY, D. **Database and spectral simulation (version 1.5)**, SRI international, 1999.

MÉVEL, R. **Detonation waves in gases**. 1. ed. Beijing: Tsinghua University, 2018, p. 50–60.

NICHOLLS, H. R.; WILKINSON, R. B.; MOR, J. A. Intermittent Detonation as a Thrust-Producing Mechanism. **Journal of Jet Propulsion**, United States, v. 27, n. 5, p. 534–541, 1957.

PINTGEN, Florian. **Laser-Optical Visualization of Detonation Structures**. Advisor: Prof. J.E. Shepherd. 2000. Thesis (Master in Mechanical Engineering) - Department of thermodynamics, Technical University of Munich, Munich, Germany, 2000.

PINTGEN, Florian. **Detonation diffraction in mixtures with various degrees of instability**. Advisor: Prof. J.E. Shepherd. 2005. Thesis (Doctor of Philosophy) - Department of Mechanical Engineering, California Institute of Technology, California, 2005.

Princeton Instruments, P. User manual of PI-max 3 system. **Princeton Instruments documentation**, United States, v.1, p. 1–6, 2003.

RANKIN, B. A. et al. Investigation of the structure of detonation waves in a non-premixed hydrogen-air rotating detonation engine using mid-infrared imaging. **Proceedings of the Combustion Institute**, United States, v. 000, p. 1–8, 2018.

ROTHMAN, L. S. et al. The HITRAN molecular spectroscopic database: Edition of 2000 including updates through 2001. **Journal of Quantitative Spectroscopy and Radiative Transfer**, United States, v. 82, n. 1–4, p. 5–44, 2003.

SCOPUS. Publications made per year related to Hydrogen-air. United States, 2019. Disponível em: https://www.scopus.com/search/form.uri?display=basic. Acesso em: 27 jan. 2020.

SETTLES, G . **Schlieren and Shadowgraph Techniques**. 1. ed. New York: Springer, 2001.

SHEPHERD, J. E. Detonation in gases. **Proceedings of the Combustion Institute**, California, v. 32, n. 1, p. 83–98, 2009.

SNYDER, C. **Glenn Research Center NASA**. United States, Available in: https://www.nasa.gov/centers/glenn/home/index.html. Access date: 15 nov. 2019.

THORLABS. **Thorlabs, Inc. - Your Source for Fiber Optics, Laser Diodes, Optical Instrumentation and Polarization Measurement & Control**. New Jersey. Available in: https://www.thorlabs.com/. Access date: 10 nov. 2019.

VON NEUMANN, J. Theory of detonation waves. **Pergamon Press,** New York, v. 1, 1942.

ZELDOVICH Y.B. On the theory of the propagation of detonation in gaseous systems. **Journal of Experimental and Theoretical Physics**, United States, v. 10, 1940.

APPENDIX A - Full view of detonation setup
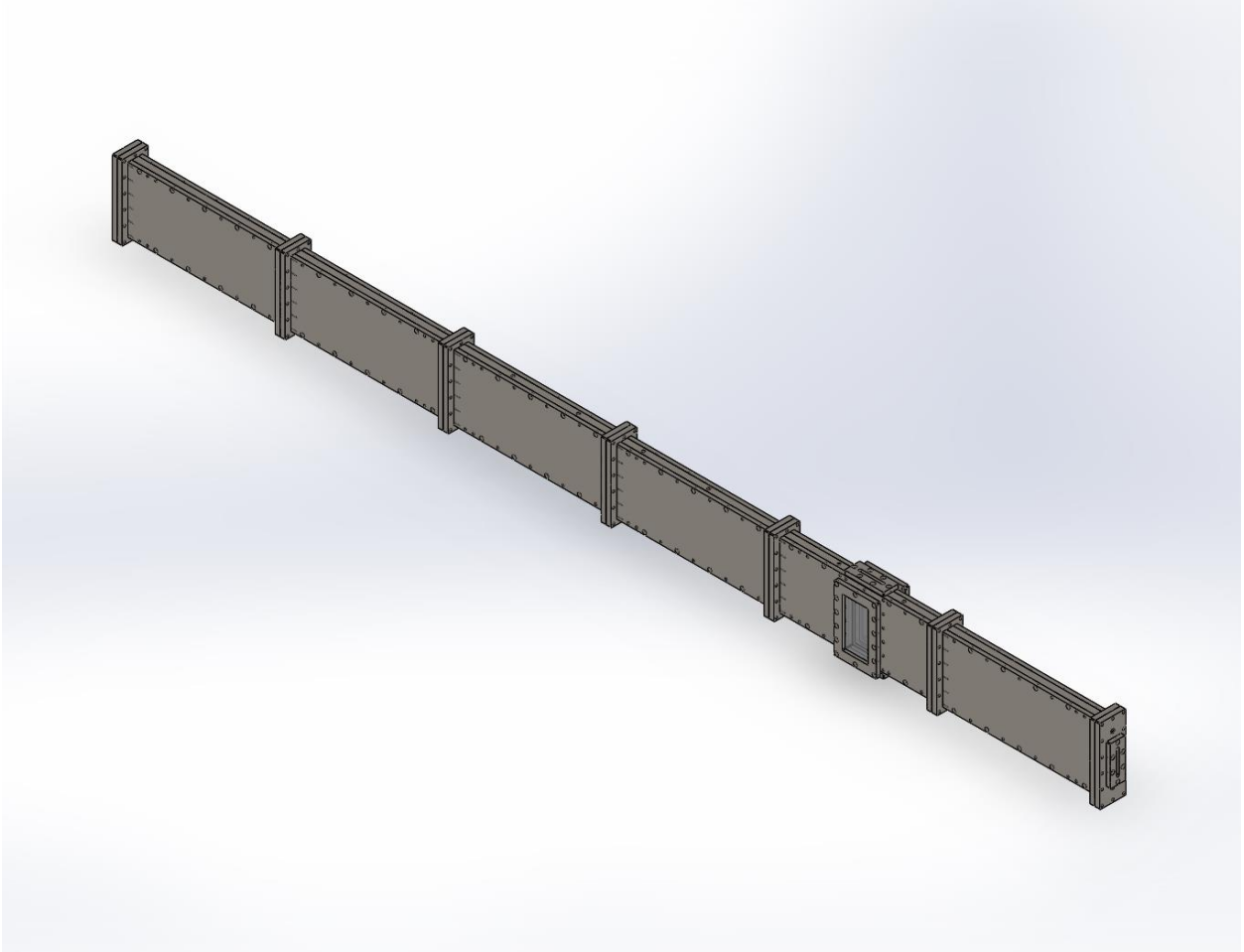
APPENDIX B – Ignition system with three spark plug
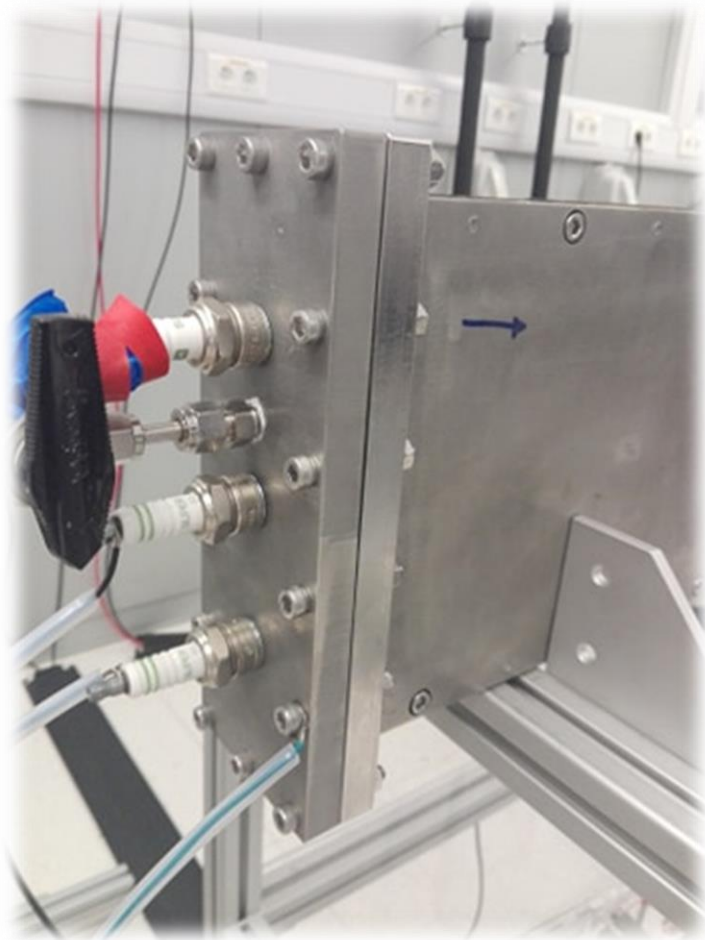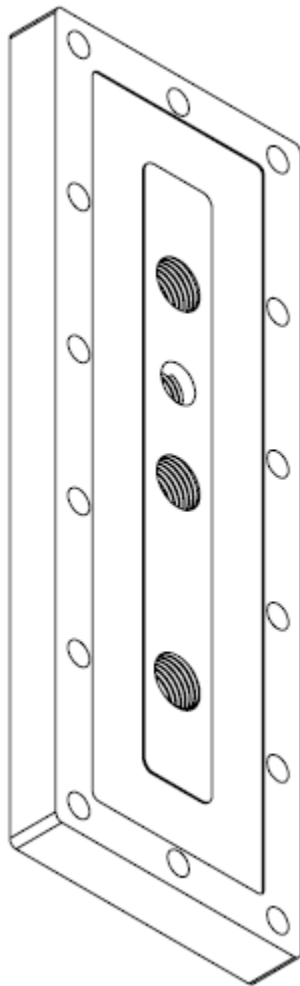
APPENDIX C – Drawing of Obstacle two
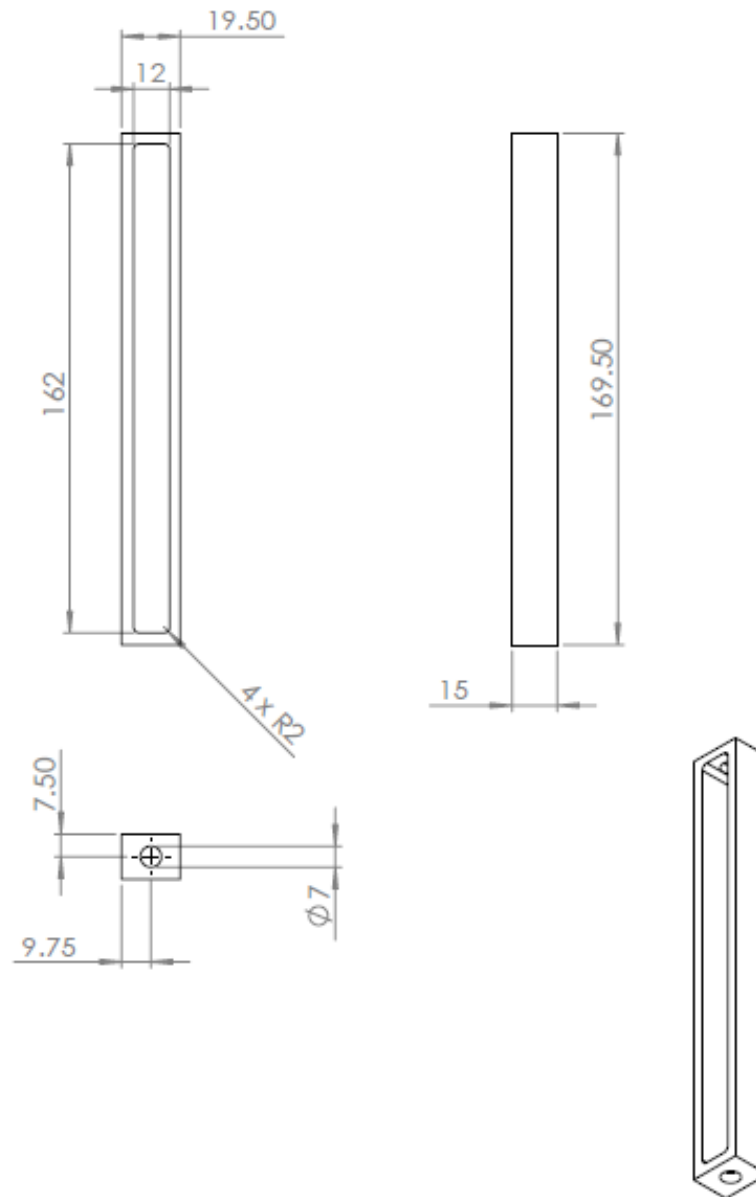
APPENDIX D – Drawing of obstacle one

15	7	
A	Ø 7	Ø 12
20	A-A	
40		
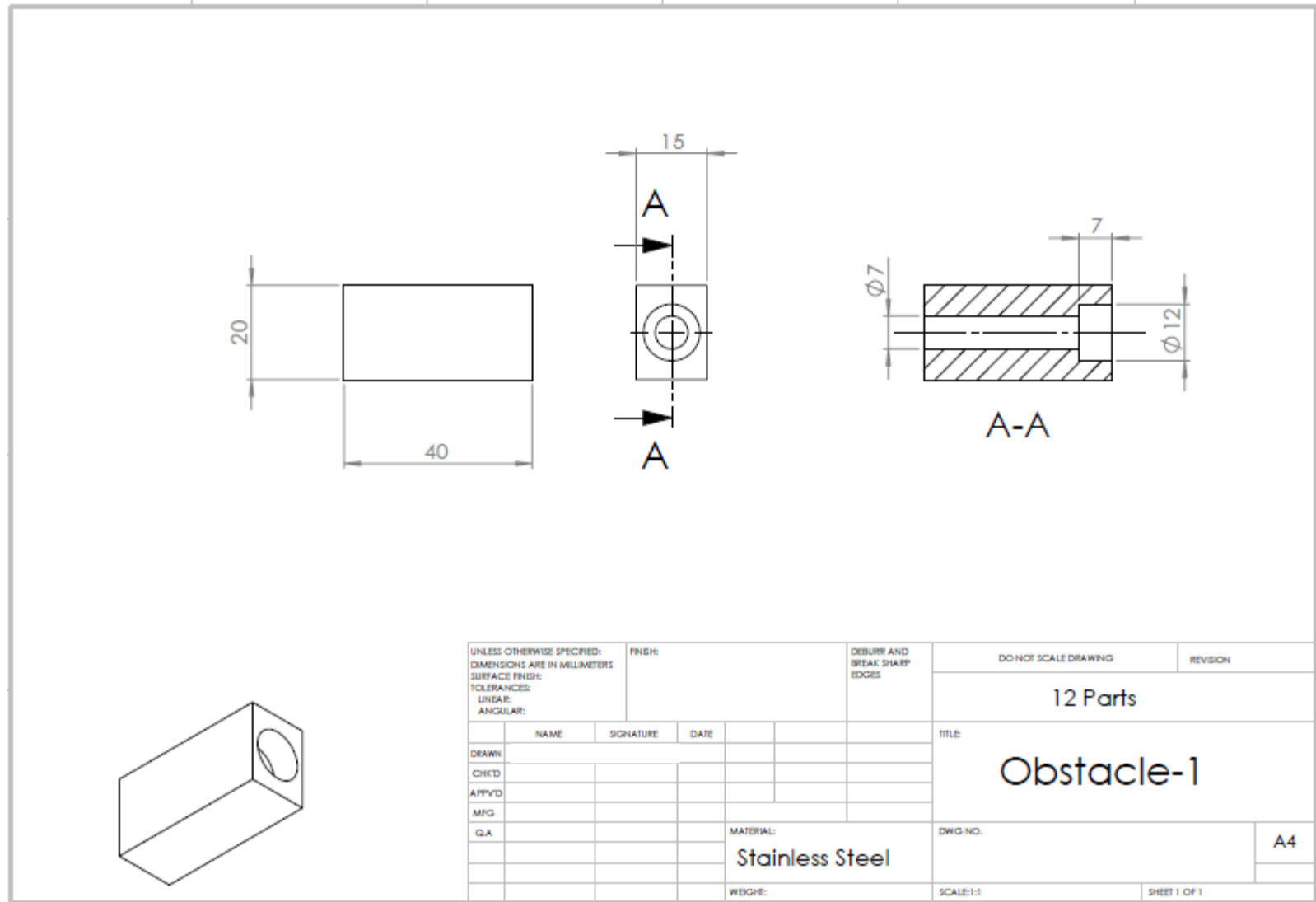
APPENDIX E – Three optical access for diagnostic purposes
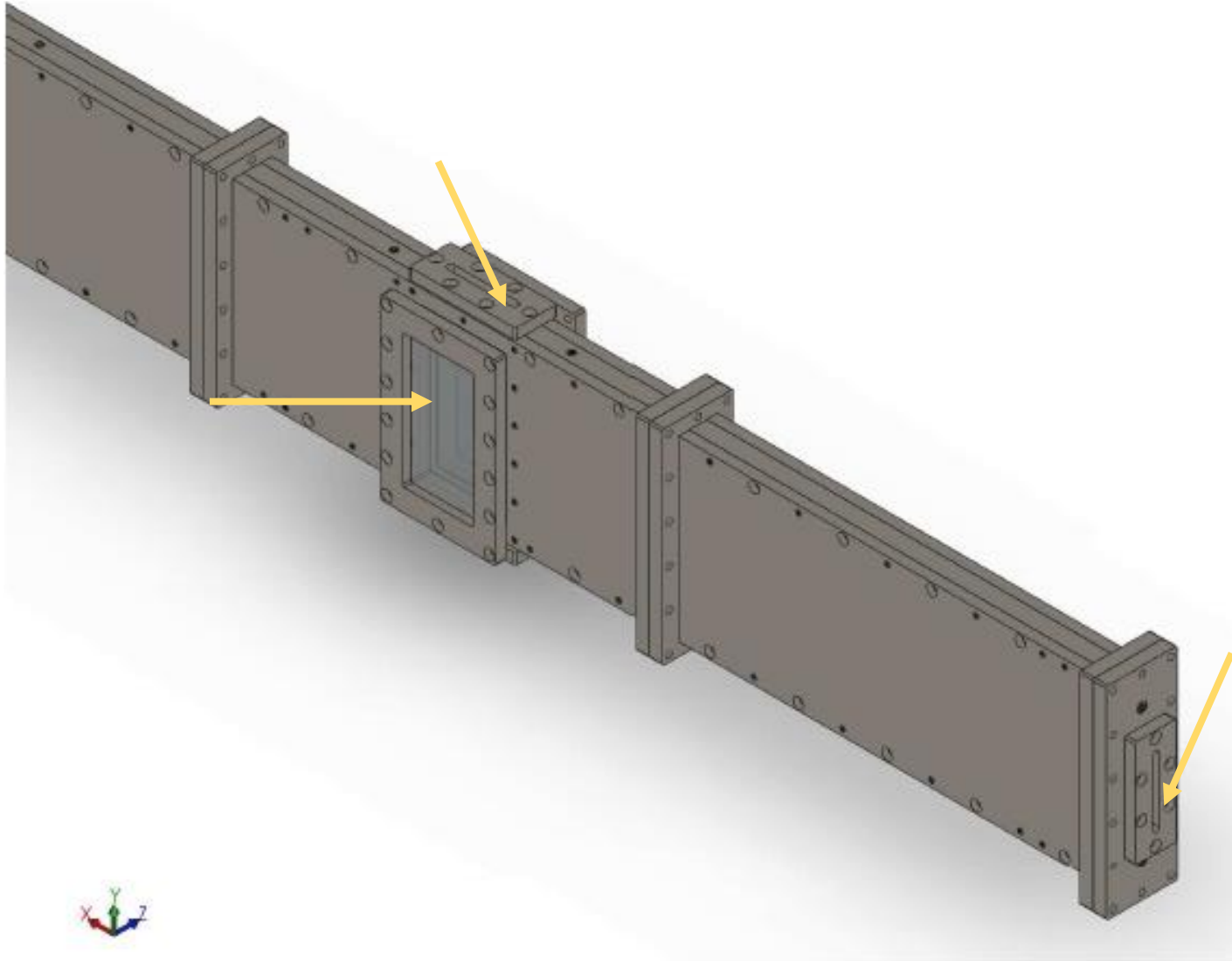
APPENDIX F – Parallel PLIF configurations
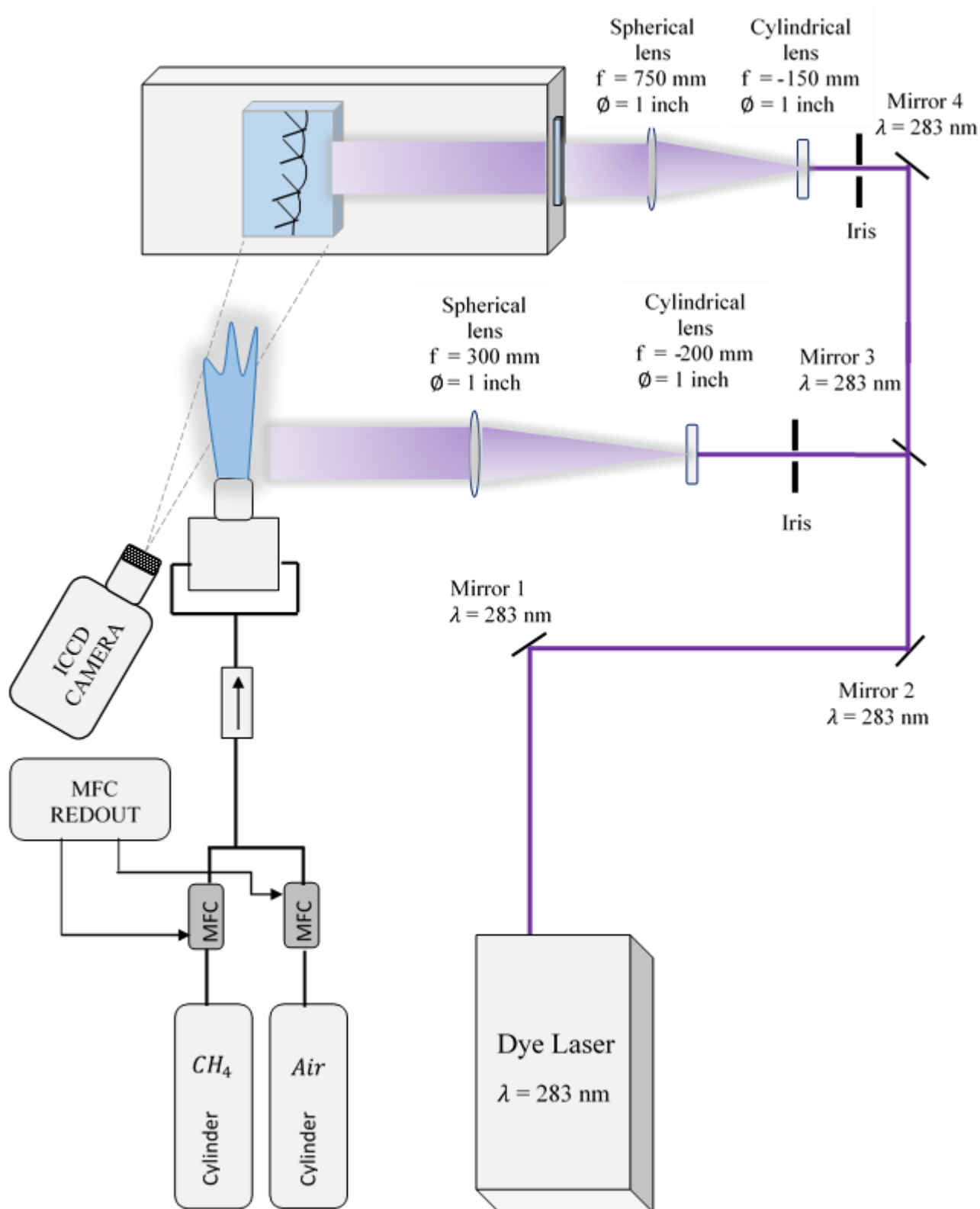
APPENDIX G – Cell size based on initial conditions

(a) H2-Air1 from (GUIRAO, 1982) at T=293 K, P=101.3 kPa
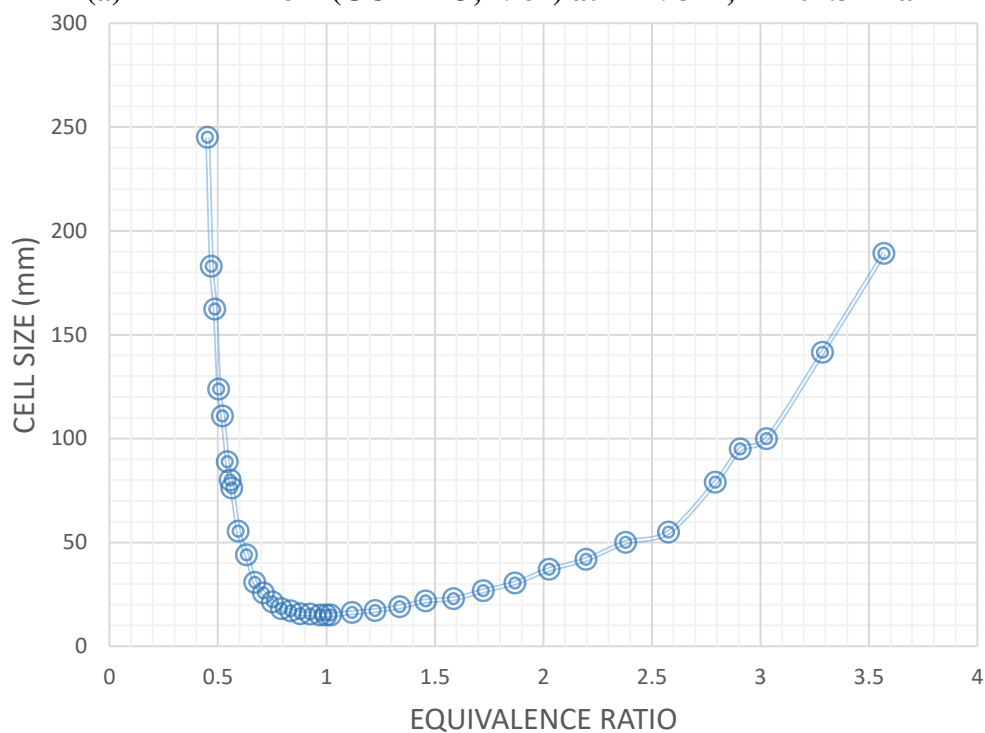
(b) H2-Air1 from (STAMPS, 1991) at T=293 K, ER=1

$y = -2E-05x^3 + 0{,}0076x^2 - 0{,}832x + 40{,}855$

$R^2 = 0{,}9905$
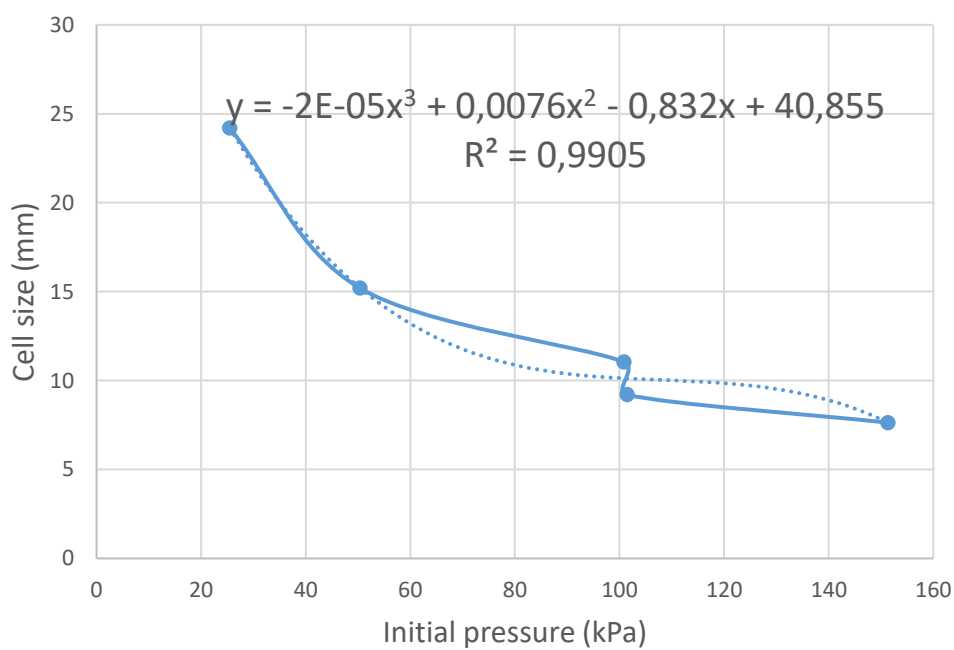
APPENDIX H – Own authorship-Schlieren images
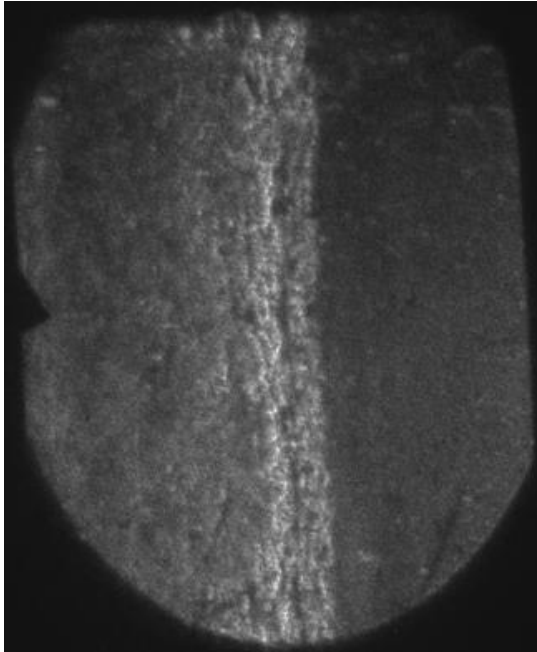
P=0.5 bar, ER=1, V=1941 m/s
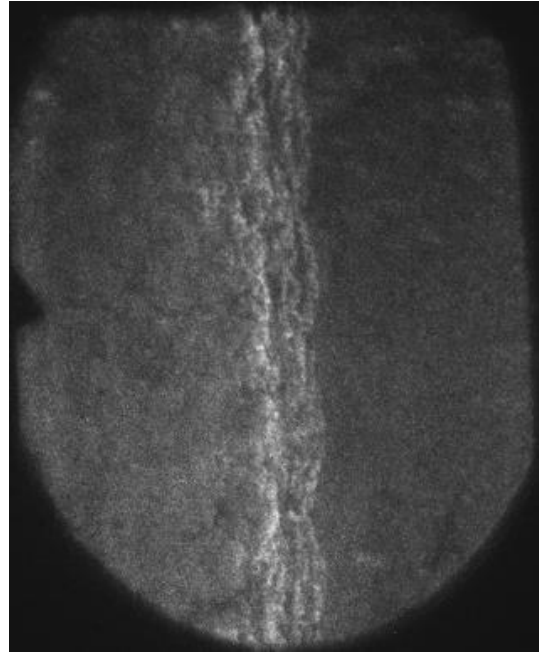
P=0.5 bar, ER=1, V=1914 m/s
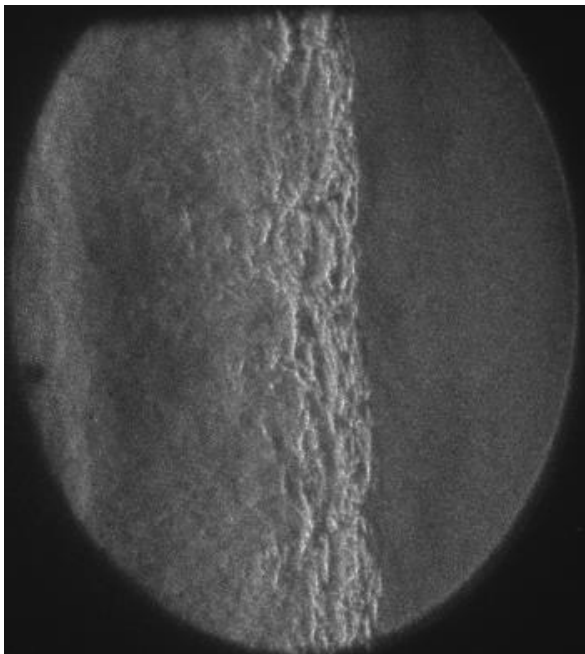
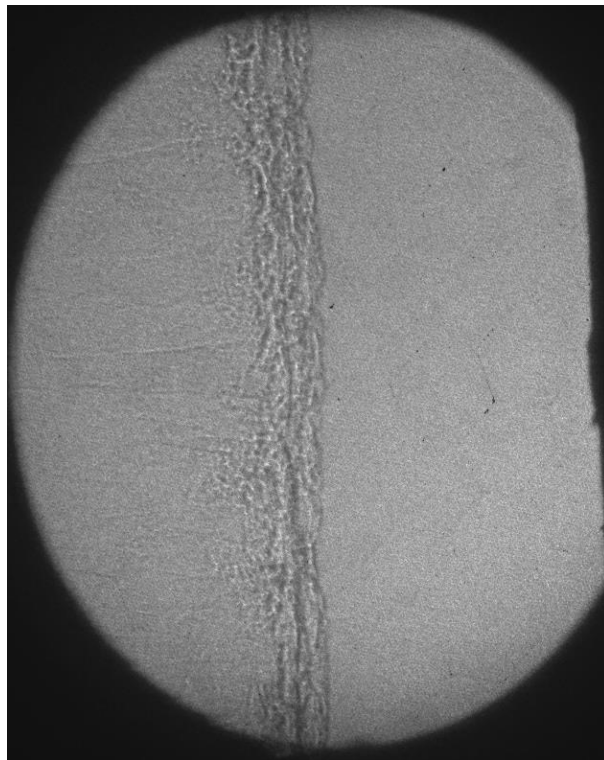

P=0.5 bar, ER=1, V=1941.75 m/s
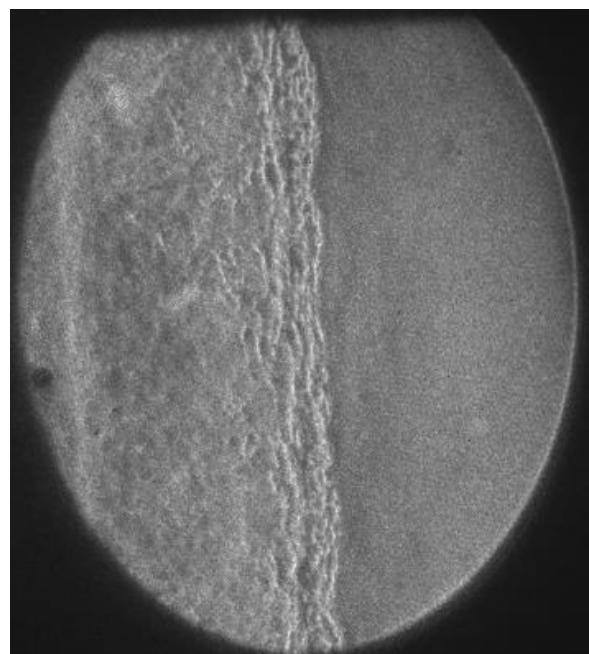
P=0.5 bar, ER=1, V=1923.08 m/s
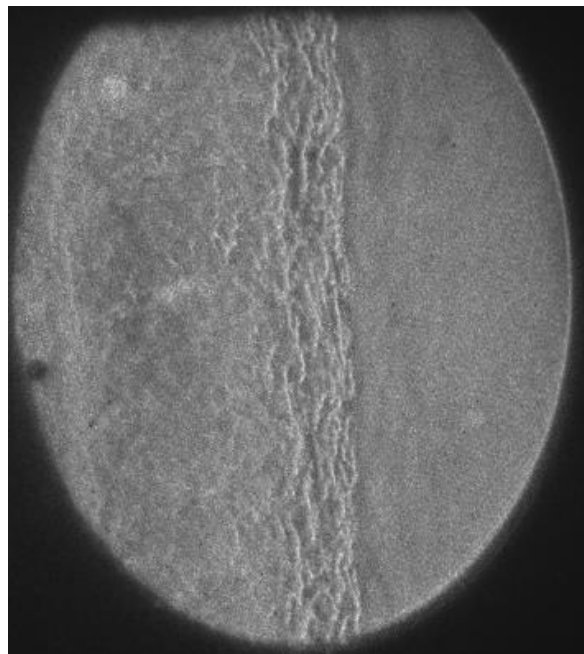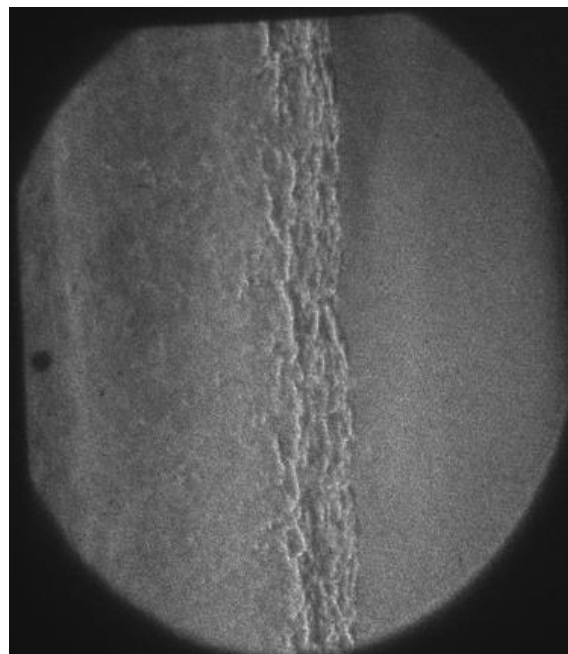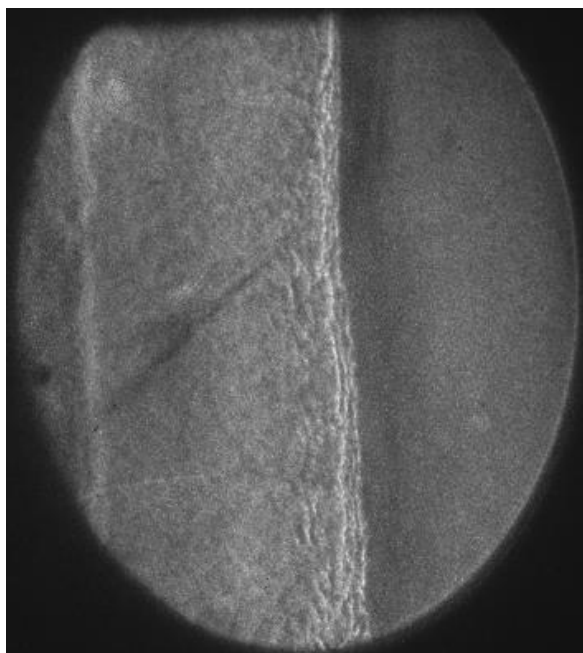
P=0.5 bar, ER=1, V=1923 m/s

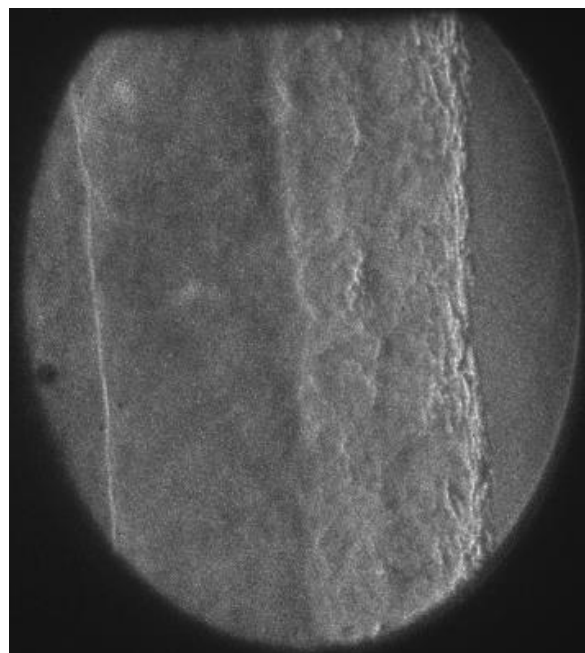P=0.5 bar, ER=1, V=1923 m/s
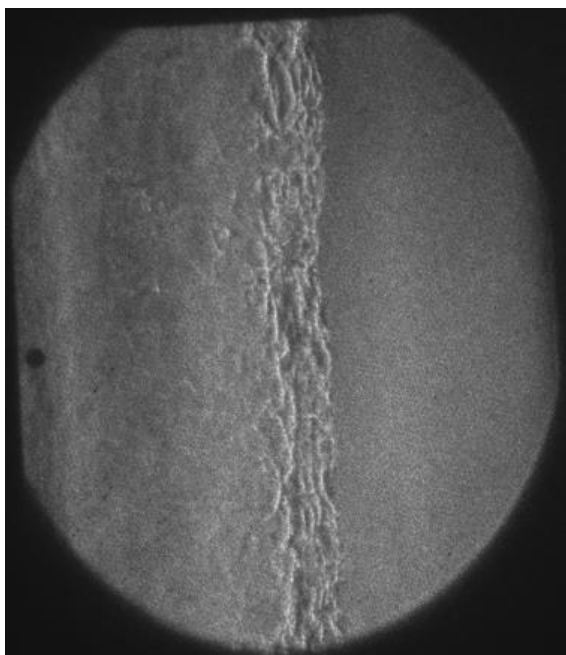
P=0.5 bar, ER=1, V=1907.76 m/s
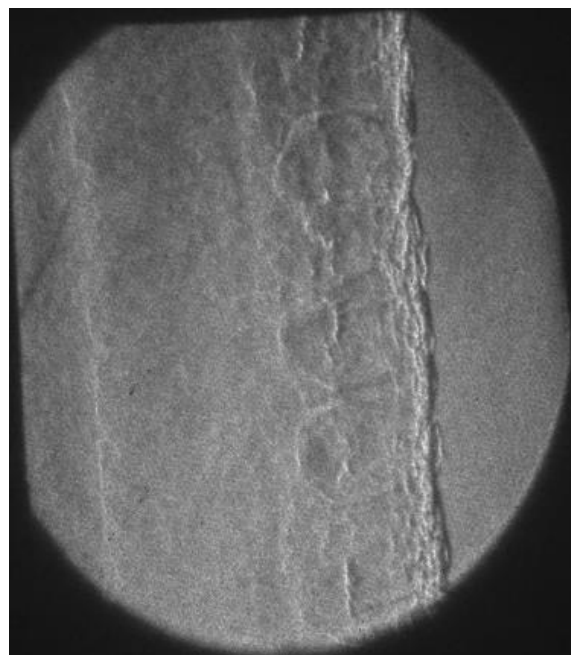
P=0.5 bar, ER=1, V=1941.75 m/s
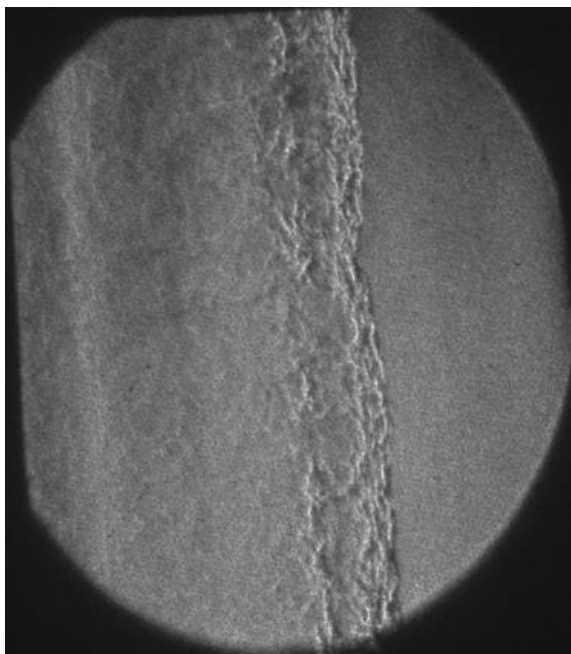
P=0.5 bar, ER=1, V=1942 m/s
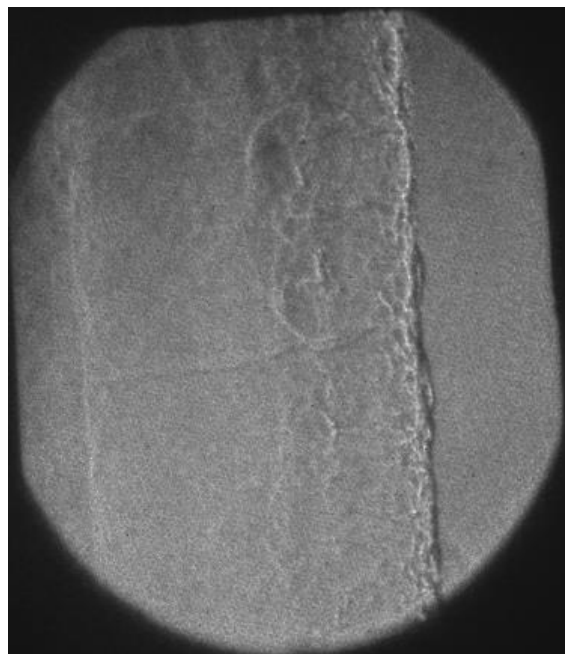
P=0.5 bar, ER=1, V=1904.76 m/s
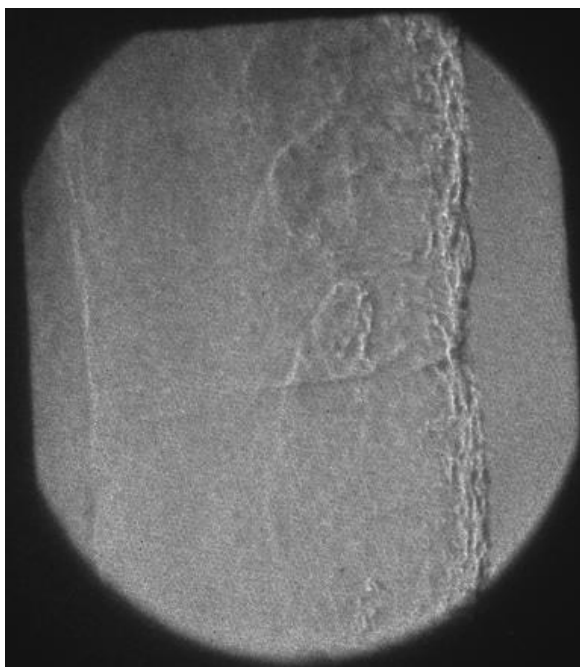
P=0.5 bar, ER=1, V=1923.08 m/s
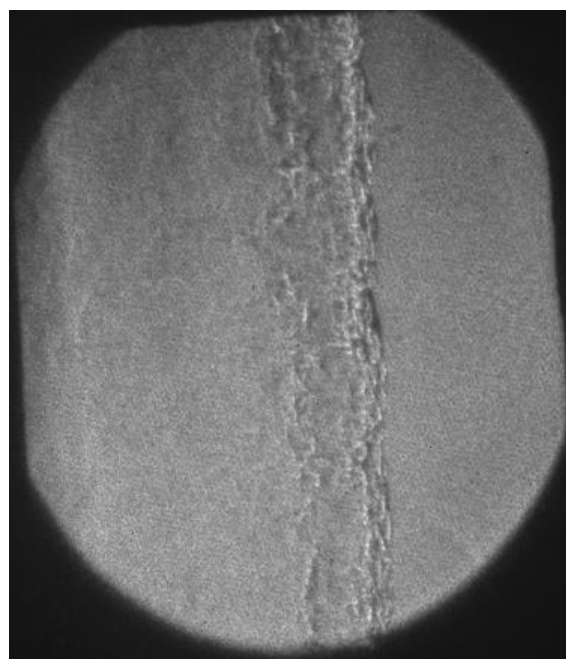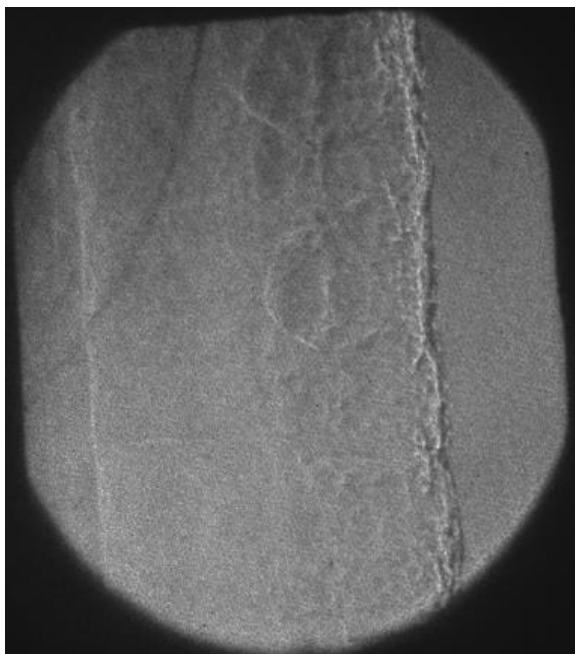
P=0.5 bar, ER=1, V=1923 m/s

P=0.5 bar, ER=1, V=1941.75 m/s
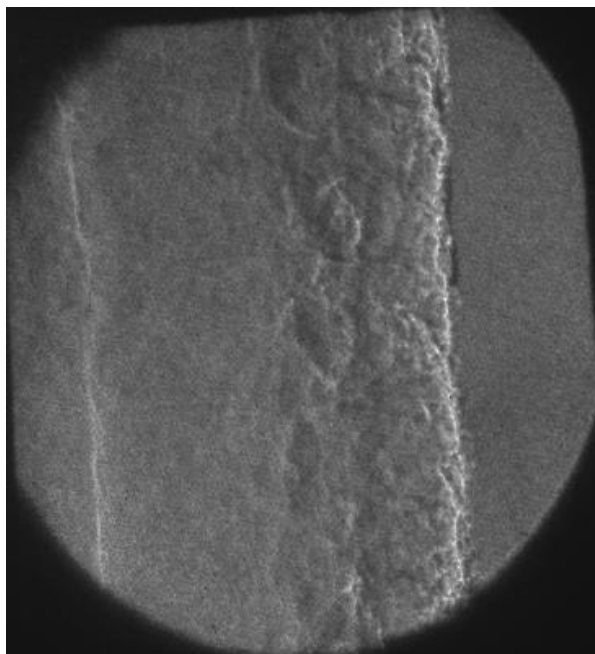
P=0.5 bar, ER=1, V=1904 m/s
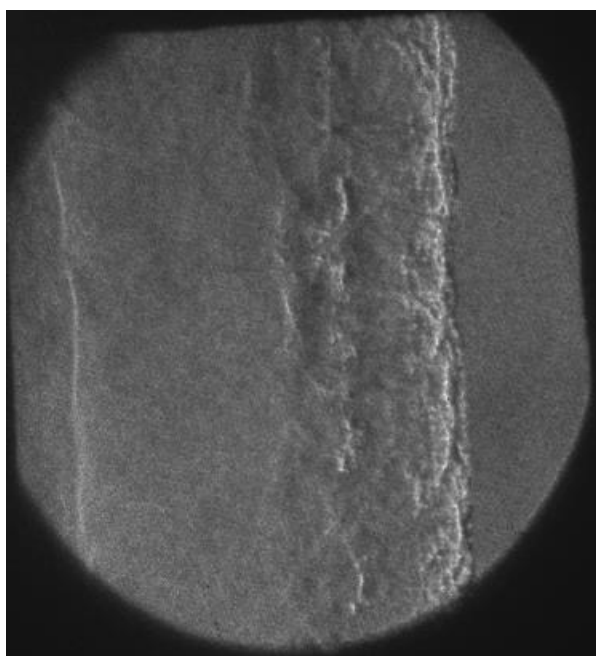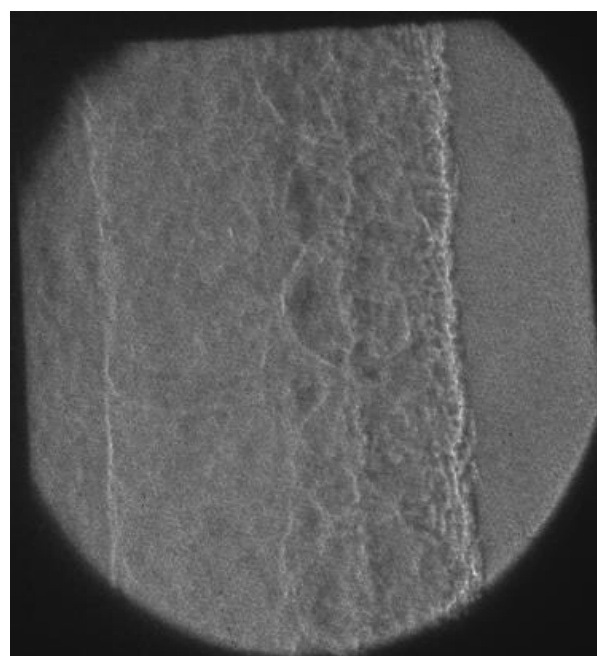
P=0.5 bar, ER=1, V=1904 m/s
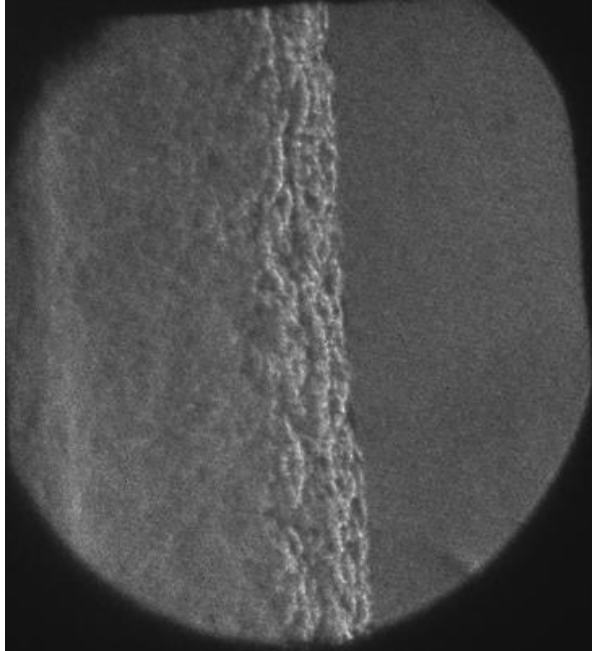
P=0.5 bar, ER=1, V=1904 m/s

P=0.5 bar, ER=1, V=1923 m/s
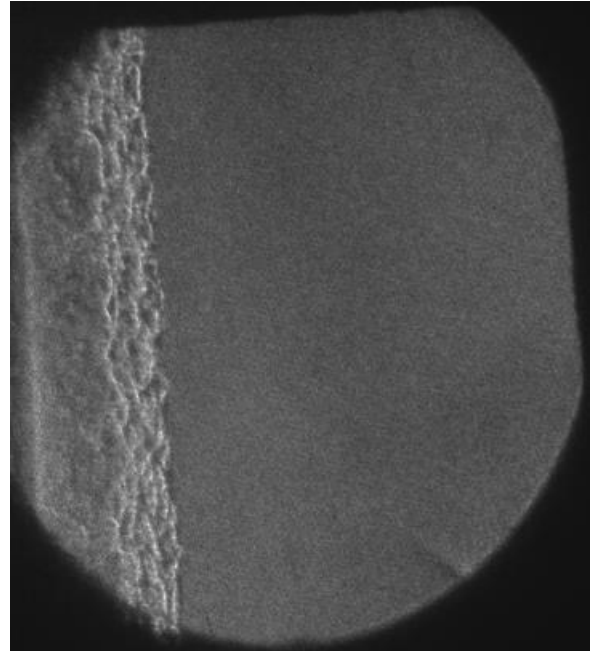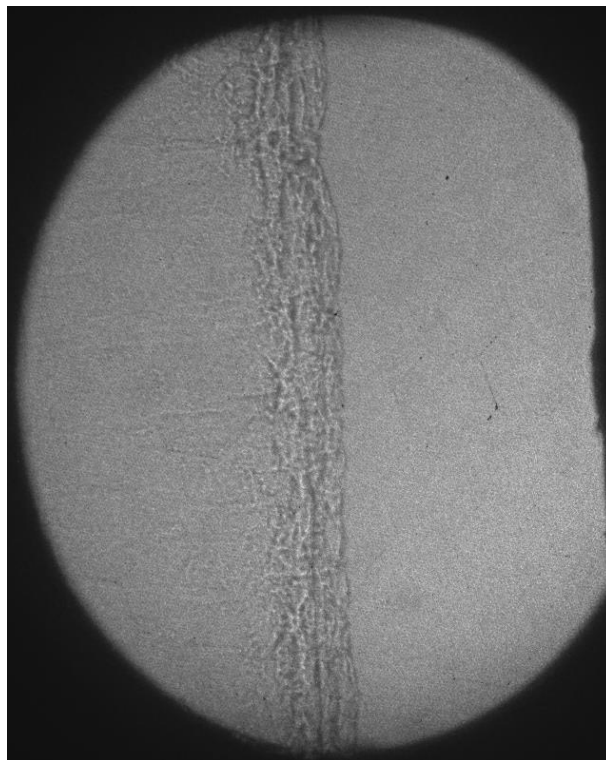
P=0.5 bar, ER=1, V=1904 m/s

P=0.5 bar, ER=1, V=1886.79 m/s
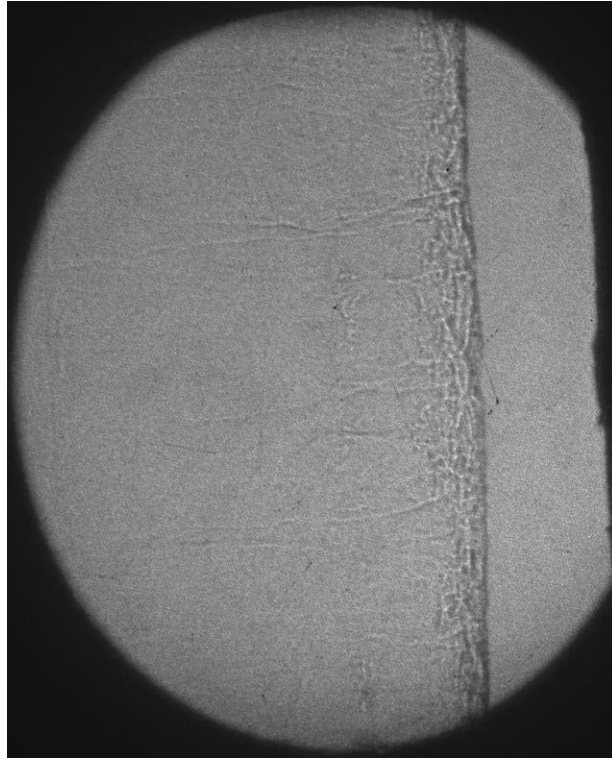
P=0.5 bar, ER=1, V=1869 m/s
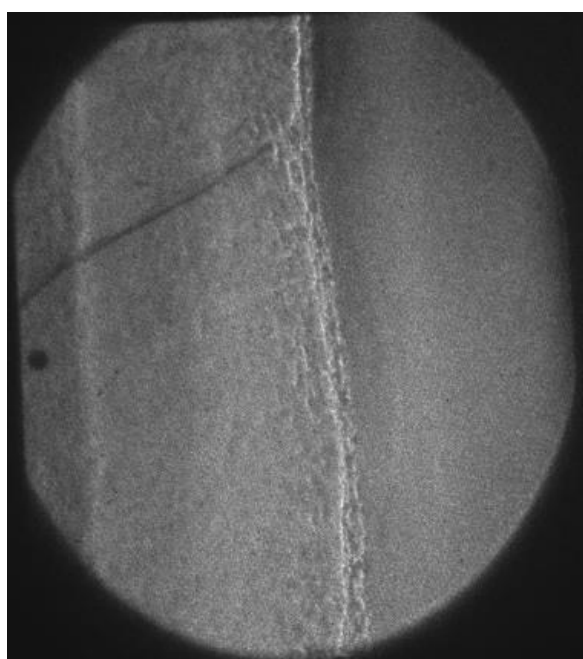

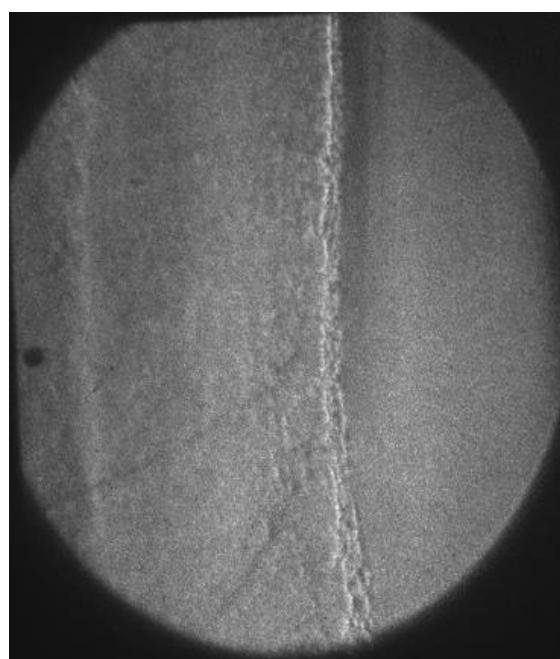P=0.5 bar, ER=1, V=1900 m/s

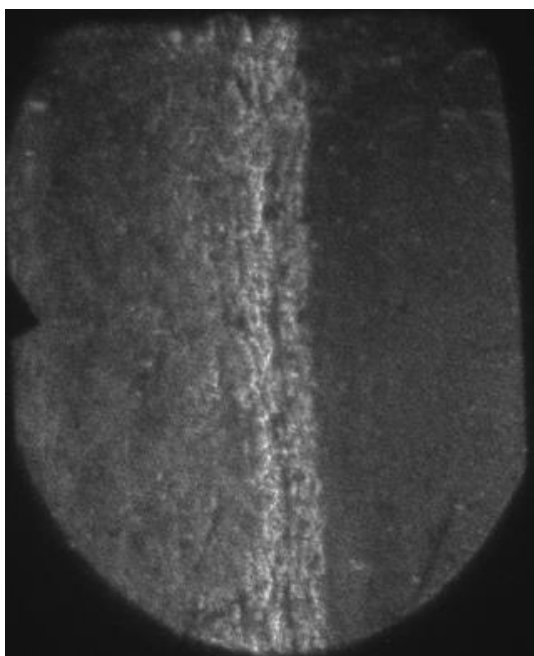P=0.4 bar, ER=1, V=1980.2 m/s

P=0.4 bar, ER=1, V=1904.76 m/s
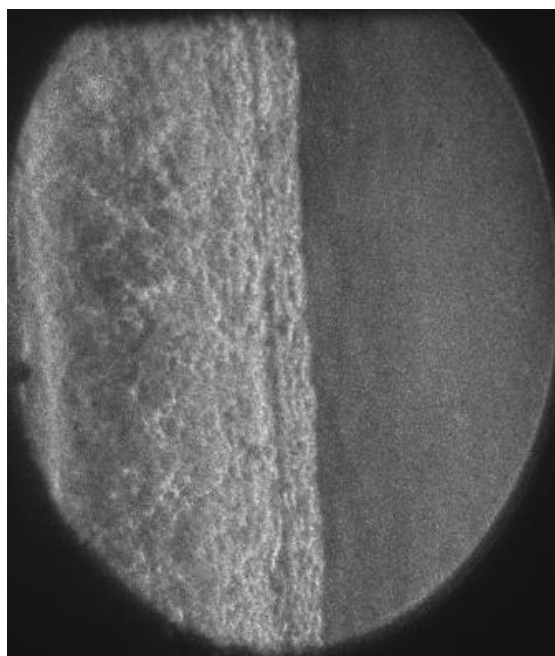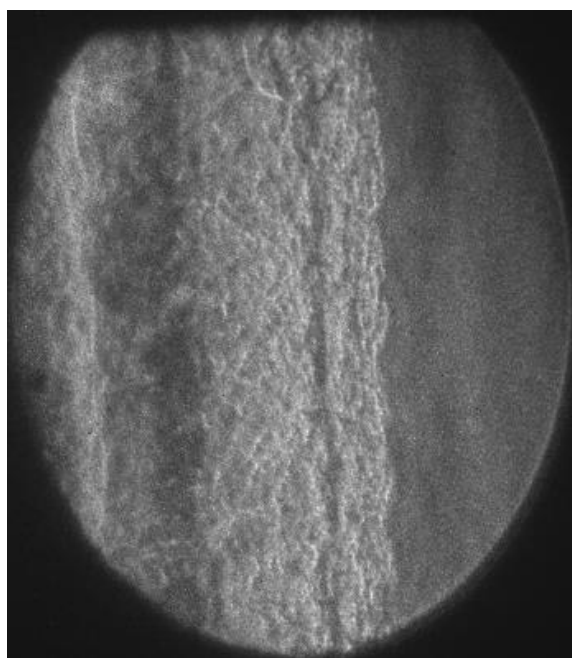

P=0.4 bar, ER=1, V=2020.2 m/s

P=0.4 bar, ER=1, V=2020 m/s

P=1 bar, ER=0.9 , V=1869 m/s

P=1 bar, ER=0.9 , V=1869.16 m/s

P=1 bar, ER=0.9 , V=1818.18 m/s

APPENDIX I – OH intensities of the methane-air flame scan

Wavelength (nm)	Normalized fluorescence intensity
283.2	0
283.205	0.045539937
283.215	0.019628166
283.21	0.00900434
283.22	0.049491482
283.225	0.073978105
283.23	0.183779232
283.235	0.49096327
283.24	0.656604262
283.245	1
283.25	0.260283734
283.255	0.075727149
283.26	0.079160459
283.265	0.090561638
283.27	0.12081363
283.275	0.256785645
283.28	0.857679601
283.285	0.671956986
283.29	0.216557621
283.295	0.240785127
283.3	0.114789143
283.305	0.074431561
283.31	0.157737902
283.315	0.104489214
283.32	0.072293839